

# Electronic structure of topological semimetals

---

## DISSERTATION

zur Erlangung des akademischen Grades

Doctor rerum naturalium  
(Dr. rer. nat.)

vorgelegt

dem Bereich Mathematik und Naturwissenschaften  
der Technischen Universität Dresden

von

M.SC. ERIK HAUBOLD  
geboren am 5. Juli 1990 in Jena



Eingereicht am 13. Mai 2019

Verteidigt am 2. Oktober 2019

1. Gutachter: Prof. Dr. Bernd Büchner  
IFW Dresden

2. Gutachter: apl. Prof. Dr. Oliver Rader  
Helmholtz-Zentrum Berlin

Die Dissertation wurde in der Zeit von August 2015 bis April 2019 am Leibniz-Institut für Festkörper und Werkstofforschung (IFW Dresden) angefertigt.



## Abstract

Topology, an important topic in physics since several years, is handled as possible solution to many current-state problems in electronics and energy. It could allow to dramatically shrink computational devices or increase their speed without the current problem of heat dissipation, or topological principles can be used to introduce room temperature high-conduction paths within materials.

Unfortunately, while many promising materials have been presented yet, the one breakthrough material is still missing. Current state materials are either consisting of toxic elements, obstructing possible use cases, or their electronic structure is too complex to investigate the interplay of all the facets of the electronic structure present in the materials.

In this thesis, two very promising materials will be thoroughly introduced, namely TaIrTe<sub>4</sub> and GaGeTe. Both materials have the potential, to lift one of the shortcomings mentioned.

First, TaIrTe<sub>4</sub> will be presented. TaIrTe<sub>4</sub> is a simplistic Weyl semimetal in terms of its electronic and topological structure - the simplest yet known material. It hosts four Weyl points, the minimum amount of Weyl nodes possible in a non-centrosymmetric material. Predictions state, that these nodes are well separated throughout the Brillouin zone, and are connected by nearly parallel Fermi arcs. The existence of the topological states is proved in this thesis through angle-resolved photoemission spectroscopy (ARPES) and confirmed by spin polarization measurements on these states. GaGeTe is predicted to be a Bi<sub>2</sub>Se<sub>3</sub>-style topological insulator, but ARPES data presented shows, that no direct band gap could be observed. Yet, a topological state is still believed to be present. This makes this material interesting in many ways: its elemental composition is less toxic than bismuth and selenium, as well as it is the first realization of such a specific electronic structure. A full discussion of the electronic states close to the Fermi level including the possible existence of topological states is shown in this thesis.



# Contents

<b>List of Figures</b>	<b>v</b>
<b>List of Tables</b>	<b>ix</b>
<b>1 Topology</b>	<b>1</b>
1.1 Topology in Math . . . . .	2
1.2 Topology in Band Structure . . . . .	3
1.2.1 Levi-Civita-Transport . . . . .	3
1.2.2 Topological invariants . . . . .	4
1.2.3 The Berry phase . . . . .	5
1.2.4 The Berry connection, Berry curvature and Chern number . . . . .	6
1.3 Topological insulators . . . . .	8
1.3.1 The quantized Hall effects . . . . .	8
1.3.2 Spin-Orbit coupling . . . . .	12
1.3.3 The $\mathbb{Z}_2$ invariant . . . . .	15
1.3.4 3D topological insulators . . . . .	16
1.4 Semimetals . . . . .	19
1.4.1 The Dirac equation . . . . .	19
1.4.2 The Majorana equation . . . . .	22
1.4.3 The Weyl equation . . . . .	22
1.4.4 Weyl semimetals . . . . .	23
1.4.5 The chiral anomaly . . . . .	27
1.5 Recent advances in topological materials . . . . .	28
1.5.1 Topological insulators . . . . .	29
1.5.2 Dirac semimetals . . . . .	29

1.5.3	Weyl semimetals . . . . .	30
1.6	Future applications of topological matter . . . . .	31
<b>2</b>	<b>Experimental Details</b>	<b>33</b>
2.1	Angle-resolved photoemission spectroscopy - ARPES . . . . .	33
2.1.1	ARPES and semimetals . . . . .	38
2.2	Sample preparation considerations . . . . .	40
2.3	Experimental setups . . . . .	41
2.3.1	The resolution of ARPES . . . . .	42
2.3.2	End stations . . . . .	44
2.3.3	Light sources . . . . .	44
<b>3</b>	<b>TaIrTe<sub>4</sub> - a ternary type-2 Weyl semimetal</b>	<b>49</b>
3.1	Theory predictions . . . . .	49
3.2	Crystal growth . . . . .	55
3.3	Transport measurements . . . . .	55
3.3.1	Magneto-resistance . . . . .	55
3.3.2	Hall effect . . . . .	56
3.3.3	Quantum oscillations . . . . .	58
3.4	ARPES measurements . . . . .	59
3.4.1	Fermi surface and band structure . . . . .	59
3.4.2	Cleavage plane . . . . .	63
3.4.3	Topology in TaIrTe <sub>4</sub> . . . . .	66
3.4.4	Conclusion . . . . .	71
3.5	Outlook . . . . .	72
3.5.1	Advanced ARPES measurements . . . . .	72
3.5.2	Superconductivity . . . . .	73
3.5.3	Ta(IrRhRu)Te <sub>4</sub> . . . . .	74
<b>4</b>	<b>GaGeTe - a simple topological semimetal</b>	<b>77</b>
4.1	Theoretical aspects of the GaGeTe band structure . . . . .	77



---

4.2	ARPES on GaGeTe . . . . .	84
4.2.1	Topology in GaGeTe . . . . .	90
4.3	Conclusion . . . . .	94
<b>5</b>	<b>Summary</b>	<b>97</b>
	<b>Bibliography</b>	<b>99</b>
	<b>List of Publications</b>	<b>115</b>
	<b>Acknowledgements</b>	<b>117</b>
	<b>Erklärung</b>	<b>119</b>



# List of Figures

1.1	Objects of different topological genus . . . . .	2
1.2	Levi-Civita transport on a sphere and a plane . . . . .	4
1.3	Different topological objects and their band structure counterparts . . . . .	8
1.4	The quantized Hall effect . . . . .	10
1.5	Schematic of the quantum, quantum spin and quantum anomalous Hall effect . . . . .	11
1.6	Schematic of spin-orbit coupling and Kramers degeneracy . . . . .	12
1.7	Schematic of a band inversion . . . . .	14
1.8	Bulk boundary correspondence . . . . .	15
1.9	Schematic of a spin Hall insulator . . . . .	16
1.10	Overview of $\mathbb{Z}_2$ configuration in 3D topological insulators . . . . .	17
1.11	Fermi surface of weak and strong topological insulators . . . . .	17
1.12	Possible transition between trivial insulators, dirac semimetals and topological insulators. . . . .	21
1.13	Schematic Brillouin zone of a Dirac semimetal . . . . .	21
1.14	Schematic structure of a Weyl semimetal . . . . .	23
1.15	Symmetries of Weyl points . . . . .	24
1.16	Surface states in Weyl semimetals . . . . .	25
1.17	Comparison of surface states of Dirac and different Weyl semimetals . . . . .	25
1.18	Type-1 and type-2 Weyl semimetal . . . . .	27
1.19	Chiral anomaly . . . . .	27
2.1	Three step model of the electron excitation during a PES experiment . . . . .	34
2.2	Penetration depth of photons in ARPES . . . . .	35
2.3	Geometry of a ARPES setup . . . . .	35

2.4	Sample preparation procedure . . . . .	40
2.5	Experimental ARPES setup . . . . .	41
2.6	Comparison between real and measured band structure . . . . .	43
3.1	Atomic structure of TaIrTe <sub>4</sub> . . . . .	49
3.2	Comparison of the band structure of TaIrTe <sub>4</sub> and WTe <sub>2</sub> . . . . .	50
3.3	Band structure details of TaIrTe <sub>4</sub> . . . . .	50
3.4	Fermi surface of TaIrTe <sub>4</sub> . . . . .	51
3.5	Berry phase calculations of TaIrTe <sub>4</sub> . . . . .	52
3.6	Calculated TaIrTe <sub>4</sub> Fermi surface maps . . . . .	53
3.7	Comparison of the topological states of different Weyl semimetals . . . . .	54
3.8	Magnetoresistance measurements of TaIrTe <sub>4</sub> for each axis . . . . .	56
3.9	Temperature dependent magneto-resistance of TaIrTe <sub>4</sub> . . . . .	57
3.10	De-Haas-van-Alphen measurements of TaIrTe <sub>4</sub> . . . . .	58
3.11	Comparison of band structure and ARPES data at 100 eV . . . . .	60
3.12	Fermi surface maps of TaIrTe <sub>4</sub> for different photon energies. As well as k <sub>z</sub> map. . . . .	61
3.13	Comparison of measured and calculated Fermi surface . . . . .	62
3.14	Comparison of band structure calculations of surface 1 & 2 with ARPES . . . . .	62
3.15	Comparison of Fermi surfaces of surfaces 1 & 2 with ARPES maps . . . . .	64
3.16	ARPES cuts and Fermi level MDC curves . . . . .	65
3.17	Comparison of ARPES and de-Haas-van-Alphen . . . . .	66
3.18	Surface states in TaIrTe <sub>4</sub> . . . . .	67
3.19	Calculated surfaces states for both surface terminations . . . . .	68
3.20	Spin polarization of the (001) surface of TaIrTe <sub>4</sub> . . . . .	69
3.21	Spin polarization of the (00 $\bar{1}$ ) surface of TaIrTe <sub>4</sub> . . . . .	70
3.22	Pump-probe ARPES data of TaIrTe <sub>4</sub> . . . . .	72
3.23	STM data of TaIrTe <sub>4</sub> showing topological superconductivity . . . . .	74
3.24	Comparison of TaIrTe <sub>4</sub> and TaRhTe <sub>4</sub> energy-momentum cuts . . . . .	75
3.25	Comparison of TaIrTe <sub>4</sub> and TaRhTe <sub>4</sub> Fermi surface maps . . . . .	76
4.1	Structure of GaGeTe . . . . .	78

---

4.2	HRTEM data of GaGeTe . . . . .	78
4.3	Brillouin zone of GaGeTe . . . . .	79
4.4	Non-relativistic band structure calculation of GaGeTe . . . . .	80
4.5	Comparison of PBE and HSE calculated band structure with ARPES .	81
4.6	Band structure calculated using GW . . . . .	82
4.7	Predicted topology of GaGeTe . . . . .	83
4.8	Images of GaGeTe crystals . . . . .	83
4.9	ARPES Fermi surface map and energy-momentum cut of GaGeTe . . .	84
4.10	Comparison of all calculation methods with ARPES . . . . .	85
4.11	Dosing experiments to analyse a possible gap . . . . .	87
4.12	Detailed comparison of ARPES data and band structure using PBE functional . . . . .	88
4.13	Analysis of the measured $k_z$ behaviour in comparison to calculations . .	89
4.14	Comparison of expected topological states with ARPES data . . . . .	90
4.15	Suggested behaviour of bands by ARPES data . . . . .	91
4.16	Images of cleaved GaGeTe and Bi <sub>2</sub> Se <sub>3</sub> crystals . . . . .	92
4.17	Surface feature recalculated with slightly changed lattice parameters . .	92
4.18	Comparison of ARPES and PBE calculations with and without distortion	93
4.19	Proposed Fermi surface based on previous results . . . . .	94



# List of Tables

2.1	Used ARPES end stations and experimental setups . . . . .	44
3.1	Overview of the spin polarization measurements on the (001) surface. .	69
3.2	Overview of the spin polarization measurements on the (00 $\bar{1}$ ) surface. .	71
3.3	Different compositions of Ta(Ir <sub>x</sub> Rh <sub>1-x</sub> )Te <sub>4</sub> . . . . .	75
4.1	Overview of calculation results for GaGeTe band structure using different methods . . . . .	81





# 1 Topology

In the recent years, technological limitations slowed down the progression stated in Moore's law substantially. Originally postulated 1965 it stated, that the complexity - being the number of integrated electronic components - doubles every 12-24 months [1, 2]. Initially predicted to be valid for ten years, it was adjusted later in 1975. While this still is true for nowadays electronics, the pace can not be kept up for long anymore. Continuing with the current pace, integrated circuits will be at atomic scales in the mid 2020's [3, 4]. This is an ultimate physical limit of what is achievable with current style electronics. Progressing from the current 14 nm to 7 nm feature sizes down to 5 nm already requires the use of extreme ultraviolet lithography, introducing a new high cost and very complex factor in the lithographic processes.

Even if the shrinking can be managed by technology and costs, waste heat becomes a major issue the smaller the features are getting [5]. Ultimately, to overcome these limitations, new approaches are needed like spintronic devices, which rely on switching electron spins instead of moving around the electrons themselves - greatly reducing the dissipated heat throughout the process while maintaining the same speed.

While spintronics is not a new idea, it is yet too clunky and bulky to keep up with modern silicon based "classical" electronics. At this point, topological materials are coming into play, greatly reducing the sizes of possible spintronic circuits by utilizing intrinsic features of the respective materials. Topology in solid state matter is still a very new field within physics, with research starting around 2010.

In this thesis, two new topological materials will be introduced, whose properties make them unique candidates for further research in topological materials and their use in electronics in general, as well as the potential use of these specific materials in future applications. The thesis will first give an overview about topology in general,

highlighting the theoretical side, and then discuss the experimental method to resolve the electronic structure. The last two chapters are presenting TaIrTe<sub>4</sub> and GaGeTe, discussing their properties and potential.

## 1.1 Topology in Math

Topology, a field of mathematics, is discussing properties of geometric bodies that are invariant to continuous transformations of these bodies. As an example, one can take a coffee mug and a torus. Now one could draw lines between different points of the surface on the mug, some going through the handle, others not. When now transforming the mug to a torus, all lines will remain, as there is still one hole in the object. However, transforming into objects with different numbers of holes is not possible, as either lines through holes get lost or new ones appear. Fig. 1.1 shows exemplary objects of different topological classes where a transformation into each other is not possible.

These surfaces are characterized by a topological invariant, called the Euler characteristic in this case. Taking a surface  $A$ , the Euler characteristic  $\chi(A)$  can be determined using the Gauss-Bonnet theorem:

$$\int_A K dA = 2\pi\chi(A) = 2\pi(2 - 2g) \quad (1.1)$$

With  $K$  being the Gaussian curvature of the surface and  $g$  its genus. The genus identifies a topological class of an object. All bodies which can be transformed into each other do have the same genus and thus the same topological class. In this case, this also implies that all objects having the same number of holes are belonging to the same topological class.

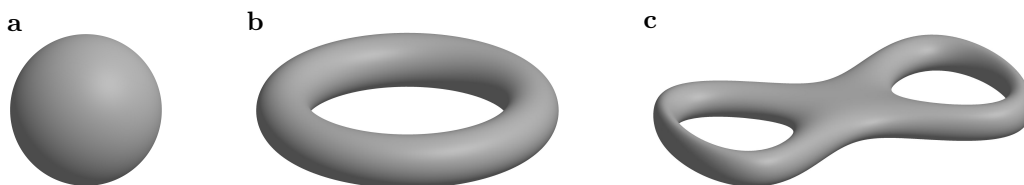


Figure 1.1: Topological objects of different genus. a) Sphere with  $g = 0$ , b) Torus with  $g = 1$ , c) double torus with  $g = 2$ .

## 1.2 Topology in Band Structure

In 1972 J. Michael Kosterlitz and David J. Thouless successfully used the concepts of topology in physics, discovering -an until this point- unknown phase transition in 2D systems, where topological defects play crucial roles. This work is very important for the understanding of the quantum theory of 1D systems at very low temperatures [6, 7].

In 1980, David J. Thouless and F. Duncan M. Haldane developed methods, identifying phases which can not be simply described by their symmetry breaking. In 1982, the quantization of the Hall effect was explained in very detail [8]. 1983 theories for spin chains were postulated, incorporating topological effects in crucial ways [9, 10]. Since then, a lot of effects which are described through topological effects emerged: integer, fractional quantum Hall effect, quantum anomalous Hall effect; to just mention derivatives of the Hall effect. But also new classes of materials appeared, including the topological insulators, semimetals, topological superconductors.

For all their important, ground-laying work on the field of topology in physics, all three mentioned physicists were awarded with the Nobel prize of physics in the year 2016.

In the following, the principles of topology in solid state physics will be discussed, based on reference [11].

### 1.2.1 Levi-Civita-Transport

First the Levi-Civita-Transport, also called parallel transport is highlighted. Figure 1.2a) shows a sphere on which a vector shown as green arrow is moved. The movement happens along the black line forming a triangle on the sphere. There are some specific requirements to the movement of the vector: it shall always be parallel to the surface of the sphere ( $\mathbf{R} \cdot \hat{\mathbf{n}} = 0$ ) and it is not allowed to rotate around the local normal vector  $\hat{\mathbf{n}}$  ( $d\mathbf{R} \times \hat{\mathbf{n}} = 0$ ), which is shown in blue. This type of transport is also called parallel transport. When moving the vector on a closed loop, after reaching point A again, it now has a phase offset of a certain angle which is called holonomy in mathematics. It is important to note, that this happens because of the geometrical implications of a movement on the sphere - if the surface is flattened and the process performed again,

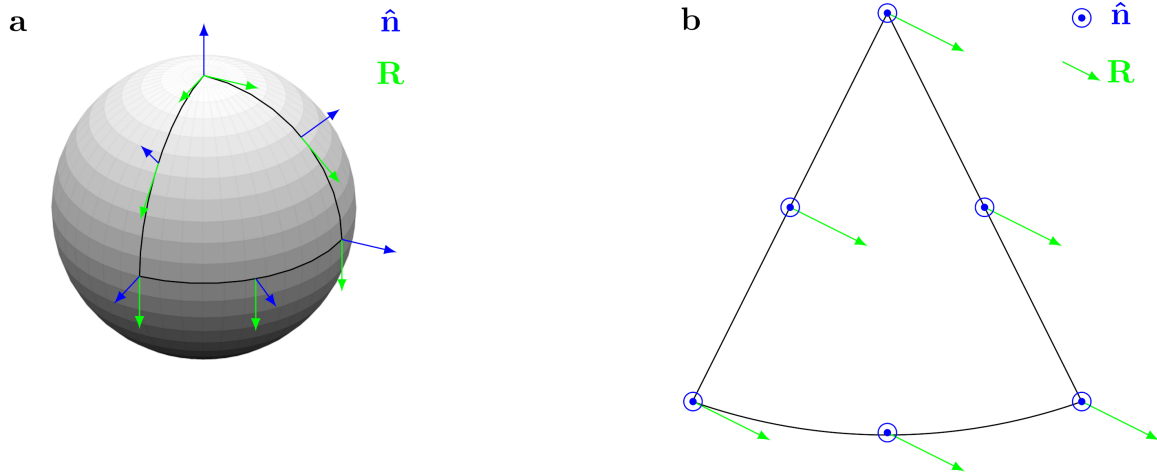


Figure 1.2: Closed loop parallel movement of a vector: a) on a sphere resulting in an offset and b) the same parallel transport on a loop on a plane.

no phase offset is gained, as shown in 1.2b.

The offset gained through the movement on a specific geometry is described by the Berry phase, which is also called the geometric phase.

## 1.2.2 Topological invariants

Topological invariants, like the Euler characteristic of geometric objects, can be found in the symmetry properties of the electronic band structure in the reciprocal space. In fact, all valence bands of a material have a topological property, contributing to an overall topological invariant of the material.

Coming back to the example with the mug and the torus, this can be transformed into physics using insulators. The hole would now correspond to a band gap. If different phases should be classified by means of topology, it has to be checked whether all points on valence bands will transform again into points on valence bands without accidentally closing the band gap. The ones not closing the band gap are the well known trivial insulators, whereas the others are topological materials.

In periodic crystalline solids the electron energy eigenstates can be written as a Bloch wave

$$\Psi_{\mathbf{k}}(\mathbf{r}) = e^{i\mathbf{k}\mathbf{r}} u_{\mathbf{k}}(\mathbf{r}) \quad (1.2)$$

where  $\mathbf{k}$  is the crystal momentum. It is now possible to define different Hamiltonians using topological invariants to describe and classify different topological phases in solid state matter.

The calculation of a topological invariant will be exemplarily discussed later in section 1.3.3.

### 1.2.3 The Berry phase

The Bloch wave is not only energy dependent, which determines many properties of solids, but also connected to the Berry phase through the momentum space dependency. To describe what the Berry phase postulated in 1984 by Michael Berry [12] is, one can have a look at the Levi-Civita-Transport on the sphere Fig. 1.2. The vector  $\mathbf{R}$  gained an angular offset while being moved along the closed loop path on the sphere. The only possibility to get rid of this phase factor is to exactly reverse the path which has been travelled.

It is possible to describe the state of the Bloch wave as a vector in a certain parameter space. The eigenstates of the Hamiltonian  $\mathcal{H}(\mathbf{R})$  can be evolved when changing parameters like  $\mathbf{R} = (r_1, r_2, \dots)$ . Thus, it is possible to move the Bloch state in a slow adiabatic process not only gaining the phase offset of the periodic lattice but another, purely geometric phase factor, as described by the Levi-Civita transport. This factor is called the Berry phase.

Looking at a vector  $\mathbf{R}$  moving along a path  $C$  in an adiabatic process through the system, the eigenstate at an arbitrary time  $t_0$  can be written as

$$|\Psi(t_0)\rangle = |n[\mathbf{R}(t_0)]\rangle \quad (1.3)$$

During this movement, the eigenvalue is depending on the time  $|n(t)\rangle$ . The phase offsets gained at this process can be written as:

$$|\Psi(t)\rangle = \underbrace{e^{i\varphi(t)}}_{\text{dynamic phase}} \underbrace{e^{i\gamma_n(t)}}_{\text{geometric phase}} |n[\mathbf{R}(t_0)]\rangle \quad (1.4)$$

With the path  $C$  being a closed ( $\mathbf{R}(0) = \mathbf{R}(T)$ ) directed curve, the Berry phase  $\gamma$  is

defined as:

$$\gamma_n = i \oint_C \langle n(\mathbf{R}) | -i \nabla_{\mathbf{R}} | n(\mathbf{R}) \rangle \cdot d\mathbf{R} \quad (1.5)$$

$$\gamma_n = \oint_C \mathbf{A}_n(\mathbf{R}) \cdot d\mathbf{R} \quad (1.6)$$

$$\mathbf{A}_n(\mathbf{R}) = i \langle n(\mathbf{R}) | -i \nabla_{\mathbf{R}} | n(\mathbf{R}) \rangle \quad (1.7)$$

Whereas  $\mathbf{A}_n(\mathbf{R})$  is the Berry potential. When performing a gauge transformation

$$|\tilde{n}(\mathbf{R})\rangle = e^{-i\beta(\mathbf{R})} |n(\mathbf{R})\rangle \quad (1.8)$$

a new set of states is obtained that differs from the original ones only by a phase factor depending on  $\mathbf{R}$ . For an open loop path this would change the Berry phase to

$$\tilde{\gamma}_n(t) = \gamma_n(t) + \beta(t) - \beta(0) \quad (1.9)$$

Looking at a closed loop, continuity would require

$$\beta(T) - \beta(0) = 2\pi m \quad (1.10)$$

with  $m$  being an integer. Out of this it directly follows that  $\gamma_n$  is invariant to transformations and quantized in units of  $2\pi$ .

The Berry phase is a powerful tool for unifying classical approaches to physics with the quantum mechanical ones. For example, it is required to fully explain the quantized versions of the Hall effect.

### 1.2.4 The Berry connection, Berry curvature and Chern number

The vector valued Berry connection, also called Berry potential:

$$\mathbf{A}_n(\mathbf{R}) = i \langle n(\mathbf{R}) | -i \nabla_{\mathbf{R}} | n(\mathbf{R}) \rangle \quad (1.11)$$

is a gauge-dependent potential, transforming as the following:

$$\tilde{\mathbf{A}}_n(\mathbf{R}) = \mathbf{A}_n(\mathbf{R}) + \nabla_{\mathbf{R}}\beta(\mathbf{R}) \quad (1.12)$$

The Berry connection can never be observed directly, but only on a closed loop path on the Berry phase. The Berry curvature can be written as

$$\boldsymbol{\Omega}_n(\mathbf{R}) = \nabla_{\mathbf{R}} \times \mathbf{A}_n(\mathbf{R}) \quad (1.13)$$

and is an anti-symmetric second rank tensor and the local, gauge invariant state of the geometric properties of the wave functions in the parameter space.

Looking at a closed path  $C$  as the boundary of the surface  $S$ , the Berry phase can be rewritten as:

$$\gamma_n = \int_S \boldsymbol{\Omega}_n(\mathbf{R}) \cdot d\mathbf{S} \quad (1.14)$$

As noted already, the closed loop Berry phase is quantized in units of  $2\pi$ . The factor is the so called Chern number and defined through the Chern theorem:

$$C_n = \frac{1}{2\pi} \int_S \boldsymbol{\Omega}_n(\mathbf{R}) \hat{\mathbf{n}} \cdot d^2\mathbf{R} \quad (1.15)$$

This term is the equivalent to the Gauss-Bonnet theorem to classify the topology of an enclosed surface.

This term is often discussed using analogons from electrodynamics. The term  $\boldsymbol{\Omega}_n(\mathbf{R})$  can be treated as a magnetic flux density and  $\mathbf{A}_n(\mathbf{R})$  is its vector potential. The Chern number would correspond to the total flux of  $\boldsymbol{\Omega}_n$  through the surface  $S$ , just like a magnetic monopole within a space encapsulated by  $S$  would behave.

This theorem can be used to classify the topological properties of solids. A 1D Brillouin zone does have the same topology as a closed loop, whereas a 2D Brillouin zone is equivalent to a two dimensional torus, as seen in Fig. 1.3. Thus, an integration over the Brillouin zone is equivalent to integrating over a mathematical body. Fig. 1.3 shows exemplary possible paths of bands and their respective locations in the corresponding bodies.

The overall Chern number is calculated by summing up Eq. 1.15 over all valence bands of the system:

$$C = \sum_{n=1}^N C_n = \frac{1}{2\pi} \sum_{n=1}^N \int_{BZ} \boldsymbol{\Omega}_n(\mathbf{k}) \hat{\mathbf{n}} \cdot d^2\mathbf{k} \quad (1.16)$$

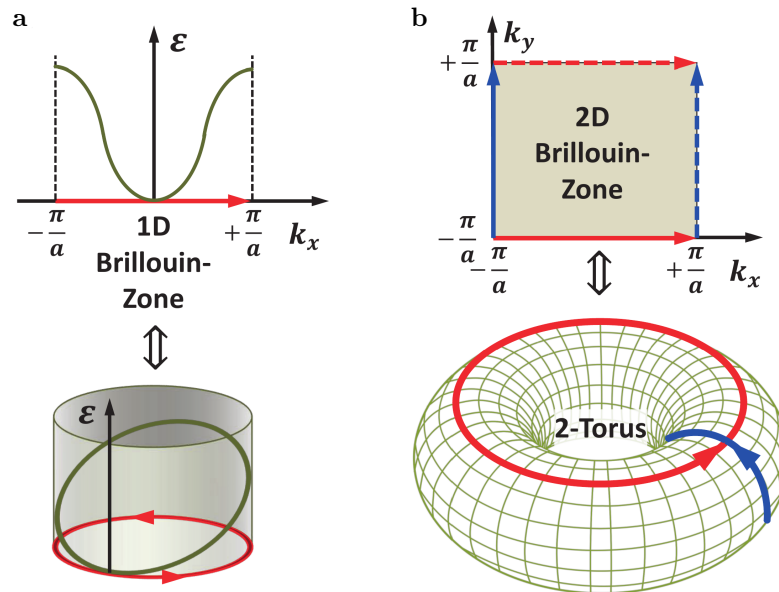


Figure 1.3: a) 1D and b) 2D band structure schematics and their topological equivalent objects. Picture taken from [11].

Like the integral of the Gaussian curvature gives a topological invariant through the Euler characteristic, the integral of the Berry curvature gives the Chern number. This shows quite well, that the concepts of topology originating from mathematics are suited very well to classify materials with different topological properties in physics

## 1.3 Topological insulators

After introducing the basic theoretical aspects of topology, their presence in specific solid state materials and phenomena will now be highlighted. In this chapter, topological insulators will be discussed based on references [13, 14], first starting the observation of the quantized Hall effect and then generalizing it to the definition of weak and strong topological insulators.

### 1.3.1 The quantized Hall effects

The Hall effect is a phenomenon discovered by E. H. Hall in 1879 [15]. It describes the change in a voltage perpendicular to a flow of current in a conductor, when applying a perpendicular external magnetic field. The voltage arises, as the electrons in the sample



are forced to the side of the sample due to the Lorentz force. If enough electrons are on one side, a static electric field rises up and balances out the Lorentz force - resulting in the electrons to go their original way. This field can be measured as a voltage change, perpendicular to the current and is called Hall voltage.

100 years after the Hall effect, von Klitzing discovered, that there can be a “quantization” of the Hall conductivity. This alteration is called the quantum Hall effect, appearing in materials thin enough to restrict the movement of the electrons along one axis [16]. The derivations of the original Hall effect quickly became an important field of research in solid state physics.

### The quantum integer Hall effect

Fig. 1.4 shows the behaviour of the Hall conductance within a thin material slab in a magnetic field. The electrons in the bulk are “locked” in place by a circular movement with a cycling frequency  $\omega_C$ , inhibiting any current to flow. This movement is quantized in the following way:

$$\epsilon_m = \hbar\omega_c(m + 1/2) \quad (1.17)$$

If only  $N$  Landau levels are filled and the rest is kept empty, the material would be a normal insulator, as the energy gap would separate the filled and unfilled states. Unlike in regular insulators, in the presented case the electrons at the edge of the material drift along the edge due to an electric field, causing a Hall current  $\sigma_{xy}$  to flow on the surface. Soon after its discovery, it was realized that the current flowing on the surface is forming directed, scatter-free conduction channels in the material. It is especially interesting, as the electrons can not be scattered backwards, as the conduction channels of opposing direction are separated by the insulating bulk, as seen schematically for two of the four edges in Fig. 1.5a.

$$\sigma_{xy} = N \frac{e^2}{h} \quad (1.18)$$

Figure 1.4b shows an exemplary measurement of the Hall current in the quantum Hall regime. The steps of  $\sigma_{xy}$  seen in the dataset correspond to equation 1.18 and were

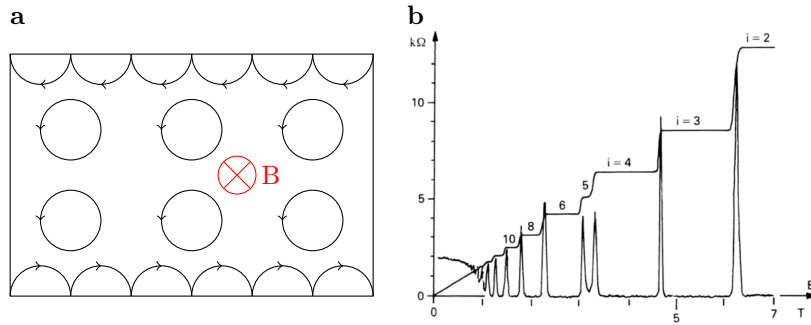


Figure 1.4: a) The “locked” movement of electrons in a strong magnetic field leading to the quantum hall effect. The edge states (indicated top and bottom) cause a current through the hopping of an electron, whereas the electrons in the bulk are locked in place. b) Exemplary experimental data of the quantized Hall current  $\sigma_{xy}$ . Panel b) taken from [17].

observed by von Klitzing. Thouless, Kohmoto, Nightingale and den Nijs [8] showed, that  $\sigma_{xy}$  computed using the Kubo formula [18] has the same form as the formula of the total Chern number of the system:

$$n_m = \frac{\pi}{2} \int d^2k, F_m \quad (1.19)$$

$$n = \sum_{m=1}^N n_m \quad (1.20)$$

thus, showing, that  $N$  from equation 1.18 is identical to the Chern number  $n$ . This explains the robust quantization of  $\sigma_{xy}$  and the presence of a quantized Hall coefficient can therefore be viewed as a strong indication for topological states existing in the material. The value of  $n_m$  is often called TKNN invariant [8] within this context. The Chern number can also be written as a combination of different Chern classes  $C_m$ , being integer values specific to each band  $m$  of the system. With this it is possible to rewrite the formula of the Hall conductivity to utilize the Chern classes:

$$\sigma_{xy} = \frac{e^2}{2\pi\hbar} \sum_m C_m \quad (1.21)$$

The sum is over all filled Bands  $m$ . This formula is called the TKNN formula.

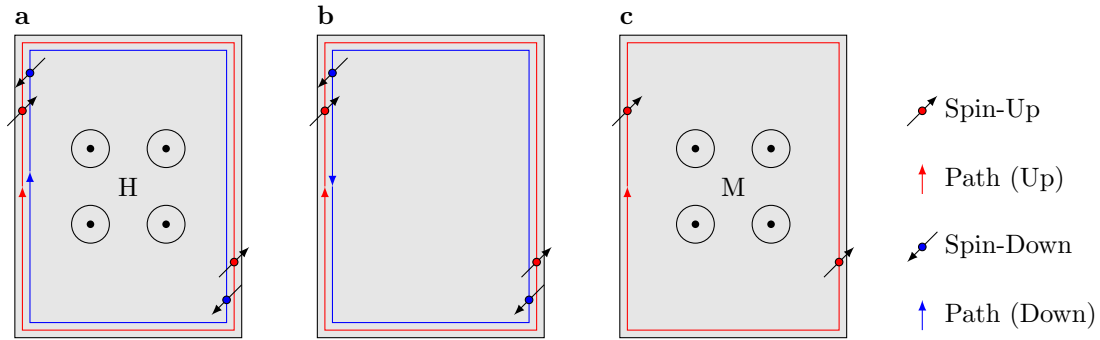


Figure 1.5: Schematic comparison of all quantized Hall effects. a) quantum Hall effect.

A strong magnetic field ( $H$ ) causes conducting edge states with electrons moving along them in one direction. b) quantum spin Hall effect. Spin currents along the edge of the material, with opposing directions resulting in a zero net current. c) quantum anomalous Hall effect. A magnetization ( $M$ ) of the material suppresses one spin direction. Picture derived from [19].

### The quantum spin Hall and quantum anomalous Hall effect

Yet, the quantized Hall effect is only present in the vicinity of strong magnetic fields. It has been shown in 1988, that instead of using an external magnetic field, the electrons can also be held in place by the presence of strong spin-orbit coupling (see section 1.3.2). This effect is called the spin Hall effect [20]. In comparison to the Hall effect, in the case of the spin Hall effect no charge current is present at the edge of the material, but a spin current. Due to the lack of a directing force, the spin current of the spin Hall effect is not flowing into one specific direction, but both, spin-up and spin-down, are drifting in opposing directions, causing the net spin current of the system to be zero.

A version of the quantum spin Hall effect, where one of the spin channels is suppressed was presented in 1881, namely the anomalous Hall [15] effect. The suppression of one channel can be achieved by strong magnetic fields, either external or by introducing an internal magnetic field through doping of suited elements.

For both effects, quantized equivalents were realized within the last ten years [21, 22]. All three quantized versions, the quantized Hall effect, the quantized spin Hall effect as well as the quantized anomalous spin Hall effect are shown schematically in Fig. 1.5. The edge currents are shown in red and blue with arrows indicating their

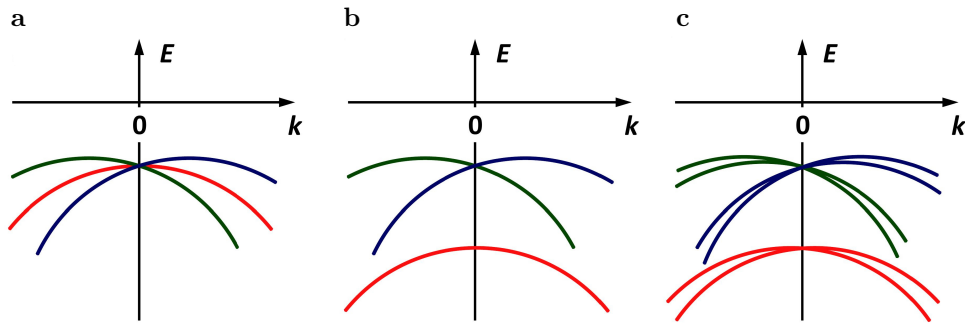


Figure 1.6: Influence of spin-orbit coupling on a p-band close to the center of a Brillouin zone. a) Sixfold degenerate point at  $k = 0$  with no spin-orbit interaction. b) Crystal with inversion symmetry: spin-orbit coupling splits the sixfold degeneracy into a 4-fold and a 2-fold degenerate point. c) Crystal without inversion symmetry: additional lifting of the Kramers degeneracy. Picture taken from [11].

directions. Spins are indicated by black arrows.

Topological insulators are materials showing an insulating bulk behaviour as well as surface conductivity at the same time. This is similar to the behaviour described by the quantized spin Hall effect. Important aspects of their bandstructure, leading to topological states in these materials will be discussed on the following pages.

### 1.3.2 Spin-Orbit coupling

Effects of topological insulators are greatly influenced by spin-orbit interactions of their electrons. Spin-orbit coupling describes the interaction between the spin of an electron and its orbital momentum. This interaction is the major cause of the splitting of the energy levels, as seen for example in the fine structure of the elements. The strength of this interaction is mostly dependent on the orientation of the spin to the orbit.

In solids, the spin-orbit interaction plays only a small role within the overall energy scale of the core levels. As for electrons bound to atoms the influence of the spin-orbit coupling is usually relatively small. It can usually be observed as a small perturbation within this energy scale. Yet, it becomes more important when only looking into the bandstructure close to the Fermi level.

When discussing spin-orbit coupling, an important aspect of spin-orbit coupling in

combination with systems that have time reversal symmetry is the Kramers theorem or degeneracy. Described by H. Kramers [23], it states, that every energy eigenstate of a system of half-integer total spin with time reversal symmetry is always doubly degenerate. An important result is, that bands with spin-up and spin-down electrons will not split because of spin-orbit coupling if the crystal does possess time reversal symmetry, yet multiple bands crossing in a point might still be split. The influence of spin-orbit coupling on both symmetry types is schematically shown in Fig. 1.6. It is seen, that in case of a time reversal symmetry the three bands get separated, but stay doubly degenerate themselves. If there is no such symmetry present, these bands split up themselves in regards of their local spin polarization.

### Band inversion

The effect of band inversion describes a situation present in the band structure of selected insulators, where the parity in certain conduction and valence bands close to the Fermi level is inverted.

Fig. 1.7 shows a schematic overview of three different schematic band configurations close to the Fermi level. Panel 1.7a shows a regular, trivial insulator. Valence and conduction bands are well separated by a band gap and the Fermi level is located within this band gap. In panel b, these two bands are overlapping, creating crossing points at the Fermi level at positions  $\pm\mathbf{k} \neq 0$ . The parity of the bands, indicated with + and - within the figure, are not changed, introducing the opposing parities into the valence or conduction bands. Due to the different symmetries of the intersecting bands, the crossings of the bands at  $\mathbf{k} \neq 0$  are forbidden. Due to this, a band structure configuration as shown in Fig. 1.7c will appear, avoiding the crossings. While the crossings are avoided, the inverted parities of the bands are preserved in the band structure.

In solids, band inversions may occur if bands close to the Fermi level are split by spin-orbit coupling. The parts of the bandstructure, where the bands are inverted, are likely hosts to topological, nontrivial properties. This makes these features interesting for spectroscopy, as inverted bulk bands are easier to resolve than fine topological details. More details about measuring of topological states are presented in chapter 2.1.

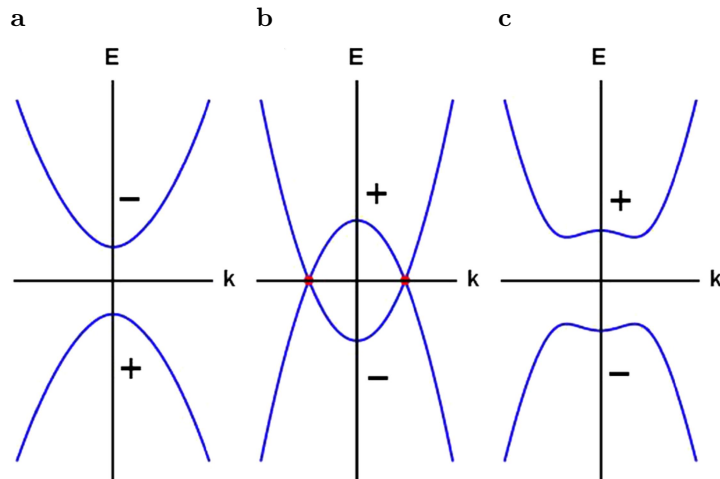


Figure 1.7: Schematic of a band inversion leading to topological states with the parity of the bands shown with + and -. a) Trivial insulating band structure. The bands are doubly degenerate. b) Overlapping bands with forbidden simple crossings at  $k \neq 0$  due to symmetries. c) Gapped out state of the variant shown in b) avoiding the forbidden crossings. The parity of the bands is inverted. Picture taken from [24].

### The bulk boundary correspondence

The band gap of a trivial insulating material can be viewed as boundary between the bulk and a vacuum. As both are of the same genus, everything simply translates at the surface without any implications. On the contrary, if the material is a topological material, on the surface transition is not simple anymore. The bulk now has a genus of one, whereas the gap still has a genus of zero. As described earlier, this can be viewed as projecting all points of a torus on top of a sphere - which is not possible without closing the hole or, in this case, the band gap. The solution is, that conducting states appear, which cross the gap - the topological surface states.

Fig. 1.8 shows electronic states in dependency of the crystal momentum at the edge of a  $\mathcal{T}$  invariant 2D insulator. When looking at the Fermi surface between two Kramers degenerate points  $\Gamma_a$  and  $\Gamma_b$  located within the Brillouin zone the following:  $\Gamma_a = 0$ ,  $\Gamma_b = \pm\pi/a$ , spin-orbit coupling will split the the degeneracy between these states. Due to the Kramers degeneracy, the degeneracy at  $\Gamma_a$  and  $\Gamma_b$  is not lifted.

The states between  $\Gamma_{a,b}$  can now connect in two different ways: either pairwise as seen

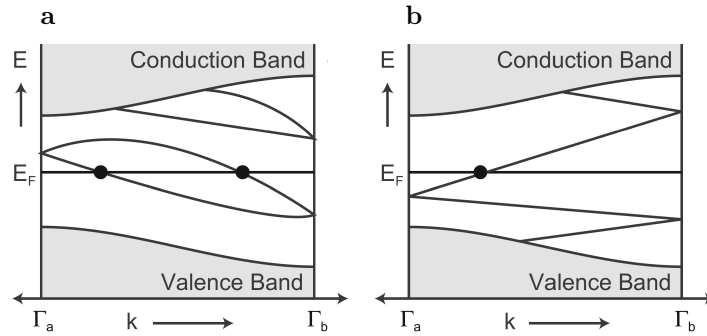


Figure 1.8: Bulk boundary correspondence of a) a trivial topological material and b) a nontrivial topological material. Picture taken from [14].

in Fig. 1.8a where the states present can be eliminated by pushing them out of the gap, or the state crosses the gap an odd number of times, as shown in Fig. 1.8b. In the latter case, these crossings can not be eliminated by moving them out of the gap and are thus protected by symmetry, leading to topologically protected boundary states.

### 1.3.3 The $\mathbb{Z}_2$ invariant

As mentioned in the introduction, Thouless, Kohmoto, Nightingale and den Nijs (TKNN) showed in an important paper [8], that the integer Hall conductivity is exactly the Chern number. This comparison was achieved through the TKNN formula shown in 1.19.

As the TKNN invariance is always 0 in this case, yet the material can still be topological, a second invariant is needed, the so called  $\mathbb{Z}_2$  invariant, which can be either  $\nu = 0, 1$ .

The  $\mathbb{Z}_2$  invariant can be interpreted as a global parity of the system. In possible topological insulators this can be calculated by taking all translation invariant momenta on the 2D surface Brillouin zone and multiply the parities of all completely filled bands in all points. Naming the translation invariant points  $\Gamma_a$ , the Bloch states  $u_m(\Gamma_a)$  are parity eigenstates with their eigenvalues  $\epsilon(\Gamma_a) = \pm 1$  - meaning the parity is either 1 or  $-1$ . The overall  $\mathbb{Z}_2$  invariant can then be calculated by calculating the product over the Kramers pairs of all the occupied bands and solving it for  $\nu$ :

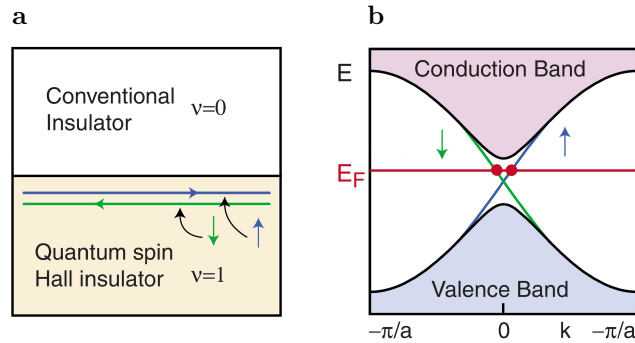


Figure 1.9: a) Schematic of the surface behaviour of a quantum spin Hall insulator. b) Band structure scheme of this state, with bulk bands shown as filled areas and surface states shown in lines. Picture taken from [13].

$$\delta_a = \prod_m \epsilon_m(\Gamma_a) \equiv (-1)^\nu \quad (1.22)$$

This method can be used to easily classify predicted materials in terms of possible topology.

### 1.3.4 3D topological insulators

Topological surface states can be present in both, 2D and 3D materials. In 2D materials, this corresponds essentially to the quantum spin Hall edge state described earlier. The interesting parts of the bulk and surface bandstructure of these states are highlighted in Fig. 1.9, where panel a highlights the general surface area and panel b shows an exemplary energy-momentum cut of the aforementioned surface area.

3D topological insulators are the 3D generalization of the 2D quantum Hall state of matter. These materials can be characterized by four  $\mathbb{Z}_2$  topological invariants:  $(\nu_0; \nu_1\nu_2\nu_3)$ . These invariants are reflecting the four translation invariant points of a Brillouin zone, shown as filled or empty circles in Fig. 1.10 as well as  $\Gamma_1$ - $\Gamma_4$  in Fig. 1.11. The edge states of the 2D topological insulator, seen in Fig. 1.9, combine to a 2D surface feature on top of the 3D Brillouin zone, forming the feature described by the red lines in Fig. 1.11a. If such states are present in a material, they must be Kramers degenerate as described in section 1.3.2.



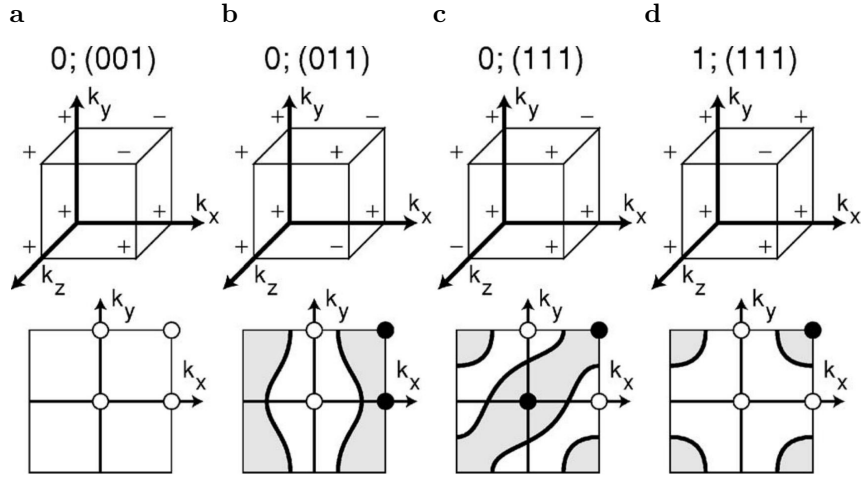


Figure 1.10: Overview of different  $\mathbb{Z}_2$  configurations  $\nu_0; (\nu_1\nu_2\nu_3)$  in 3D topological insulators a) - d). The top row shows the value of  $\delta_a$  at the invariant points  $\Gamma_a$ . The bottom row depicts the 001 surface for each configuration, with the thick lines being possible topological states. Picture taken from [25].

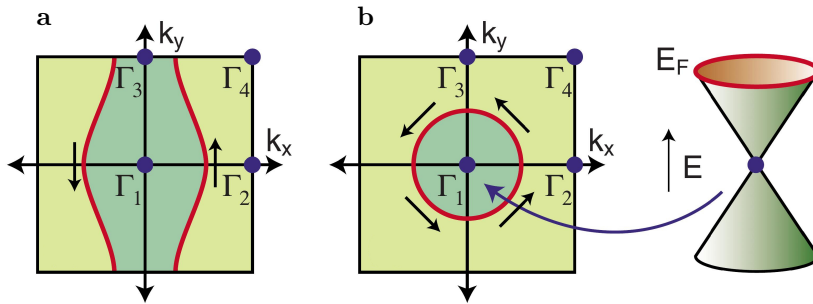


Figure 1.11: Fermi surface of a) weak topological insulators and b) strong topological insulators. c) Energy dependency of the topological states in strong topological insulators. Picture taken from [25].

Moving away from these points, this degeneracy is lifted through the spin-orbit interaction. These Kramers degenerate points form 2D Dirac points in the surface band structure. Surface states in topological insulators can be either of the form shown in Fig. 1.11a, named weak topological insulators, or as shown in Fig. 1.11b, named strong topological insulators. The difference is found in the number of times, the surface states are crossing any direct connections between two arbitrary translation invariant points on the surface. Taking two of the four  $\Gamma_1$ - $\Gamma_4$  invariant points,  $\Gamma_a$  and  $\Gamma_b$ , the line between them will cross the surface states either an even or an odd number of times. If

the states are crossed an odd number of times, this means that these are topologically protected. Which behaviour can be found in the material, is given through the  $\mathbb{Z}_2$  topological invariant component of  $\nu_0$ : if  $\nu_0 = 0$  the material is called a weak topological insulator, whereas if  $\nu_0 = 1$  the material is called a strong topological insulator.

### Weak topological insulators

Imagine a simple topological insulator build out of a stack of 2D quantum spin Hall insulators. Their topological edge states will combine to anisotropic surface states, resembling the look of the red lines in Fig. 1.11a. The resulting Fermi surface shows nontrivial connectivity between  $\Gamma_1$  and  $\Gamma_2$  as well as  $\Gamma_3$  and  $\Gamma_4$ . In these weak topological insulators, the first index  $\nu_0$  is always zero. The set of indices  $(\nu_1\nu_2\nu_3)$  can be interpreted as Miller indices, describing the orientation of the layer. Possible configurations of these invariances are shown in Fig. 1.10, including possible surface states which could appear when these are present.

These states are not protected by translation symmetry. The states are present on clean surfaces, but can appear localized for perturbations in the crystal lattice.

### Strong topological insulators

Strong topological insulators are described with  $\nu_0 = 1$ . Contrary to weak topological insulators, the strong counterparts can not be constructed out of stacking 2D quantum spin hall insulators. Fig. 1.11b shows the simplest case of a strong topological insulator. The Fermi circle encloses one Kramers degenerate Dirac point in this picture, but higher odd numbers are also possible.

In strong topological insulators, as shown in [13], the simplest case of a single Dirac point can be described by the Hamiltonian

$$\mathcal{H}_{surface} = -i\hbar\nu_F\sigma\nabla \quad (1.23)$$

$\sigma$  characterizes the spin.

These surfaces are similar to graphene, but instead of having four Dirac cones, only one Dirac cone is present - which appears to violate the fermion doubling theorem [26]. But

the partnering Dirac cones are just residing on the opposite surfaces. These surface states form a unique 2D topological metal [25, 27] resembling half an ordinary metal - which has spin up and down states distributed all over the Fermi surface, whereas a strong topological insulator shows only non degenerate states. As  $\mathcal{T}$ -symmetry is still present, it is required that the states at  $\mathbf{k}$  and  $-\mathbf{k}$  have the opposite spin. This can be achieved by rotating the spin around the center, resulting in the circle visible in Fig. 1.11b as well as a nontrivial Berry phase. An electron rotating on this line will gain a spin offset of  $2\pi$  - resulting in a  $\pi$  Berry phase.

## 1.4 Semimetals

Semimetals are a class of materials between regular metals and insulators. These materials still have overlapping bulk and valence bands, but the overall Fermi surface cross section is reduced to a minimum. It has been found, that these tiny overlappings in the band structure are hosts to unusual features. In the following chapter, an introduction into such materials and their properties will be given, based on reference [24].

### 1.4.1 The Dirac equation

The Dirac equation was postulated 1928 by Paul Dirac [28]. It is a very important principle in physics, as it unified the special relativistic theory together with quantum physics, both being quite new concepts in 1928. Due to this equation quantum electrodynamics as well as quantum field theory were made possible.

The equation is describing a spin 1/2 particle - a Fermion - which is required to be different from its antiparticle. This fact makes this equation interesting from the point of particle physics, as it is the first prediction of antimatter.

The equation is of first order, both in space and time and can be written as:

$$(i\hbar\gamma^\mu\partial_\mu - mc)\psi = 0 \tag{1.24}$$

with  $\gamma^\mu$  being  $4 \times 4$  matrices

$$\gamma^0 = \begin{pmatrix} I_2 & 0 \\ 0 & -I_2 \end{pmatrix} \quad \gamma^1 = \begin{pmatrix} 0 & \sigma_x \\ -\sigma_x & 0 \end{pmatrix} \quad \gamma^2 = \begin{pmatrix} 0 & \sigma_y \\ -\sigma_y & 0 \end{pmatrix} \quad \gamma^3 = \begin{pmatrix} 0 & \sigma_z \\ -\sigma_z & 0 \end{pmatrix} \quad (1.25)$$

created out of the identity matrix  $I$  and the Pauli matrices  $\sigma_{x,y,z}$ :

$$\sigma_x = \begin{pmatrix} 0 & 1 \\ 1 & 0 \end{pmatrix} \quad \sigma_y = \begin{pmatrix} 0 & -i \\ i & 0 \end{pmatrix} \quad \sigma_z = \begin{pmatrix} 1 & 0 \\ 0 & -1 \end{pmatrix} \quad (1.26)$$

For this equation, simplifications for certain edge cases appeared quite quickly. The most noteworthy ones are the Majorana equation and the Weyl equation. Both will be introduced later in this chapter.

It has been believed for a long time, that the Dirac physics only plays a role in high energy physics. As the main energy scales of interest in condensed matter physics are much smaller than the rest mass of an electron, it was believed that a nonrelativistic description of the electrical properties would be sufficient to describe the electronic properties of solids and thus no Dirac physics is needed to be involved.

It turned out, that the quantum theory is indeed a key to correctly analyse the band structure as well as spin-orbit coupling requires fully relativistic calculations to be correctly reproduced.

Research in graphene started to lead to a reconsideration of the usage of the Dirac physics in condensed matter. As it turned out, the Dirac equation very well describes the behaviour of the electrons close to the Fermi surface. Due to that, the Dirac equation became an important tool to describe nontrivial gapless materials in the recent years and overall lead to a “new field” in solid state physics.

### Dirac semimetals

Dirac semimetals are materials, hosting linear, doubly degenerate bandcrossings close to the Fermi level. The points of these crossings are therefore fourfold degenerate and can be described by the Dirac equation. Fig. 1.12 shows a schematic phase transition from a trivial insulator to a topological insulator. The Dirac semimetal fits in this picture as the critical point when the bands touch, before the bands open again with band inversion being present.

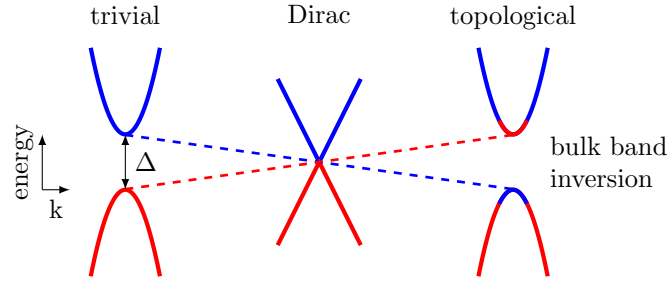


Figure 1.12: Transition from a trivial insulator to a topological insulator. The bands close in until they reach a critical point where they touch - the Dirac semimetal. Continuing in this scheme, the bands open again with band inversion being present as topological insulator. Picture derived from [29].

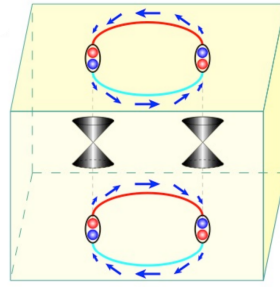


Figure 1.13: Schematic Brillouin zone of a Dirac semimetal. The Dirac cones are located in the Bulk states, and their projections on the surface Brillouin zone are connected by spin-polarized circular topological states. The direction from the top and bottom spin are opposing each other. Picture taken from [30].

The topological states of the Dirac semimetals on the surface Brillouin zone are describing a full circle, as depicted in Fig. 1.13. Dirac semimetals can appear both, with fermions of vanishing or non-vanishing mass. In the case of a non-vanishing mass, a small gap opens up in the Dirac cone.

### 1.4.2 The Majorana equation

Suggested by Ettore Majorana in 1937 [31, 32], the Majorana equation is a real wave equation

$$(i\hbar\gamma^\mu\partial_\mu - mc)\Psi = 0 \quad (1.27)$$

$$\Psi = \Psi_c \quad (1.28)$$

with  $\Psi_c$  being the charge conjugate of  $\Psi$ . Due to this requirement, the only feasible solution is an uncharged particle, which also is its own antiparticle.

As all topological matter, Majorana Fermions gained a lot of interest lately, especially when discussing the interplay of topological matter with superconducting materials [33, 34].

### 1.4.3 The Weyl equation

The Weyl equation, suggested by Hermann Weyl in 1929 [35], is another edge case of the Dirac equation in the terms of vanishing mass. Due to that, the Dirac equation reduces to:

$$i\hbar\gamma^\mu\partial_\mu\psi = \gamma^\mu\partial_\mu\psi = 0 \quad (1.29)$$

For a long time, the neutrino was handled as a candidate of a Weyl fermion. After the discovery of a nonvanishing neutrino mass, no fundamental particles were left in high energy physics satisfying the conditions of the Weyl equation. But with the rise of nontrivial electronic properties in solids, topological insulators and Dirac semimetals, realizations of Weyl Fermions in solid state matter were found. In comparison to high energy physics, solid state matter does change the boundary conditions quite substantially. In a high energy point of view, all degrees of freedom are available, which does not have to be the case in solids. Due to this, different types of Weyl Fermions have emerged. The most noteworthy types of Weyl fermions apart from the “classical”, or type-1 Weyl state are the type-2 Weyl [36] state and the spin-1 Weyl state [37].

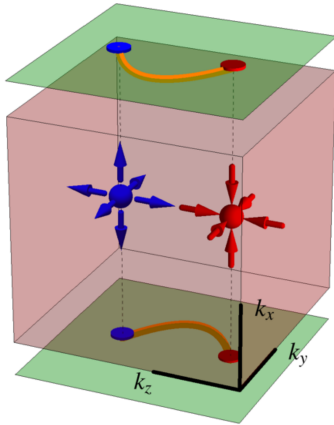


Figure 1.14: Schematic structure of a Weyl semimetal.

There are pairs of Weyl points of opposite chirality. Surface features appear on the Fermi surface between the projections of the Weyl points and do form a “loop” throughout the system. Picture taken from [38]

#### 1.4.4 Weyl semimetals

Weyl fermions are hosted in materials, possessing a topological protected linear crossings of non degenerate bands in 3D materials. These crossings can be viewed as spin split versions of the crossings seen in Dirac semimetals. This causes the Weyl points to always appear in pairs with each Weyl point corresponding to one spin direction. It is required, that the overall chirality of the system must vanish - an uneven number of Weyl points is therefore not possible. A scheme of a Brillouin zone hosting Weyl points is shown in Fig. 1.14. The chirality of the points is indicated by the arrows pointing either towards or away from them. The green planes are the surface Brillouin zones, where the projections of the Weyl points are connected by Fermi arcs - dispersions originating from the topological states in these materials.

Weyl points have unique properties and a lot of work has gone into the search for materials hosting these. One major difficulty is, that these materials need to have either broken time reversal  $\mathcal{T}$  or inversion symmetry  $\mathcal{P}$ , as otherwise Weyl points of opposing chirality will overlap and annihilate. The broken symmetries prevent this, protecting these features. These symmetries will now be discussed in more detail.

##### Time reversal symmetry $\mathcal{T}$

Broken time reversal symmetry  $\mathcal{T}$  allows the simplest configuration of Weyl nodes possible in a Weyl semimetal. With time reversal symmetry broken, but inversion symmetry intact, the minimal amount of Weyl nodes is one pair of opposite chirality.

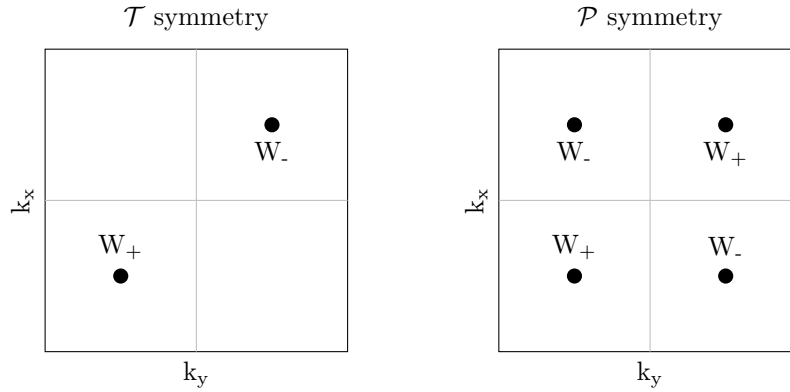


Figure 1.15: Schemes of the Brillouin zones and the simplest possible Weyl point configurations for the  $\mathcal{T}$  and  $\mathcal{P}$  symmetries.

Additionally, it is guaranteed that these points are at the same energy. To check for the existence of these points, the parity of the eigenvalues in the time reversal invariant momenta (TRIM) can be used.

The inversion symmetry requires that the Weyl node at  $\mathbf{k}$  is not equal to  $-\mathbf{k}$ .

### Inversion symmetry $\mathcal{P}$

If  $\mathcal{T}$  is present, the only possibility to host Weyl points is to have  $\mathcal{P}$  broken symmetry. In this case, the minimum number of Weyl points is now multiples of four. Due to the symmetry operations allowed, the Weyl node at  $\mathbf{k}$  is also present at  $-\mathbf{k}$ . As there are now 2 Weyl nodes of same chirality and as the overall chirality of the Brillouin zone must vanish, there are two more Weyl points of the other chirality.

### Surface states

As already mentioned, the projections of the Weyl nodes are connected by the Fermi arcs on the surface Brillouin zone. This is again shown in Fig. 1.16 for the slightly special case, when the Weyl nodes are located directly at the Fermi level. The surface state is connecting the two cones of opposing chirality located at  $\pm\mathbf{k}_0$  in the surface Brillouin zone. When cut at  $E_F = 0$  form the so called Fermi arcs terminating at the projected Weyl nodes. This behaviour can be directly derived from the Berry flux, with the Weyl nodes acting as sinks and sources.



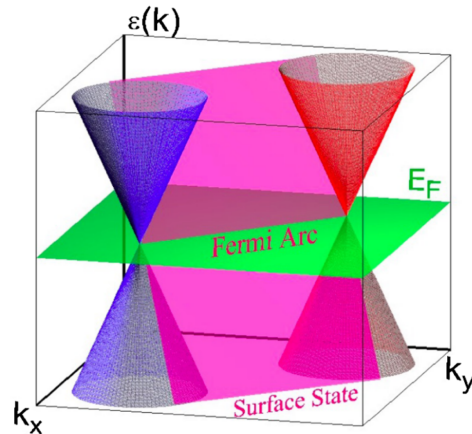


Figure 1.16: Topological surface state connecting two Weyl cones in a 3D Brillouin zone of a Weyl semimetal. The Fermi level is highlighted as green sheet.

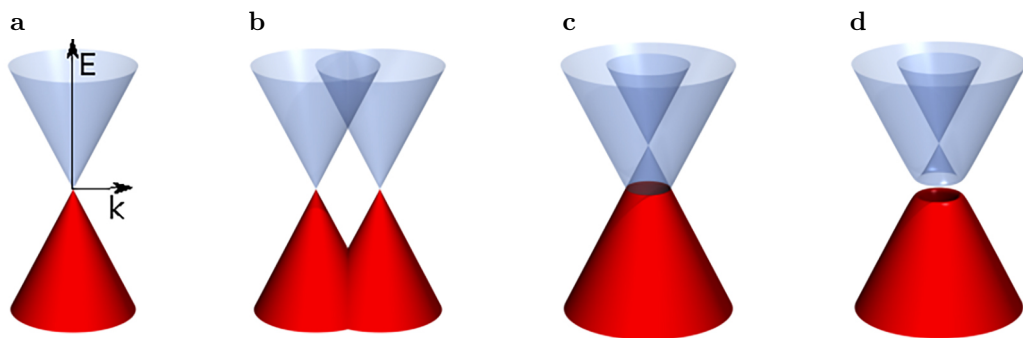


Figure 1.17: Topological states of Dirac and Weyl semimetals. a) normal Dirac semimetal. b) Weyl semimetal. c) line node semimetal, d) magnetic semiconductor. Picture taken from [39].

### Interplay of Dirac and Weyl semimetals

It is possible to transform massless Dirac cones into two Weyl cones - essentially splitting them into a spin-up cone and a spin-down cone. Fig. 1.17 shows possible transformations. The most common splitting is in  $k$ -space, where due to magnetic fields or strain the spins separate into their own cones, creating a Weyl phase in the material. But, the spin can also separate in energy, creating so called line node semimetals.

### Type-2 Weyl semimetals

Until now, only type-1 Weyl semimetals have been discussed. The topological states within these materials can be visualized as upward cones within the band structure, as visualized in Fig. 1.17a. But Soluyanov et al. [36] showed, that this is no necessity. They proposed, that taking the kinetic energy term of the Weyl equation into account allows for a set of different properties. Looking at the Hamiltonian of the Weyl fermions

$$H(\mathbf{k}) \sim f_0(k_0) + v_0 \delta \mathbf{k} + \sum_{x,y,z} \mathbf{v}_\mu \delta \mathbf{k} \sigma^\mu \quad (1.30)$$

$$(1.31)$$

it can be viewed as

$$H = T + U \quad (1.32)$$

where T stands for the kinetic energy and U for the potential energy. There are now three possible relations between the kinetic and the potential energy of the system:

$$\begin{aligned} T = 0, & \quad \text{Weyl-I Fermion} \\ T \neq 0, & \quad \text{small anisotropy around Weyl point} \\ T \gg U & \quad \text{tilting of structure, "type-2 Weyl"} \end{aligned} \quad (1.33)$$

The first case,  $T = 0$ , does satisfy the Lorentz symmetry in vacuum. These materials have been called type-1 Weyl semimetals. In contrast to a particle in vacuum, Lorentz symmetry can be broken in a crystal close to an isolated twofold bandcrossing. This is the case for the third option where  $T \gg U$ . The band structure gets tilted along one symmetry axis, resulting in a new momentum space geometry of the whole system. These materials show open constant energy curves on the Fermi surface in addition to topological surface states.

The two different cones are depicted in Fig. 1.18. Tilting the cones crucially influences the properties of the type-2 systems, as it introduces angular dependencies to most properties. Most noteworthy being the angular dependency of the Hall resistivity as well as the magnetoresistance. Overall, the density of states close to the Fermi level is quite different from the type-1 Weyl semimetals.

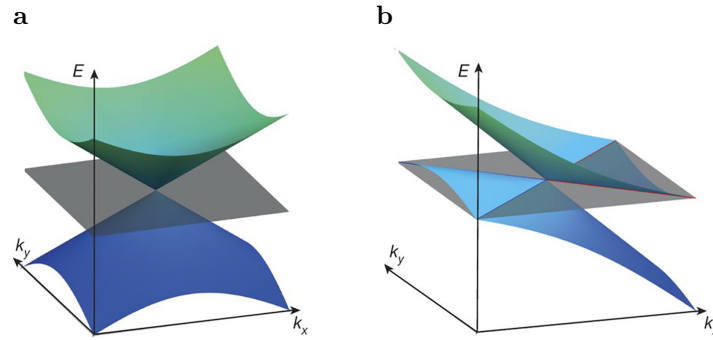


Figure 1.18: Schematic bulk band structure of a) type-1 and b) type-2 Weyl semimetals.

Picture taken from [36].

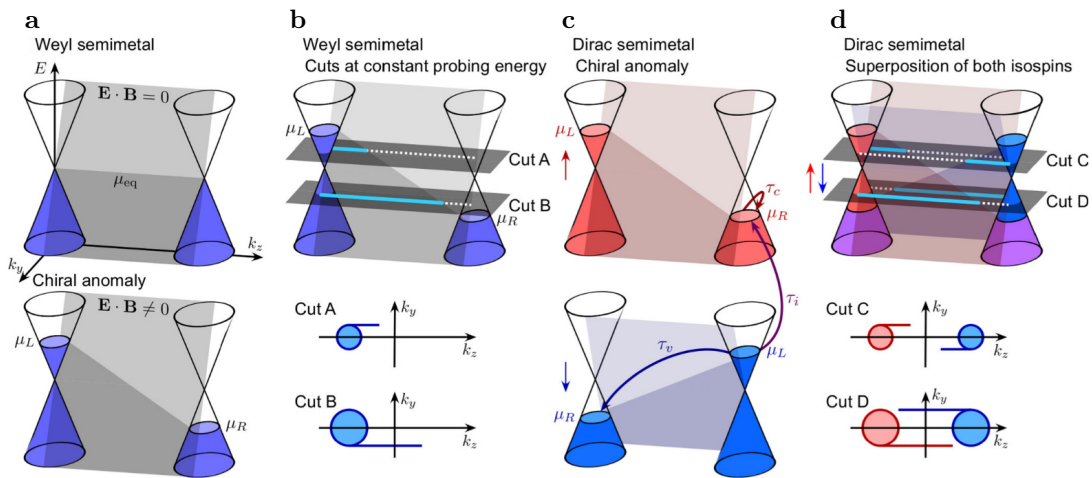


Figure 1.19: The chiral anomaly in Dirac and Weyl semimetals. Picture taken from [40].

### 1.4.5 The chiral anomaly

Quantum anomalies, appearing when symmetries in materials are broken during quantization, are very interesting as they usually introduce unique material properties. With the experimental realization of the Weyl semimetals and their low energy description using chiral fermions, the anomalous breaking of the chiral anomaly was discussed in more detail. The term chiral anomaly describes the anomalous breaking of the conservation of the chiral current in materials - resulting in an imbalanced amount of states of left and righthanded chiral fermions.

Fig. 1.19 shows the impact of the chiral anomaly in Dirac and Weyl semimetals in more detail.

In a normal state, the Weyl cones of a system are equally filled, one with left and one with right handed chiral fermions. It is now possible, to pump fermions from one cone to another using nonorthogonal electric or magnetic fields, as shown in Fig. 1.19b, which causes a tilt of the chemical potential. When looking at Fig. 1.16, the green sheet resembling the chemical potential now cuts the pink surface state diagonal, resulting in an optically tilted surface state, as seen in 1.19a bottom. These Fermi arcs are still connecting the two Weyl nodes at their different energy levels, but are now located in the 3D momentum space. When cutting a  $k_x$ - $k_y$  plane of the Brillouin zone, as for example photoemission experiments would do, the surface states won't connect the full range between the Weyl points anymore, but will be cut off at the point, where they cross the measured  $k_x$ - $k_y$  plane - leaving a note-like shape [40].

Similar behaviour can be found in Dirac semimetals, which can be treated as overlap of both Weyl points seen in Fig. 1.19c. This results in opposite tilted surface states for each spin, as seen in Fig. 1.19d.

The chiral anomaly is a cause for a set of interesting features, among which are the negative magnetoresistance, special local and nonlocal transport phenomena or chiral optical activity of Weyl semimetals.

## 1.5 Recent advances in topological materials

Over the recent years, a growing number of materials hosting topological states has been experimentally realized and many more are proposed to be hosts to topological phases of matter. In the following chapters, a short overview about major examples for all three types of materials in this thesis will be given: topological insulators, Dirac semimetals and their special cases, the Weyl semimetals.

During the last years, research focus in the field of topological materials shifted. With the number of materials hosting topological states rapidly growing over the last years, they also got more complex. It has been found, that topological states are present in many usually nontopological materials due to external influences like strain or chemical doping. In addition to that, the newest materials of this zoo are showing topological states in combination or alongside with superconductivity - a field where the number

of new found compounds is still growing.

### 1.5.1 Topological insulators

Graphene was one of the first topological materials. The discovery immediately sparked interest, quickly resulting in many more materials in which topological phases manifest in specific points in the 3D momentum space. Nowadays, also the group of single layer \*-ene materials has grown substantially. Silicene and germanene are among the most important to be noted. Current research focusses on functionalizing these sheets to enhance their properties. Possible use cases are within the nanoelectric spintronic devices, like a possible topological field-effect transistors [41, 42].

Soon after its prediction in 2007 [25], the first experimentally realized topological insulator was  $\text{Bi}_{1-x}\text{Sb}_x$  [43], quickly followed by the realization of symmetry protected states in pure Sb [44, 45]. In 2009, a second generation of topological insulators was realized, including  $\text{Bi}_2\text{Se}_3$  [46–50] as the most prominent example, but also  $\text{Bi}_2\text{Te}_3$  [45, 47, 49, 51] and  $\text{Sb}_2\text{Te}_3$  [45].

Due to incorporated defects in some materials a natural doping is occurring, shifting the Fermi level either up into the conduction band in  $\text{Bi}_2\text{Se}_3$  where the Fermi level is in the middle of the band gap, or down, in the case of  $\text{Sb}_2\text{Te}_3$  which is doped in a way, that the top of the valence band is located right at the Fermi level and the topological states are found above.

### 1.5.2 Dirac semimetals

The first experimentally observed 3D Dirac semimetal was  $\text{Cd}_3\text{As}_2$  [52–54], showing two 3D Dirac cones per Brillouin zone. More materials experimentally confirmed to be Dirac semimetals include  $\text{Na}_3\text{Bi}$  [55, 56],  $\text{BiO}_2$  [57],  $\text{ZrTe}_5$  [29] and  $\text{BaZnBi}_2$  [58].

Since the experimental realization of Dirac semimetals, several experiments have been carried out, to study the transition of topological insulators to Dirac semimetals and vice versa, by varying pressure, strain or doping of the crystals. The two compounds  $\text{SrSn}_2\text{As}_2$  [59] and  $\text{ZrTe}_5$  [60, 61], in comparison to other Dirac semimetals, are existing naturally close to the transition point between topological insulators and Dirac

semimetals.

Recent materials include PtBi<sub>2</sub>. First believed to be a trivial material, it was later found that the cubic phase hosts Dirac fermions [62] and also the hexagonal phase was confirmed to be topological [63] now. It has been suggested, that this material might also host triply degenerate Fermions [64].

### 1.5.3 Weyl semimetals

TaAs was the first material where Weyl surface features have been proven experimentally in 2015 [65–67]. It was shown, that the material hosts 24 Weyl points and the Fermi surface only consists of Fermi arcs. Closely after TaAs replacements of tantalum and arsen were discussed, resulting in NbAs, NbP and TaP being proposed to be type-1 Weyl semimetals [68]. Shortly after, photoemission experiments confirmed these calculations [69–71].

The class of type-2 Weyl semimetals was proposed with the example of WTe<sub>2</sub> [36] and soon after confirmed [72] experimentally. The true nature of the surface states in this compound, whether they are originating from topology or not, is still a matter of discussion and has not yet been fully resolved [73]. MoTe<sub>2</sub>, shown by [74–78], as well as the alloy Mo<sub>1-x</sub>W<sub>x</sub>Te<sub>2</sub> [79, 80] were also proven to be type-2 Weyl semimetals.

As shown in Fig. 1.17 the Weyl nodes can not only be separated in momentum space, but also by energy. This is the case for YbMnBi<sub>2</sub> [81]. Additionally, this material does exhibit magnetic properties, in contrast to the previously mentioned materials.

In combination with the chiral anomaly, magnetic materials would allow complete new possibilities in technology. This shifted research towards materials with intrinsic magnetic properties, like Heusler and semi-Heusler compounds. The most promising semi-Heusler compositions are GdPtBi, NdPtBi [82], Co<sub>2</sub>TiX (X = Si, Ge, Sn) [83, 84] or HfIrX (X = As, Sb, Bi) [85]. Compositions like XCo<sub>2</sub>Z (X = V, Zr, Nb, Hf; Z = Si, Ge, Sn) [86] are Heusler compounds possibly showing Weyl states.

## 1.6 Future applications of topological matter

After discussing the topological properties as well as an overview of the current state of materials, the current state of applications of topological matter will now be discussed in some more details. Three major areas are currently of interest: Spintronics, topological quantum computation and thermoelectricity.

### Spintronics

Major use cases of topological matter are researched in the field of spintronics [87, 88] or chiral electronics [89]. These fields of electronics focus on utilizing the intrinsic features of materials, like a spin current or chiral anomaly to strongly enhance the properties of current state of the art electronic devices.

Spintronics are believed to be the next step in electronics [90], combining intrinsic spin features together with well known electronic concepts. It is hoped, that this would allow a great extension of Moore's law. Current research, for example, focusses on non-volatile memory devices, transistors with switching times down by orders of magnitude and less current loss within the chips. A recent example is the realization of current induced switching of the magnetization by spin-orbit torque at room temperature in  $\text{Bi}_2\text{Se}_3/\text{NiFe}$  heterostructures, boosting the non-volatile memory applications based on topological insulators [91].

### Thermoelectricity

Thermoelectric applications have long been of great interest: they would allow the harvesting of waste heat in many processes, increasing their overall efficiency, better heat imaging, locally manageable cooling or even solid state coolers. Yet, the materials available were not ideal. While research focussed a long time on quantum sized effects in semiconductors [92], the first realizations of topological materials gave a large boost, resulting in something which can be called a renaissance of thermoelectric applications [93]. Through utilizing the unconventional behaviours of the topological materials in the Seebeck [94] and moreover the Nernst effect new regions of efficiency and enhanced material properties could be achieved [95].

Among all the mentioned application possibilities, the thermoelectric generators - turning a heat flux into electric energy, as well as thermoelectric coolers - basically working exactly in the contrary to the generators are of especial interest. Examples of recent progress include a greatly increased operating temperature range for thermoelectric generators [96], increased performance for thermoelectric microcoolers [97] or the evaluation of new materials for thermoelectric generators [98].

### **Topological quantum computation**

While spintronics can be viewed as an upgrade to already existing electronics, quantum computing requires different approaches. Until now, no small sized quantum computer could be realized. Among the many different approaches to quantum computing, topological quantum computing is one of the promising ones [99].

Topological quantum computers are aiming at the usage of non-Abelian states of matter to manipulate and store the quantum information. This happens in a non-local way, protecting the quantum information from noise and decoherence - the two major complications in quantum computing [99–102].

Systems are non-abelian, if their ground state is separated from the excited states by an energy gap and all particles in a system interact in a way, that they form a quasiparticle called a "non-Abelian" anyon. If these states are present, the ground state is degenerate, and the grade of the degeneracy depends on the number of anyons present. Additionally, these states are robust against local perturbations, as they are not originating from a symmetry.

There are different ways of achieving this state through topology. The easiest are Majorana fermions [103], whereas the chaining of superconductors and topological states is also believed to exhibit anyons.



## 2 Experimental Details

To prove the existence of topological states, multiple methods can be used. In this chapter, the photoemission spectroscopy will be presented and discussed based on reference [104]. Additionally, experimental details will be presented, both for general photoemission setups as well as for measuring topological states as done in this thesis.

### 2.1 Angle-resolved photoemission spectroscopy - ARPES

Photoemission spectroscopy, in short PES, is a collection of experimental methods all based on the photoelectric effect, first observed by Hertz [105] and later explained by Einstein [106]. Among the experimental methods are ultraviolet photoelectron spectroscopy (UPS), X-ray photoelectron spectroscopy (XPS) and angle-resolved photoelectron spectroscopy (ARPES). All of these methods can be used to analyse the electronic structure of solids.

The photoelectric effect describes the absorption of the energy of an incident photon by a sample. The absorbed energy excites an electron in the sample into higher states and ultimately into vacuum. In this case the electrons move through the sample and cross the surface into vacuum with a kinetic energy of

$$E_{kin} = h\nu - \Phi \tag{2.1}$$

Where  $\nu$  is the photon energy and  $\Phi$  is the work function of the material, usually equal to 4–5 eV.

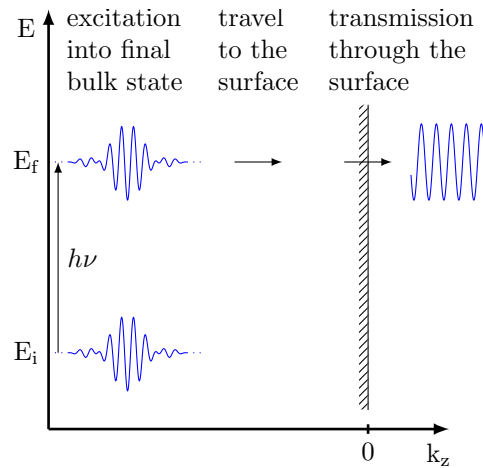


Figure 2.1: Three step model of the electron excitation during a photoemission experiment. Picture derived from [104].

### The three step model

The complex process after the absorption of the photon can be broken down into a simplified three step model. This model, as shown in Fig. 2.1, splits the overall complex process into three simple steps:

1. After the absorption of a photon, the electron is excited from the initial state  $E_i$  to the final bulk eigenstate  $E_f$ . The transition probability between the two states is a very important parameter of this step.
2. Being in the final bulk state, the electrons travel towards the sample surface. This process is influenced by the scattering probability and the average mean free path of the electron during its travel to the surface.
3. The electron leaves the sample. To successfully cross the surface, the electron has to overcome the work function of the material. The work function describes an electric field originating from the surface of the sample resulting in a barrier, which the electron has to overcome.

The total photoelectron current is thus a product of three terms: the total probability of the optical excitation, the scattering probability of the electrons as well as the transmission probability through the surface barrier.

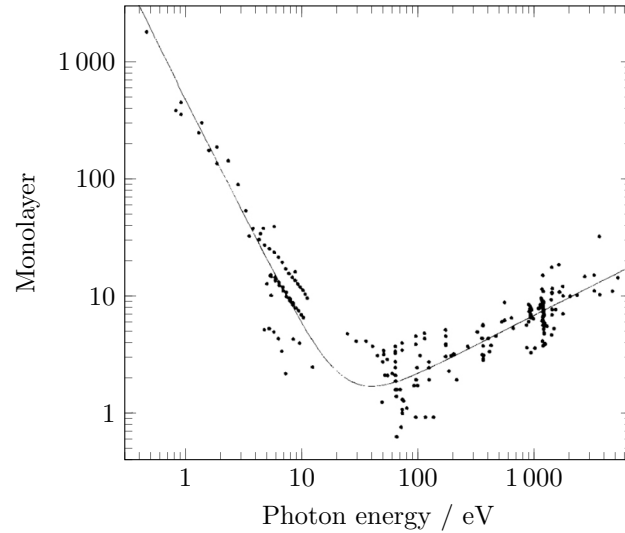


Figure 2.2: Correspondence between the energy of the incident photon and the penetration depth of the photons, noted in monolayers. Panel taken from reference [107].

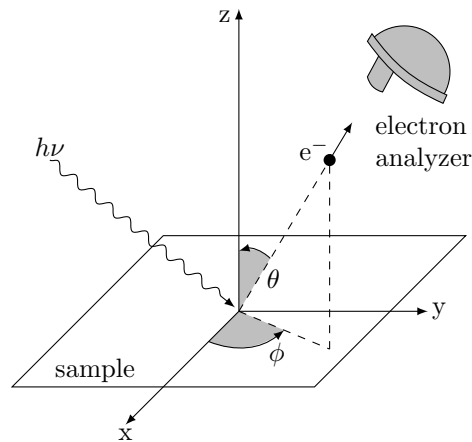


Figure 2.3: The angular geometry of an ARPES setup. Picture derived from [104].

In reference [107] the correspondence between the incident photon energy and the resulting penetration depth is discussed. Fig. 2.2 shows exemplarily the correspondence between the incident photon energy and the number of monolayers, which can be excited by the photons. This analysis shows, that ARPES itself is not only surface sensitive, but also that the choice of the light source can play a crucial role.

### The angular geometry of ARPES

When measuring the electrons from the sample by a detector, their kinetic energy is measured for a given emission direction. Their vector can be expressed as:

$$\mathbf{K} = \mathbf{p}/\hbar \quad (2.2)$$

The modulus of this term is given by  $K = \sqrt{2mE_{kin}}/\hbar$ , and the components parallel to the surface ( $K_x, K_y$ ) are determined by the polar emission angle  $\theta$  and the component perpendicular to the surface ( $K_z$ ) through the azimuthal emission angle  $\phi$ . The components can thus be written as:

$$K_x = \frac{1}{\hbar} \sqrt{2mE_{kin}} \sin \theta \cos \phi \quad (2.3)$$

$$K_y = \frac{1}{\hbar} \sqrt{2mE_{kin}} \sin \theta \sin \phi \quad (2.4)$$

$$K_z = \frac{1}{\hbar} \sqrt{2mE_{kin}} \cos \theta \quad (2.5)$$

To get the relation of  $E_{kin}$  and  $\mathbf{K}$  measured with the detector and the electronic dispersion relation  $E(\mathbf{k})$ , a look at the total energy and momentum conservation laws is needed. The total energy relation is given by:

$$E_{kin} = h\nu - \Phi - |E_B| \quad (2.6)$$

with  $h\nu$  being the photon energy,  $\Phi$  being the work function of the sample and  $E_B$  the binding energy. In regards of momentum conservation, the components parallel to the surface are conserved due to a translational symmetry, but the abrupt change of the potential along the  $z$ -axis causes this to not be true in the case of the perpendicular axis. The parallel components can be written as:

$$\mathbf{k}_{\parallel} = \frac{1}{\hbar} \sqrt{2mE_{kin}} \cdot \sin \theta \quad (2.7)$$

To obtain the perpendicular component of the crystal momentum, a priori assumptions have to be made, either through band structure calculations or by adopting a nearly-free-electron description for the final Bloch states, as described in [104]. Out of these assumptions, one gets

$$\mathbf{k}_{\perp} = \frac{1}{\hbar} \sqrt{2m(E_{kin} \cos^2 \theta + V_0)} \quad (2.8)$$

$$V_0 = |E_0| + \Phi \quad (2.9)$$

$E_{kin}$  is the kinetic energy of the electron in reference to the vacuum level and  $V_0$  is the inner potential - the energy of the bottom valence band in regards to the vacuum level. From equation 2.7 it can be read, that the x and y momentum space components only depend on the tilting angle and the photon energy. Thus, when changing the angle for a constant energy, it directly translates into a change in the measured location within the 3D Brillouin zone. This is not the case for the axis perpendicular to the surface. As it can be seen from equation 2.9, the inner potential  $V_0$  appears as an additional parameter, thus the  $k_z$  value can not be directly translated from the photon energy. If this relation is needed, there are three possibilities to measure this as discussed by [104]. i: Optimization between calculation and measured band structure in regards of the occupied band structure. ii: Setting  $V_0$  to the theoretical zero of the muffin tin potential in the calculation. iii: Measure the electronic structure at the Fermi level through the full energy range and calculate  $V_0$  out of the observed periodicity. This method is usually the simplest, as it is just a normal measurement with varying photon energies.

### Spectral function

It will now be discussed, what is actually measured during a photoemission experiment. The electrons within the solid are located in bands throughout the Brillouin zone. Neglecting any interactions, this would be directly measured by ARPES. In real samples, the electrons interact in multiple ways: electron-electron interactions, electron-phonon interactions to name two examples. These interactions can change the dispersion substantially. The intensity of a 2D single-band system as measured by ARPES can be written as:

$$\mathbf{I}(\mathbf{k}, \omega) = \mathbf{I}_0(\mathbf{k}, \omega, \mathcal{A})f(\omega)\mathcal{A}(\mathbf{k}, \omega) \quad (2.10)$$

where  $\mathbf{k} = \mathbf{k}_{\parallel}$  is the in-plane electron momentum,  $\omega$  is the energy of the electron in reference to the Fermi level.  $\mathbf{I}_0$  is a matrix element which depends on the incident photon energy and polarization and  $f(\omega)$  is the Fermi function. The spectral function  $\mathcal{A}(\mathbf{k}, \omega)$  is given by:

$$\mathcal{A}(\mathbf{k}, \omega) = -\frac{1}{\pi} \frac{\sum''(\mathbf{k}, \omega)}{[\omega - \epsilon_0(\mathbf{k}) - \sum'(\mathbf{k}, \omega)]^2 + [\sum''(\mathbf{k}, \omega)]^2} \quad (2.11)$$

where  $\Sigma'(\mathbf{k}, \omega)$  is the energy renormalisation,  $\Sigma''(\mathbf{k}, \omega)$  is the lifetime broadening and  $\epsilon_0$  is the dispersion of the bare band.

### 2.1.1 ARPES and semimetals

Proving the large number of predicted topological materials turns out to be a difficult task. Methods like ARPES, quantum oscillations utilizing de-Haas-van-Alphen or Shubnikov-de-Haas effects, magneto-optical transport measurements and STM have been of large interest when determining the existence of topological states in solid matter. The possibility to directly depict the band structure of materials has made ARPES one of the most important tools of this list.

#### Using ARPES to verify theory predictions

Theory predictions are very convenient: it is possible to calculate all possible kinds of chemical compounds and predict their electronic properties. When discussing band structures, calculations allow to dissect the band structure into bulk and surface contributions as well as trivial and topological ones. Due to the ability to directly resolve the band structure in the 3D Brillouin zone, ARPES is an ideal method to verify theoretical band structure calculations.

All materials in this thesis were initially predicted by calculations. We used ARPES measurements to confirm these predictions and propose necessary changes where the prediction differed from the actual measured material. Overall, two steps were taken for each material. First, the confirmation of the bulk calculations and general material properties like Brillouin zone symmetries. This is done by mapping the electronic structure of material at several photon energies. These results were relayed to the theoreticians to adjust calculation parameters if needed. After clarifying the bulk features, the now available calculations were greatly aiding the search of the topological states. Whilst for the topological insulators the observation is usually a bit easier and more a matter of the system resolution, direct measurement of the topological states in type-2 Weyl semimetals can be challenging due to many overlapping bulk and topological states close to the Fermi level.

### Difference between surface and bulk states

Especially in topological insulators it is obvious, that apart from the 3D Bulk features, there are surface features existing close to the Fermi level. These states do have a very limited  $k_z$  dispersion. Thus, alternating the photon energy will change the bulk features while the topological states stay at the same position.

This case is similar for semimetals. Similar to the topological insulators, the topological states in semimetals are considered

In terms of an ARPES experiment this means, that features likely to be topological, can be checked by tuning the photon energy to cover different high symmetry points on the  $k_z$  axis of the Brillouin zone. Topological features are still visible, whereas the bulk features are changing - providing a confirmation of the existence of topological features within the band structure.

### ARPES and quantum oscillation measurements

ARPES data can be compared to and expanded by a wide range of different other experimental methods, like Hall measurements, neutron diffraction and many more.

Within this thesis, ARPES will be compared to quantum oscillation measurements, like the de-Haas-van-Alphen or Shubnikov-de-Haas methods. Quantum oscillations allow the mapping of the Fermi surface feature sizes by measuring the frequency of electrons on the Fermi surface. These electrons are forced into circular motions by a magnetic field and due to their energy constraints are moving only on contours of their respective Fermi surface features. Their results can be compared to ARPES Fermi surface maps by utilizing the Onsager relation[108]:

$$F = \frac{\Phi_0}{2\pi^2} A_k \quad (2.12)$$

where  $\Phi_0$  is the flux quantum ( $\Phi_0 = 2.07 \times 10^{-15} \text{ T m}^2$ ) and  $A_k$  is the cross sectional area of the Fermi surface, being the size of the measured features of the ARPES Fermi surface map.

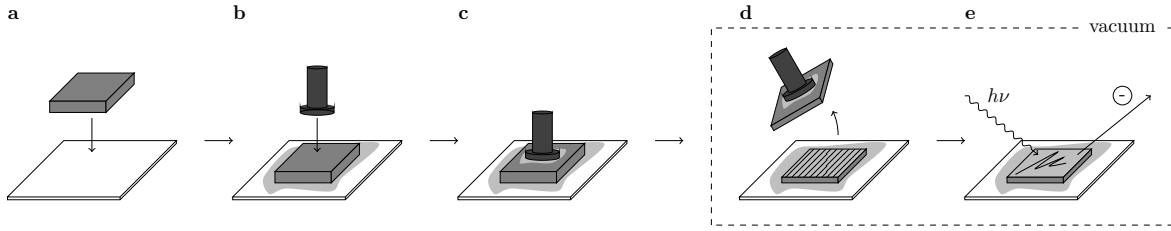


Figure 2.4: Sample preparation steps. a) The crystal is glued to the sample holder, b) a top post is glued onto the sample, c) the whole stack is cured and put into vacuum. d) The sample is cleaved by breaking off the top post, resulting in a clean surface of the sample, e) the sample is measured by ARPES.

## 2.2 Sample preparation considerations

Due to its surface sensitivity, ARPES requires atomically clean planar surfaces. Fig. 2.4 shows the simplified steps of the single crystal preparation for an ARPES experiment as done with all samples measured and presented in this thesis.

First, the sample is glued to the sample holder and a so-called top-post is fixed to it. This stack is then typically heated for one hour to 150 °C to cure the used two-component epoxy. Specific samples might require special epoxy glue, which itself requires different curing times. The heating also degases the epoxy to increase its performance within ultra-high vacuum. Additional steps have to be done, if the sample is either air sensitive or can not be exposed to warmer temperatures. This has not been the case for the samples presented later in this thesis.

After curing the stack, it is put into the vacuum chamber and pumped down to ultra high vacuum, usually below  $5 \times 10^{-10}$  mbar. In the measurement position, the top-post will be removed, breaking parts of the crystal away with it - ideally resulting in a mirror-like surface on the remaining crystal. This surface can now be measured using ARPES, but has a limited lifetime. This lifetime depends on a set of experimental parameters, including the used photon source, overall vacuum quality and what type of atoms/molecules are diluted in the vacuum like remnants of evaporation processes.



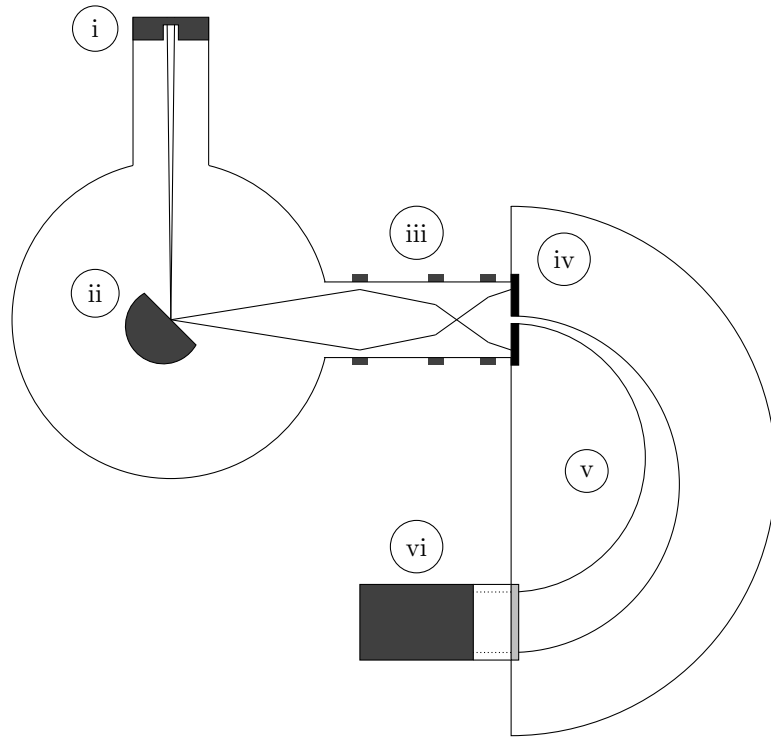


Figure 2.5: Experimental ARPES setup with a schematic beam path sketched into the picture. i: The light source and optics. ii: The sample on a manipulator with a cryostat in a high vacuum chamber. iii: The electron optics of the analyser, separating the angles. iv: Entrance slit of the analyser. v: Hemispherical part of the analyser, separating the energies. vi: A channel plate inside the hemisphere is filmed by an external attached CCD camera to visualize the results.

## 2.3 Experimental setups

Manifold ARPES setups have been used to measure the data presented in this thesis. Fig. 2.5 shows a simplified schematic of an ARPES setup. The sample is mounted on a cryo-manipulator in ultra-high vacuum, usually being cooled to liquid helium temperatures. Each setup does have a light source together with optics to focus photons on the sample. Light sources are usually synchrotrons, noble gas discharge lamps or lasers. Advantages and disadvantages of the different light sources will be discussed later. Electrons from the sample are collected by an electron analyser, where they are first separated by angle through electron lenses. In the hemispherical part of the

analyser the electrons are split by energy. After their separation by energy and angle, the electrons are directed onto a microchannel plate which is filmed by a CCD camera. This setup is therefore measuring a energy-momentum “cut”, of the four dimensions of data: three momentum axes and the binding energy scale. The momentum axis measured in this setup is parallel to the surface of the sample, which exactly is depending on the exact orientation of the entrance slit within the overall setup. To measure along the other axis parallel to the surface, the angle between the sample surface and the beam is changed by rotating the manipulator. The manipulator itself can be used to align the sample within the beam as well as the analyser focus, to achieve the highest possible count rates.

Typically, ARPES setups are also equipped with additional vacuum chambers. These allow for sample storage in vacuum, sample treatment like heating, surface treatments like sputtering or dosing with alkali metals or simply act as a second vacuum chamber for optimised sample transfer and storage.

### **2.3.1 The resolution of ARPES**

As the measurement of fligree topological features is complex, several parameters can be tuned for optimal resolution. The factors affecting the resolution in ARPES will now be discussed in more detail. First to mention are the resolutions of the experimental equipment. The finite resolution of the electron analyser limits the angular resolution to  $0.20^\circ$  and the energy resolution to 3 meV. The finite resolution of the motors on the manipulator, limiting the resolution of sample positioning, can usually be neglected as their influence on the final result is way smaller than the ones from the analyser.

Resolution further depends on the sample quality and the quality of incident light beam. A bad surface reduces the signal-to-noise ratio by significant amounts and multiple crystallites might lead to overlapping and offset features in the measured picture. The light source itself plays an important role: the light can be focussed and the beam shape can be altered using blades within the beam path. Focussed beams usually cope better with smaller samples or smaller good parts on the sample surface. While these aspects are usually given for synchrotron light, this is not always the case for laboratory light sources. The flux of the beam is important to consider in regards of

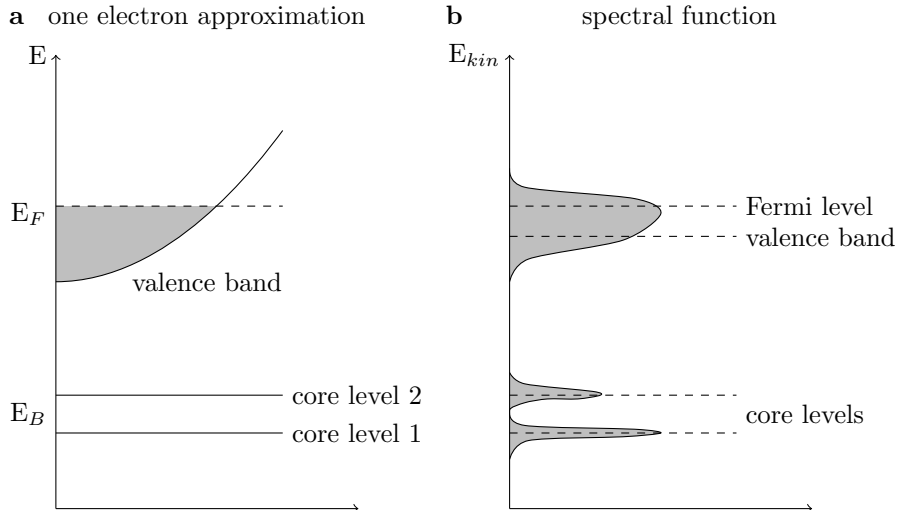


Figure 2.6: Comparison of band structure a) as they are in solids and b) how a corresponding ARPES image would resolve them.  $\Phi$  is showing the work function of the material, showing the difference between the Fermi level and the vacuum energy.

signal-to-noise ratio. A higher flux allows shorter measuring times, making the actual measurement less dependent on other difficulties like surface degradation due to dirt on the surface or a damaging of the surface stemming from too intense light.

The temperature of the sample strongly influences the sharpness of the Fermi edge. The higher the temperature of the sample is, the broader and less pronounced the measured features are, as the electrons scatter more often along their path to the sample surface due to the reduced mean free path. In all experiments done, the lowest temperatures possible for each setup have been chosen to reduce this influence. The exact temperature ranges are shown in Tab. 2.1. Lowering the temperature of a material strongly reduces the vibrations of the atoms within the material, resulting in less scattering of electrons. Less scattering is visible as a higher signal-to-noise ratio in the measured spectrum.

Fig. 2.6 shows a comparison of a one electron approximation to the previously discussed spectral function. The additional effects covered by the spectral function are influencing the overall shape of the band structure. These effects include many body effects, lifetimes or scattering. As discussed before, ARPES measures this spectral function and the influence of many parameters can be optimized for ideal results during the

Name	Light source	Energy [eV]	Detector	Temp. [K]
1 <sup>3</sup> ARPES	Synchr. (BESSY II) [109]	15 - 100	Scienta R4000	1
1 <sup>2</sup> ARPES	Synchr. (BESSY II) [110]	15 - 100	Scienta R8000	35
I05	Synchr. (Diamond) [111]	15 - 180	Scienta R8000	7
BL-9B	Synchr. (HSRC) [112, 113]	15 - 100	ESPRESSO	15 - 50
USARPES	Laser	5.6 - 6	Scienta DA30	3.5
UPS	He-Lamp	21.2	Scienta R8000	30

Table 2.1: ARPES setups used to measure the results presented in this thesis. For each station, the available light source with the used energy range, the detector and the temperature range used for measurement is given.

experiment, like increasing the mean free path of the electrons during their transition to the sample surface or improving of the sample surface through ideal cleaving conditions.

### 2.3.2 End stations

Tab 2.1 shows the list of used ARPES end stations for all results presented in this thesis. For each station the used light source along with the used photon energy range is given as well as the used detector. Additionally, the lowest temperature reachable with these setups is noted.

It has to be noted, that the setup, as shown in Fig. 2.5, is altered slightly for the experiments performed at the Hiroshima synchrotron facility (see table 2.1). On this setup a VLEED spin detector was positioned after the hemispherical ARPES detector, allowing the simultaneous measurement of ARPES spectra and 3D spin polarization [112, 113].

### 2.3.3 Light sources

The characteristics of the incident light greatly influence an ARPES experiment. In the following, the three major light sources: synchrotrons, gas discharge lamps and lasers are discussed. Newer styles of ARPES experiments, for example enabled by the use of pulsed laser light, will be discussed at the end of this section.

### Synchrotron radiation

Synchrotron radiation is a very convenient light source for all types of experiments. In terms of ARPES, the very high photon flux and the seamlessly tunable photon energy are the most important. Photon energies can be adjusted typically from approximately 15 eV to several hundred electronvolt through a monochromator. A tunable photon energy allows for easy  $k_z$  dependency mapping. Each beamline does offer optics to adjust the shape and focus of the beam allowing very small spot sizes. The spot sizes are reasonably small and can usually be adjusted in at least width or height. With these setups, it is possible to measure smaller samples with higher signal-to-noise ratio, as well as samples, which are difficult to cleave. Despite all the advantages of synchrotron light, the very limited availability of beamtime can be considered as a disadvantage.

### Noble gas lamps

Using helium or xenon discharge lamps, ARPES experiments can be carried out outside of synchrotrons. While allowing for more flexibility compared to synchrotrons in terms of available beamtimes, these light sources are limited in several ways. First, these lamps have fixed wavelengths: for helium lamps mostly the He-I $\alpha$  (21.2 eV) and He-II $\alpha$  (40.8 eV) are being used. Second, photons of these lamps are not focussed. Whilst the overall flux can be comparable to a synchrotron, the non-focussed photon beam results in a lower brilliance of the light source, requiring larger sample surfaces and longer measuring times during the experiment. The longer exposition times uncover another technical problem of this type of light source: the noble gasses used are not 100% pure. Small amounts of other gasses are diluted with them, with molecular hydrogen being one of the most common contaminant. In the discharge process, these molecules get split up into atomic hydrogen and through the setup of these lamps the gas gets into close reach of the sample surface. There it diffuses into the surface therefore destroying it, as described in the work of Nicolay et al [114]. Due to this, sample lifetime in lab setups using gas discharge lamps is very limited, if no additional technical precautions have been carried out. For our experiments, a filter for hydrogen molecules was put into the helium source of the discharge lamp, to decrease the amount of available hydrogen which would decrease sample lifetime.

### Laser radiation

In the recent years, lasers became more common light sources used for ARPES measurements with lower photon energies. Through these low photon energies it is possible to measure more detailed pictures of topological states, especially when surrounded by many other bands. Typical photon energies range from 5.9 eV to 7 eV, but different laser configurations allow different energies, going up to 22 eV [115]. Typical measurement limits from lasers with photon energies up to 7 eV are about  $\sim 2$  eV on the energy scale and  $\sim 0.5 \text{ \AA}^{-1}$  on the momentum scale.

But not only the strongly increased resolution is a welcome benefit. When pumping the sample with another laser beam first, it is possible to measure the band structure above the Fermi level without the need to chemically alter the sample surface. This method is called pump-probe ARPES. Using ultrafast pulsed lasers, it is also possible to measure changes to band structure as a function of time. This is called time-resolved ARPES or tr-ARPES.

In general, lasers, despite showing just a very small portion of the Brillouin zone due to the low energy, have some advantages when comparing to noble gas discharge lamps: the photon flux is much higher, the beam can be focussed through simple optical elements and no gas enters the chamber which might degrade the sample surface, greatly increasing sample lifetime during measurement.

**Pump-probe ARPES** utilizes two laser beams: a first one, a pumping beam, excites the electrons of the sample into the unoccupied states. A second beam then measures those excited states. There are certain requirements to these beams: their timing is crucial, as the measurement of the excited states must happen while the electrons are still in the unoccupied region. For this, a usual setup would utilize a 800 nm/1.55 eV pump beam in conjunction with a 200 nm/6.2 eV measurement beam.

**Time-resolved ARPES** utilizes ultrashort laser pulses at very high repetition rates. This mode can be viewed as stroboscopic light flashes, producing still images of the current state of the electronic configuration of the system. This allows the measurement of movement speeds of charge carriers or the analysis of interactions of the crystal solids

under the effect of moving charge carriers on the time scale.

Current work still focusses on unifying most of the advantages of the different laser based-systems into all-in-one setups: high photon energies, high repetition rates while maintaining a high photon flux [115]. Photon energies of up to 22 eV would increase the overall measurement ranges to  $\sim 5$  eV on the energy and  $\sim 1.5 \text{ \AA}^{-1}$  on the momentum scale.





# 3 TaIrTe<sub>4</sub> - a ternary type-2 Weyl semimetal

## 3.1 Theory predictions

With the introduction of WTe<sub>2</sub> and MoTe<sub>2</sub> as type-2 Weyl semimetals [36], the search for more type-2 semimetals quickly started. TaIrTe<sub>4</sub> was proposed as first ternary and third overall type-2 Weyl semimetal [116].

The material shares some similarities to the first two materials: the basic structure of the unit cell is similar, with just one axis being doubled. The crystals are of a non-centrosymmetric orthorhombic structure of space group 31 (Pmn2<sub>1</sub>) [117]. The lattice parameters were measured as  $a = 3.77 \text{ \AA}$ ,  $b = 12.421 \text{ \AA}$ ,  $c = 13.184 \text{ \AA}$ . Looking

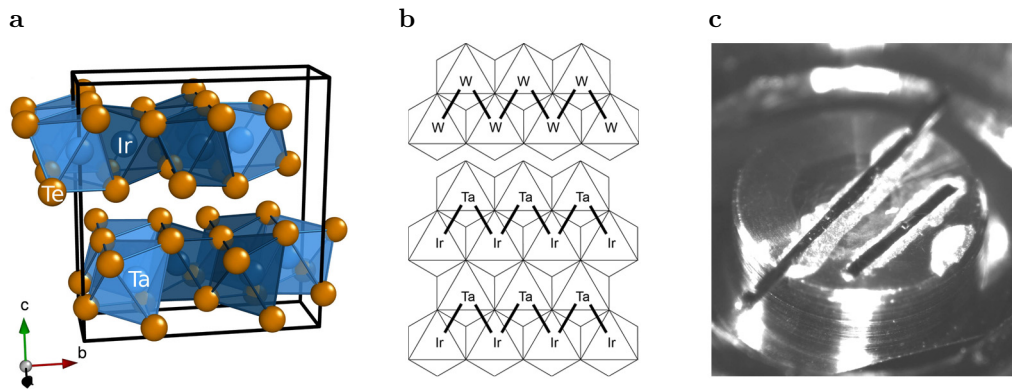


Figure 3.1: a) Atomic structure of TaIrTe<sub>4</sub>, showing the layered structure of the material. b) comparison of the schematic structure of one layer of WTe<sub>2</sub> (top) and TaIrTe<sub>4</sub> (bottom). The atoms within these layers are bound covalent, whereas the layers are connected by Van-der-Waals bonds. c) Picture of the needle shaped TaIrTe<sub>4</sub> crystals glued to a sample holder.

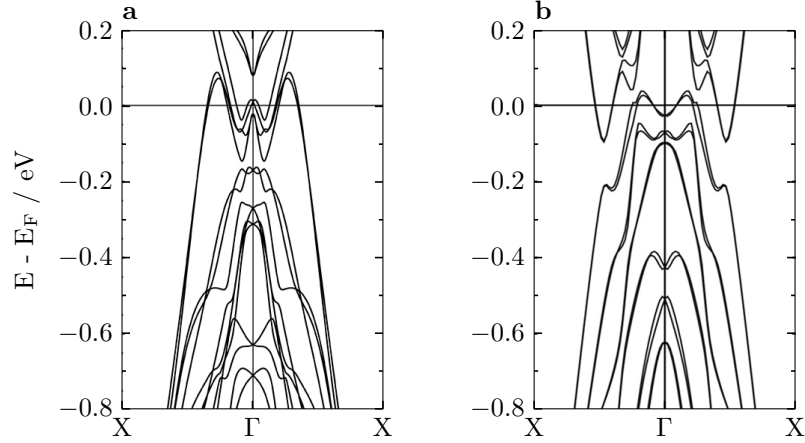


Figure 3.2: a) Fully relativistic band structure calculation for  $\text{TaIrTe}_4$  along the X- $\Gamma$ -X direction. b) Same for  $\text{WTe}_2$ .

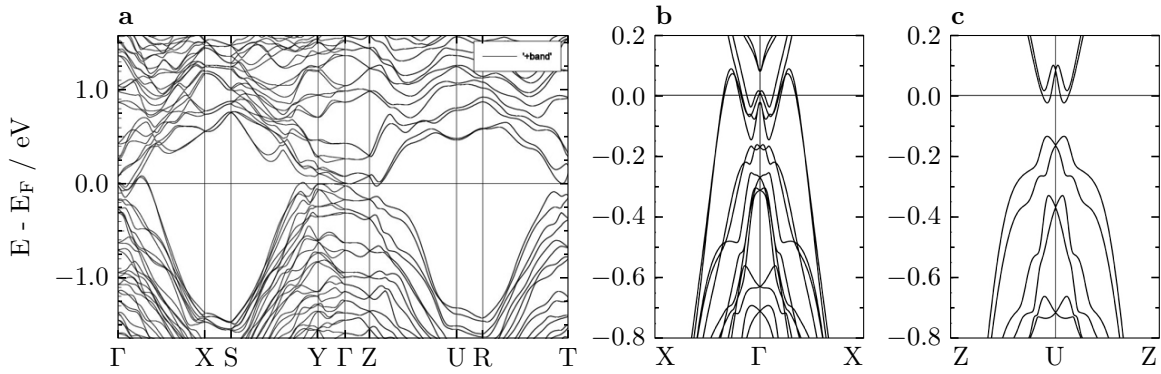


Figure 3.3: a) Fully relativistic band structure calculation for  $\text{TaIrTe}_4$ . Panel b) and c) show the X- $\Gamma$ -X / Z-U-Z parts with more detail.

into Fig. 3.1a, it is nicely seen that a unit cell consists of 2 layers of octahedra, being slightly distorted and sharing their corners.

Despite all the similarities in the atomic structure of the systems, the similarities should not be overemphasized, as the electronic properties turn out to differ - especially the Fermi surface. Looking at the band structure shown in Fig. 3.2, it is immediately visible, that the hole and electron character of the features at the Fermi level are interchanged when comparing to the  $\text{Mo}_x\text{W}_{1-x}\text{Te}_2$  system.

A full range calculation of the band structure of  $\text{TaIrTe}_4$  is shown in Fig. 3.3. It is clearly visible, that the most interesting aspects of the band structure are around the  $\Gamma$  point. Also seen are larger changes for the topmost valence bands: these are either

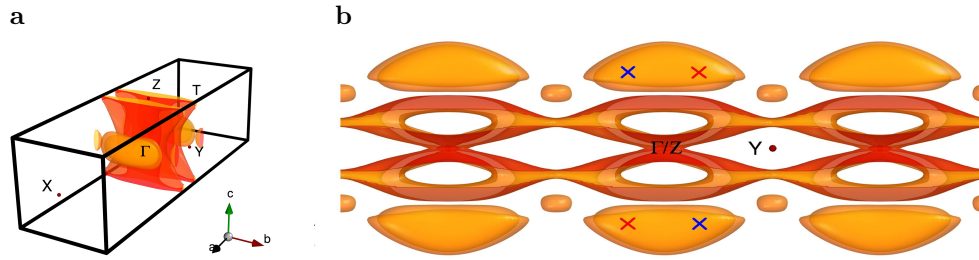


Figure 3.4: a) 3D calculated Fermi surface. b) Top view of a), corresponding to the a-b-plane. Pictures taken from [118].

close to the Fermi level or approximately  $-1.5$  eV away from the Fermi level. Panels b and c highlight the most interesting parts of this band structure. Fig. 3.3b is the X- $\Gamma$ -X direction showing an area where the conduction bands cross the Fermi level directly at the  $\Gamma$  point, whilst the valence bands also cross the Fermi level slightly towards the X-point. As is seen in panel 3.3c, the valence bands are shifted down compared to panel 3.3b in  $k_z$  direction, while the conduction bands still cross the Fermi level.

This behaviour of the valence and conduction bands at the Fermi level is discussed in more detail in Fig. 3.4. This figure shows the calculated Fermi surface, consisting of five pockets: two electron pockets in the centre of the Brillouin zone, two nested hole pockets aligned next to the electron pockets. In comparison to the electron pockets, the hole pockets to have a strong 3D character. Additionally, there is a small hole pocket at the y-axis boundary of the Brillouin zone at Y points.

Due to the same symmetry conditions as they are in  $\text{Mo}_x\text{W}_{1-x}\text{Te}_2$ , the Weyl points can only appear at the  $k_z = 0$  plane. Without turning on spin-orbit coupling,  $\text{TaIrTe}_4$  does also have eight Weyl points. Taking spin-orbit coupling into account, this number reduces to four.

The calculations of  $\text{TaIrTe}_4$  were done using LDA [119] with FPLO code [120]. Brillouin zone was sampled with a  $12 \times 6 \times 6$  k-mesh and integrated using the tetrahedron method. Calculations were done with and without taking spin-orbit coupling into account. During the calculations, a model for  $\text{TaIrTe}_4$  was established to describe the bands up to 1 eV above the Fermi surface accurately. For this, the Wannier functions for Ta-5d, Ir-5d and Te-5d bands were used. This model allows quick and correct

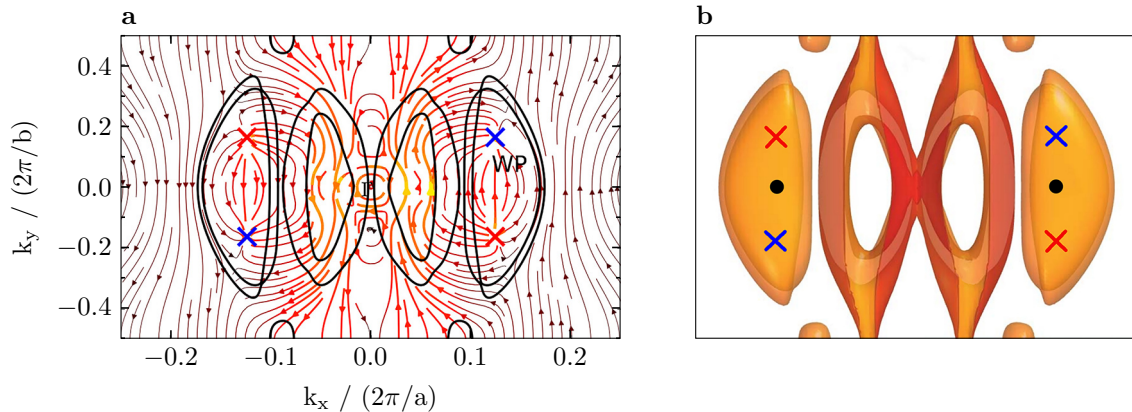


Figure 3.5: a) Calculated Berry curvature in the Brillouin zone in the  $k_x$ - $k_y$  plane at  $k_z = 0$ . The Weyl points are drawn as crosses, with red and blue being the opposite chirality. b) Calculated Fermi surface including the calculated position of the Weyl points. Panel a) taken from [116].

calculations for the interesting parts of the Brillouin zone, but might lead to slight differences in other, non optimised areas, in comparison to full calculations for the respective areas.

The topology of the material was predicted and calculated by first calculating the Berry curvature in the Brillouin zone. The results of this are shown in Fig. 3.5a). Shown is the averaged Berry curvature of the  $k_x$ - $k_y$  plane. This was achieved by calculating the Berry curvatures for the  $N$  lowest bands over the whole Brillouin zone and then integrating over their whole  $k_z$  range. Sinks and sources do have the values 1 and  $-1$  and are shown as red and blue crosses. With these calculations the existence of the Weyl points has been clearly proven, as well as the exact position could clearly be revealed. Fig. 3.5b) depicts again the Fermi surface calculations, this time highlighting the location of the Weyl points. Overall, the points with same chirality are located diagonally.

Fig. 3.6 shows the surface states from the experimental point of view. While doing these calculations, the finite  $k_z$  integration of ARPES, as described in Sec. 2.1, was taken into account. Here the different cleavage planes of the crystal start to play a crucial role, as the topology of both surfaces should give a closed loop state throughout the Brillouin zone. Panels 3.6a and 3.6c highlight energy momentum spectra clearly

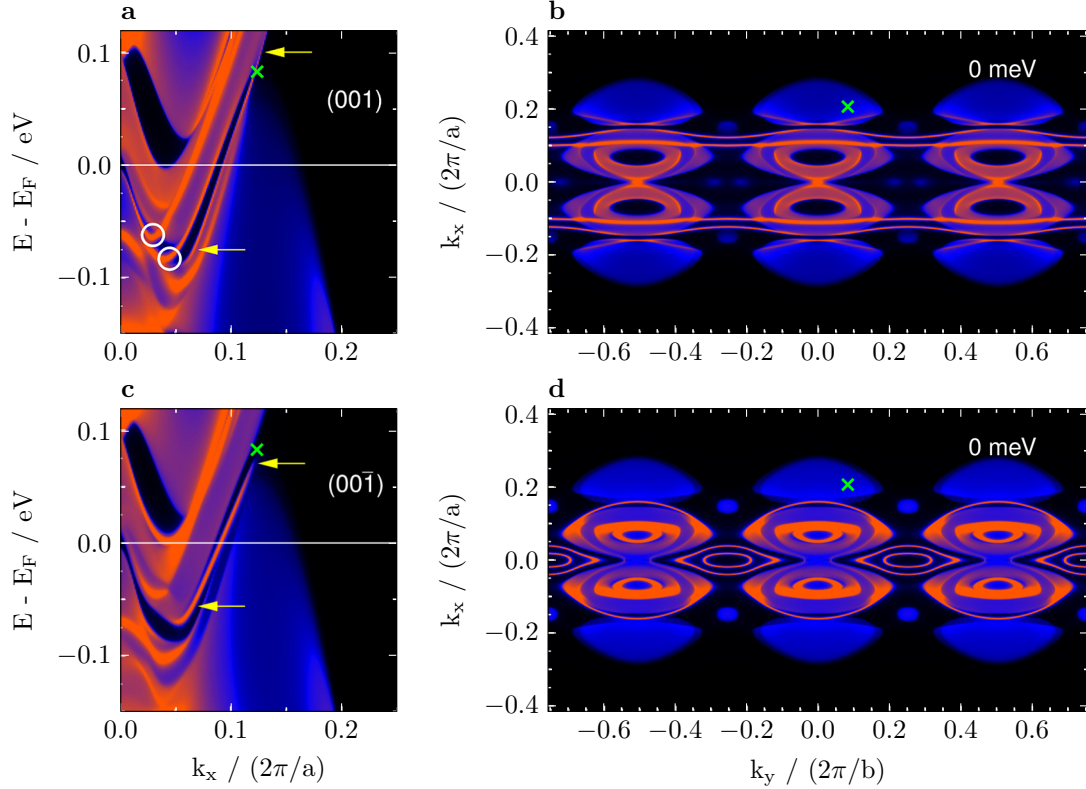


Figure 3.6: a) Calculated energy-momentum-data and b) calculated Fermi surface ARPES spectra for cleavage plane (001). c), d) same as a & b for the (00 $\bar{1}$ ) plane. The topological states in the energy momentum cuts are highlighted with arrows and the location of the Weyl points are marked with crosses. Pictures taken from [116].

showing the topological state emerging from the lower part of the central conduction bands, going along them to the top of the valence bands, where the Weyl points are located. Their exact location is expected to be 82.7 meV above the Fermi level.

The topological surface Fermi-surface states are especially interesting in this compound. They are connecting the Weyl points along the edge of the large hole pockets and their length is up to one third of the Brillouin zone, thus being way larger compared, for example, to the  $\text{Mo}_x\text{W}_{1-x}\text{Te}_2$  system. Also, they are roughly going in parallel at least for the (001) surface. This, together with the long arcs, again highlights the speciality of this material. As noted in Sec. 1.5, materials like TaAs do have proven topological states and Fermi surfaces mostly consisting only of Fermi arcs, but their arrangement is very complex - making them hard to analyse in terms of electronic structure or

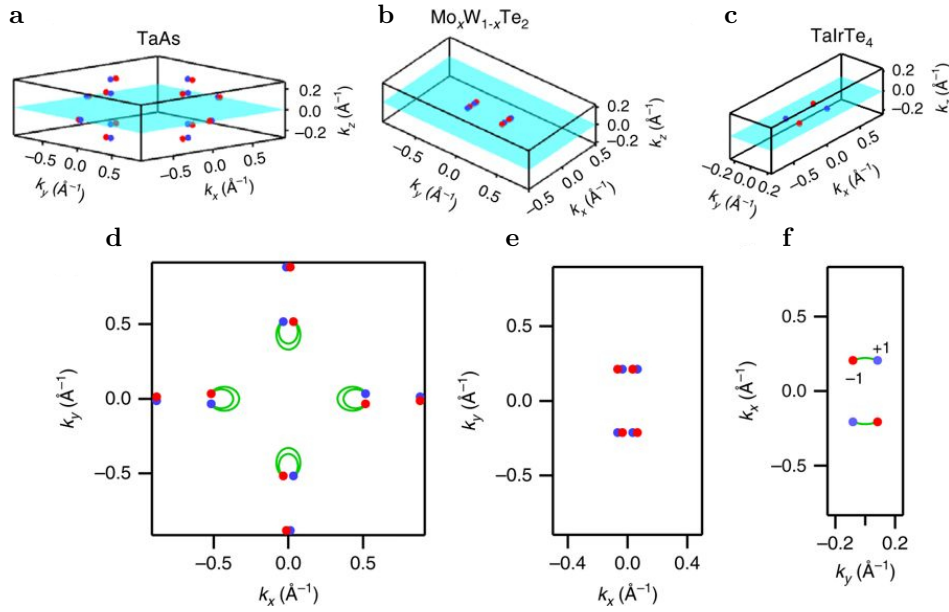


Figure 3.7: Weyl point and Fermi arc configuration in the 3D Brillouin zone (top row) and on the  $k_x$ - $k_y$  plane (bottom row) for a), d) TaAs; b), e)  $\text{Mo}_x\text{W}_{1-x}\text{Te}_2$  and c), f)  $\text{TaIrTe}_4$ . Picture taken from Ref. [121].

transport properties, as they can not be separated well from the bulk features. It is also noteworthy, that the Fermi arcs are present on both of the inequivalent surfaces. Fig. 3.7 highlights the simplicity of  $\text{TaIrTe}_4$  again. TaAs, the first experimentally confirmed type-1 Weyl semimetal, has a very complex configuration of Weyl nodes: 24 of them are distributed along the Brillouin zone in close distance pairs. Eight pairs are stacked in  $k_z$  direction. The Fermi arcs, connecting the Weyl points of each pair, are of a hemicircle shape.  $\text{Mo}_x\text{W}_{1-x}\text{Te}_2$ , the first proposed type-2 Weyl semimetal, only has eight Weyl points. Again, these are distributed in pairs and all Weyl points are very close to each other. Fermi arcs are very short, connecting the Weyl points within each pair.

In contrast to these materials, with their complex configurations,  $\text{TaIrTe}_4$ , shown in panel 3.7c, is very simplistic. Only four Weyl points, the minimum in non-centrosymmetric materials, are present and well separated within the Brillouin zone. All of the Weyl points are in the same  $k_z$  plane and are connected by very long, nearly parallel Fermi arcs.

These features make this material especially interesting for future research concentrat-

ing on leveraging these topological properties and understanding them as well as their influence on the whole electronic system of these materials in every detail.

## 3.2 Crystal growth

Single crystals of  $\text{TaIrTe}_4$  have been grown from an excess Te flux. The pure elements were put into an evacuated quartz tube on an aluminium crucible in a ratio of Ta:Ir:Te of 1 : 1 : 20. After sealing, the tube was heated to 1000 °C and afterwards slowly cooled down to 700 °C. At that temperature the excess Te was centrifuged away.

The crystals are of a needle like shape, roughly of the size of  $2.0 \times 0.5 \times 0.02$  mm. Initial characterization of the crystals was done using single-crystal x-ray diffraction. Full scans over a full sphere of the reciprocal space have been done in  $0.5^\circ$  steps as well as  $2\theta$  ranges from  $4^\circ$  to  $60^\circ$ . The results were corrected from absorption effects and refined using a set of different software (SAINT [122], SHELXL [123], JANA2006 [124]).

These measurements resulted in a crystal lattice with  $a=3.78 \text{ \AA}$ ,  $b=12.43 \text{ \AA}$  and  $c=13.19 \text{ \AA}$ , being of the  $\text{Pmn}2_1$  space group same as  $\text{WTe}_2$ . As already mentioned, in comparison to  $\text{WTe}_2$ , the lattice constant in b direction is doubled.

## 3.3 Transport measurements

Prior to a detailed ARPES analysis, a set of transport measurements were conducted. These were performed by S. Khim and presented in [117]. As Weyl semimetals, but especially the ones of type-2, do have unique electronic transport and magnetic properties, these measurements are a good starting point for checking the presence of the exotic states. In this part, the magneto-resistance, Hall resistivity and quantum oscillations will be highlighted. Each type of measurement was done with three different crystals of the same batch.

### 3.3.1 Magneto-resistance

The magneto-resistance was measured along all axes of the Brillouin zone. Fig. 3.8a shows the relative magneto-resistance  $\rho/\rho_0$  in dependence of the strength of the mag-

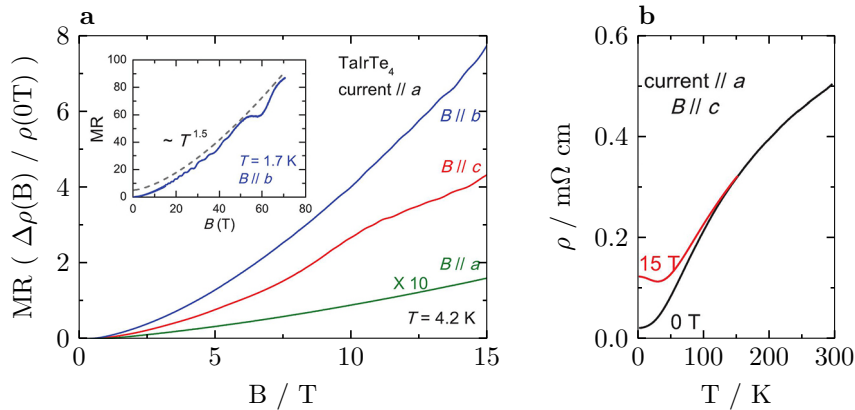


Figure 3.8: a) Relative magneto-resistance of TaIrTe<sub>4</sub> for different orientations of the magnetic field to the crystal in function of the the magnetic field. The angular dependence of the signal is clearly visible. b) Magneto-resistance as function of the temperature for 0 T and 15 T. An increase of the magneto-resistance is observed for low temperatures. Figures taken from [117].

netic field. The shown data was recorded with the magnetic field parallel to the respective crystal axes. Clearly visible is, that the external magnetic field oriented parallel to axis a has the lowest, while the external magnetic field parallel to b the highest values, highlighting the expected high anisotropy of the magnetic resistivity in regards of the angle of the external magnetic field. The inset shows the curve with the magnetic field parallel to axis b in dependence of the magnetic field recorded at a sample temperature of 1.5 K. Quantum oscillations are visible at these temperatures and magnetic fields. Fig. 3.8b shows the magneto-resistance in dependency of the temperature for two selected magnetic fields. The magneto-resistance measured parallel to axis c shows a strongly increased resistivity. When comparing the resistivity at low temperatures for both curves, a clear qualitative change below 100 K is visible between 0 T and 15 T. The slope of the magnetic resistivity rises with  $\rho \propto B^{1.5}$  up to a value of 70 T without saturation, just like WTe<sub>2</sub>.

### 3.3.2 Hall effect

Magnetic field and temperature dependent Hall effect has been measured and is depicted in Fig. 3.9. Shown is the magnetic resistivity as a function of the magnetic field



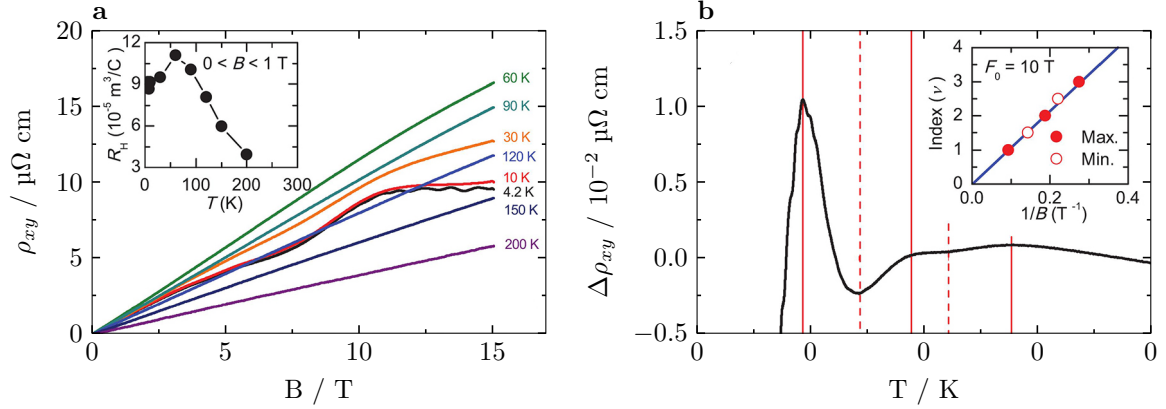


Figure 3.9: a) Magnetoresistance in dependency of the magnetic field shown for several different low temperatures. Starting with 30 K and below, quantum oscillation become visible. The inset highlights the data in dependency of the temperature in the range of 0 T to 1 T for the magnetic field. b) Maxima and minima of the curvature. Picture taken from [117].

for a list of different temperatures ranging from 4.2 K to 200 K. The positive  $\rho_{xy}$  seen for every temperature in the range indicates dominating hole carriers in the material.

The inset in panel a shows the Hall resistivity in dependence of the temperature shown for magnetic field between 0 T and 1 T. A maximum at approximately 60 K can be observed for the Hall resistivity. This strong dependence on the temperature is an indication for bands with coexisting electron and/or hole pockets, which is fitting to the calculated band structures. In a more general way, a temperature dependent Hall resistivity can be caused by multiple bands having their own distinct temperature dependencies of their respective carrier mobilities.

For temperatures of 30 K and below, oscillations can be observed in Fig. 3.9a. Fig. 3.9b depicts the derivative of the 4.2 K curve plotted as  $\Delta\rho_{xx}$  over  $1/B$ . Maxima and minima are visible and highlighted with solid (maxima) and dashed (minima) lines. The inset shows the positions of the calculated periodicity of the minima and maxima as function of  $1/B$ . A good correspondence can be observed. The large peak in panel b corresponds to the change in curvature at  $\approx 10 \text{ T}$ , seen in panel a as well as in the magneto-resistance plots in Fig. 3.8a.

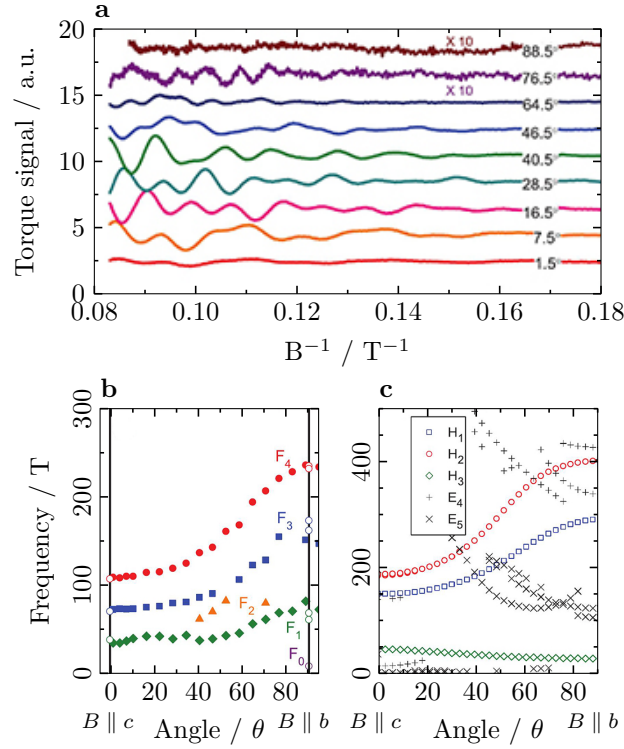


Figure 3.10: a) Oscillating torque signals in dependency of  $1/B$  measured for various angles at a fixed temperature of 15 K. The polynomial background has been subtracted. b) De-Haas-van-Alphen frequencies in dependence of the measured angle. c) Calculated angular dependency of the de-Haas-van-Alphen data. Picture taken from [117].

### 3.3.3 Quantum oscillations

As the data showed Shubnikov-de-Haas oscillations above 10 T, a more detailed investigation was performed to further analyse the angular dependent magnetic quantum oscillations.

For this, magnetic torque de Haas van Alphen signals have been recorded for 1.5 K at various angles. The crystal and the fields were aligned in a way, that  $\theta = 0^\circ$  is along the b axis, whereas  $\theta = 90^\circ$  is along the c axis. When looking at the signal, with curves from different angles plotted over  $1/B$ , as seen in Fig. 3.10a, a clear difference for the curves in dependence of the angle can be seen. This is a very good evidence for anisotropic 3D Fermi surface pockets. The corresponding frequency spectra of these curves are shown in panel b. Panel 3.10c additionally shows calculated de-Haas-van-Alphen spectra.

Comparing panels 3.10b and 3.10c, the measured features  $F_3$  and  $F_4$  are corresponding to the calculated spectra of the two large hole pockets  $H_1$  and  $H_2$  respectively. The measured curve of  $F_1$  was identified to belong to the small hole pockets via ARPES and the calculations can not properly reproduce this curvature. Feature  $F_0$  is believed to belong to the electron pockets and calculated features  $E_4$  as well as  $E_5$ .

Overall, the features of the pockets  $H_1$ ,  $H_2$  and  $H_3$  were qualitatively comparable, although discrepancies are in the calculations regarding the exact curvature and the absolute values.

## 3.4 ARPES measurements

After the discussion of the theoretical predictions, the measured ARPES data will now be discussed on the following pages. This data will be discussed in comparison to the theoretical predictions and, where applicable, will be compared to transport data available.

The ARPES data will also be discussed and analysed in detail to prove the existence of topological states within this material, as they are predicted by theory.

### 3.4.1 Fermi surface and band structure

Figure 3.11a shows an ARPES energy-momentum cut taken at 100 eV. The energy is ranging from the Fermi level at 0 eV to  $-12$  eV. Panel 3.11b shows the corresponding DFT calculations in a corresponding range - showing more than one Brillouin zone on the  $\Gamma$ -X- $\Gamma$ -X- $\Gamma$  path - slightly more than seen in the measured ARPES plot. Whilst this range is not interesting for topological aspects of the material, it allows a very good comparison with band structure calculations to eliminate uncertainties in the bulk band structure calculation. Comparing both panels, a very good correspondence is seen. The qualitative agreement of the calculations and measurement is very good: the topmost band, going from  $\approx -1.5$  eV at X-point up to the Fermi level and crossing it when going to  $\Gamma$ -point. For the range of  $-2$  eV to  $-7$  eV, not many features can be compared due to the resolution of the cut, but the large gap between  $-7$  eV and  $-11$  eV is again reproduced by calculations very precisely.

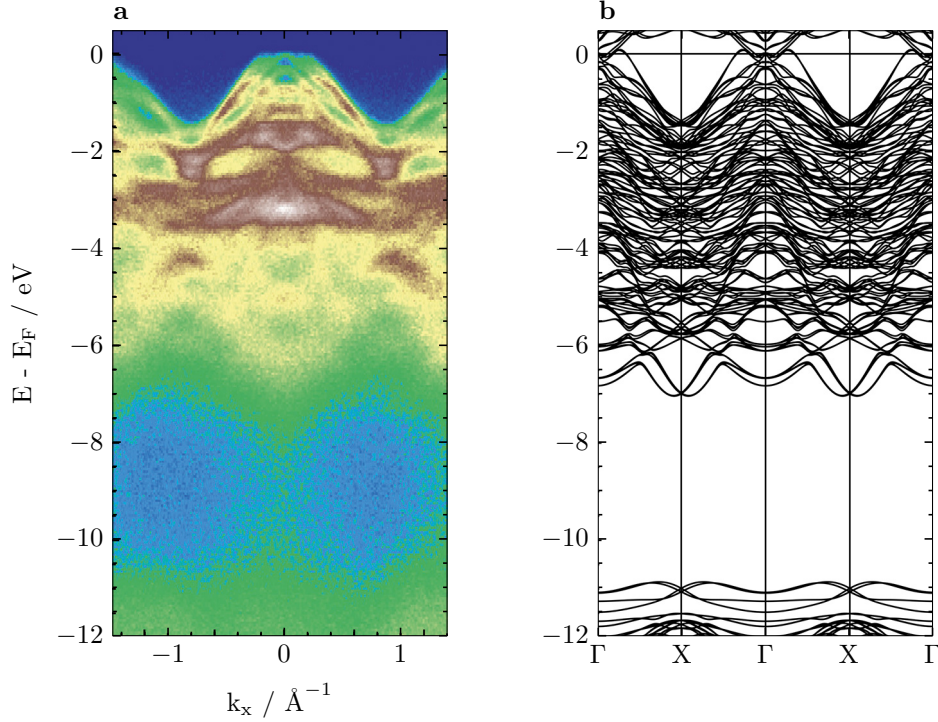


Figure 3.11: a) Measured energy-momentum cut at 100 eV photon energy and a wide energy range below the Fermi energy. b) Corresponding calculated band structure of the same region. Picture taken from [118].

Fig 3.12 is presenting a set of Fermi surface maps taken at a set of different photon energies: 100 eV, 70 eV and 25 eV, shown in panels a-c respectively. On the 100 eV map, the Brillouin zone of the material can be observed completely. On the  $k_x$  axis, being the long axis, the bands from the second Brillouin zone on this axis are seen at  $1.1 \text{\AA}^{-1}$ . On the  $k_y$  axis many repetitions of the features are visible. Noteworthy is, that the central Brillouin zone at  $(0, 0) \text{\AA}^{-1}$  is the least intense one, while the third one on this axis is the most intense one. The same behaviour is observed in panel b, which resolves the overall structure better, due to the lower photon energy of 70 eV. When using a photon energy of 25 eV, the features are resolved the best.

Panel d depicts a  $k_z$  scan of  $\text{TaIrTe}_4$  from  $k_z = 2.0 \text{\AA}^{-1}$  to  $5.5 \text{\AA}^{-1}$ . This range corresponds to a photon energy range of 18 eV to 100 eV. In Fig. 3.4, theorists predicted a “continuous” central electron pocket - which is seen as a continuous stripe of intensity in the center. The hole pockets are seen at  $2.5 \text{\AA}^{-1}$  and  $4.5 \text{\AA}^{-1}$  and do show a clear dependency of the  $k_z$  value. There should be another set of pockets at approximately

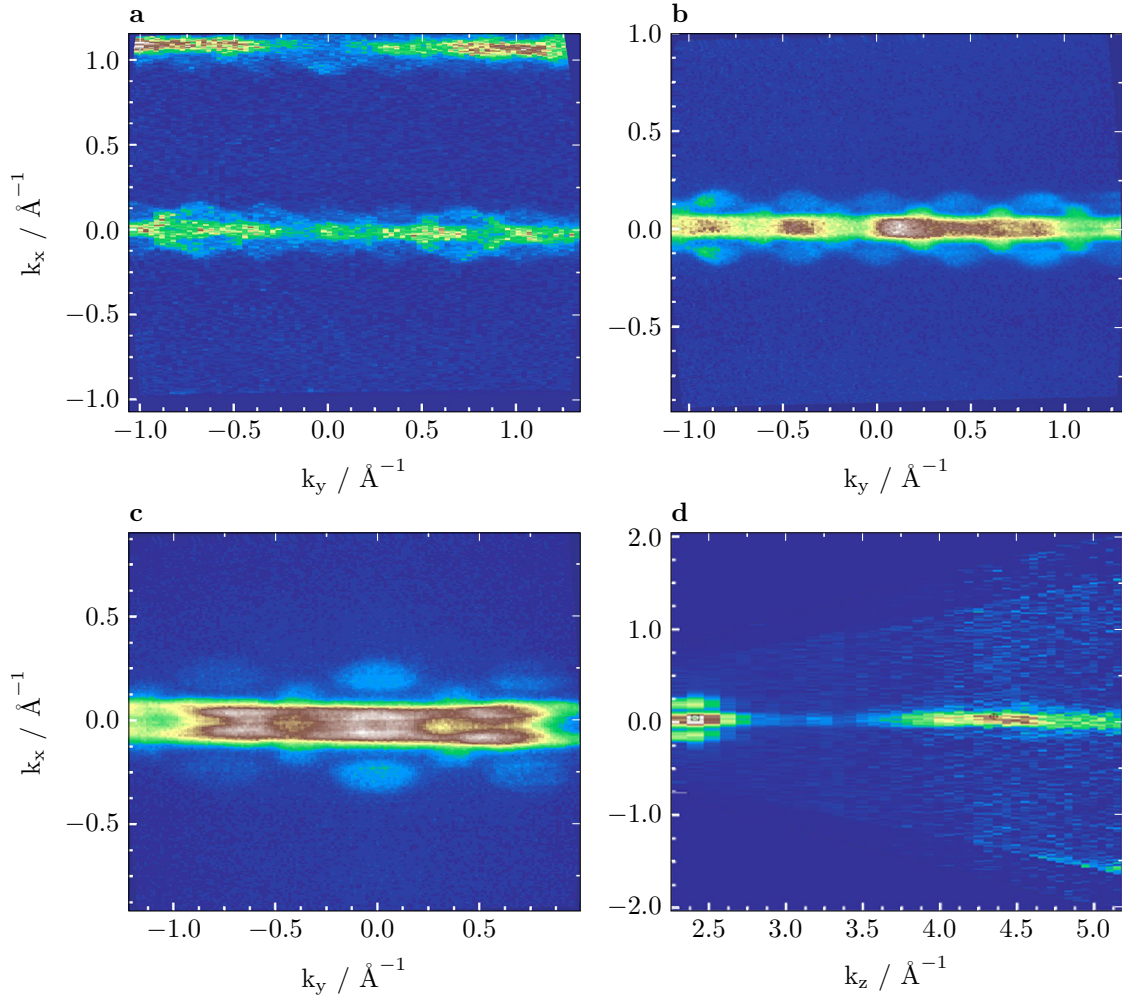


Figure 3.12: ARPES Fermi surface maps, taken at a) 100eV, b) 75eV, c) 25eV. d) ARPES energy dependence scan of an energy-momentum cut through the  $\Gamma$  point in the range from 18 eV to 100 eV shown as  $k_z$  map. Picture taken from [118].

$3.5 \text{ \AA}^{-1}$ , but due to the matrix element the intensity is very low at this range. This also corresponds well to the distribution of the intensity of the electron features.

Whilst the 100 eV map is to a certain extent an initial overview of the electronic structure of the system, the 25 eV photon energy was taken from the  $k_z$  plot, corresponding to the position of the  $\Gamma$  point at the centre of the hole pockets.

In Fig. 3.13 the 25 eV Fermi surface map cutting the Brillouin zone at the  $\Gamma$  point is compared in more detail with the calculated ARPES spectra. Comparing the overall arrangement of the pockets on the Fermi level, the predicted Fermi surface is very good.

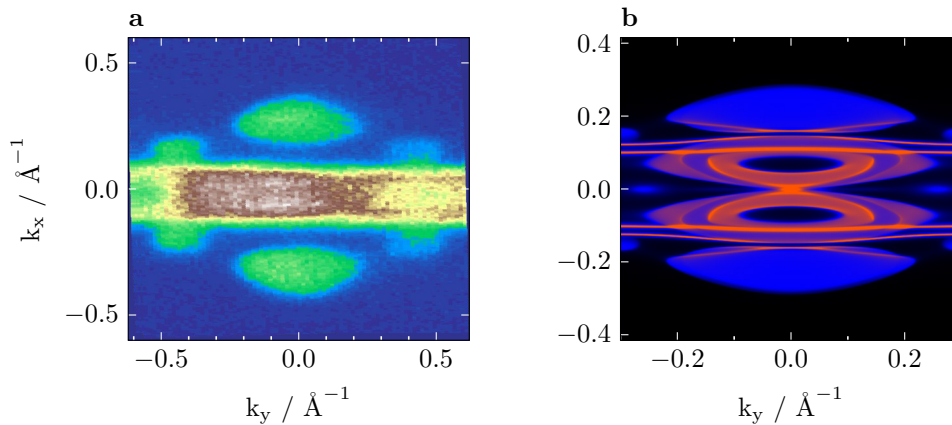


Figure 3.13: a) Measured Fermi surface, taken at 25 eV photon energy. b) Calculated Fermi surface of the same momentum space region.

Shape and position of the hole pockets are fitting well as well as the continuous electron features. The gap between the large hole pockets and electron pockets is larger in the measurement and the size of the smaller hole pockets is smaller in the calculation. For detailed discussions in regards to the electron features the resolution is not good enough, but still a difference in intensity is seen as calculated when comparing the  $\Gamma$  point at the centre with the Y point at the side of the Brillouin zone.

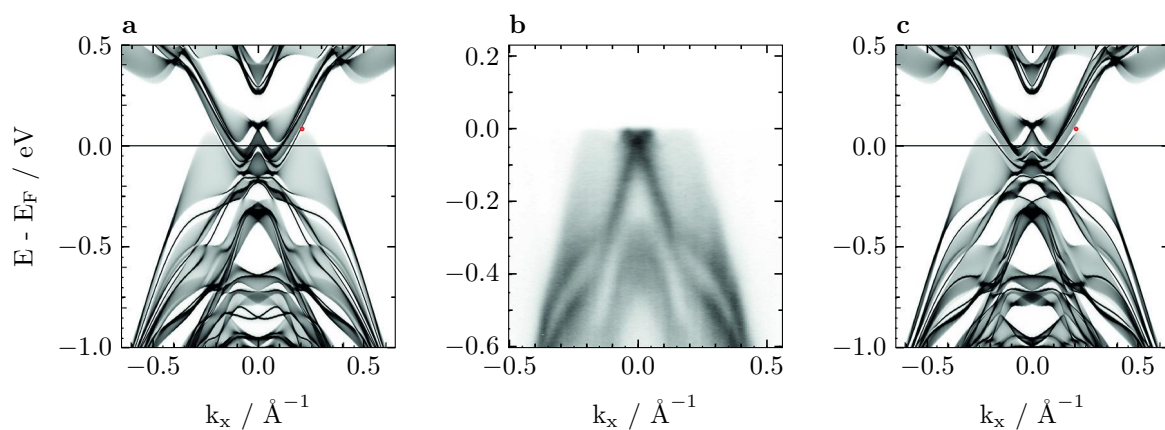


Figure 3.14: a) Calculated energy-momentum cut for the (001) surface termination. b) Measured energy momentum cut at 100 eV photon energy, c) as a for the  $(00\bar{1})$  surface termination. Picture taken from [118].

### 3.4.2 Cleavage plane

As written in section 3.1, TaIrTe<sub>4</sub> cleaves along the  $c$  axis where the layers are loosely connected by Van-der-Waals bonds. When looking at these layers in detail, the top of a layer, the  $(001)$ -surface, and the bottom of the layer, the  $(00\bar{1})$ -surface, do have different surface terminations. As already shown, these terminations do have a distinctive difference in their electronic structure. Fig. 3.14 shows calculated energy-momentum cuts in panels 3.14a and 3.14c for each surface. The major differences are fine details of dispersions along the inner edges of the hole pockets at the Fermi level. Other changes can be found in the energy region of  $-0.6\text{ eV}$  to  $-0.8\text{ eV}$ , but are not of interest in regards of the surface features. A corresponding measured energy-momentum cut is shown in panel b. The overall correspondence is very good: features like the shoulders visible at  $-0.4\text{ eV}$  are a good example as well as the measured momentum width of the features at the Fermi level corresponds well to the preliminary calculations. When focussing on the surface features - or, in general, on the small range around the Fermi energy - it can not be said, whether the  $(001)$  or the  $(00\bar{1})$  surface is fitting better. Thus, using energy-momentum cuts is not a feasible way of determining the cleaved surfaces.

Whilst the cleaved plane could not be determined from this comparison, it became apparent, that the calculated Fermi level and the measured Fermi level are not in perfect agreement. Because of this, a slight shift of approximately  $25\text{ meV}$  is proposed - moving the Weyl point from  $82.7\text{ meV}$  to approximately  $50\text{ meV}$  above the Fermi level.

As it is not possible to determine the measured plane by energy-momentum cuts, Fermi surface maps, presented in Fig. 3.15 were looked at next, as these show larger differences between the different surface terminations. The panels 3.15b and 3.15c show the expected Fermi surfaces for both cleavage planes. Major differences are visible at the electron features. These are continuous for the  $(001)$  surface, on the  $(00\bar{1})$  surface these features are interrupted, with high intensity areas around the  $\Gamma$  point and smaller features at the  $Y$  point. Fig. 3.15e and 3.15f show the same surfaces as 3.15b and 3.15c, but at an energy  $-75\text{ meV}$  below the Fermi energy. These different shifts do take the differences of the Fermi level into account for comparison. At this lower energy, the

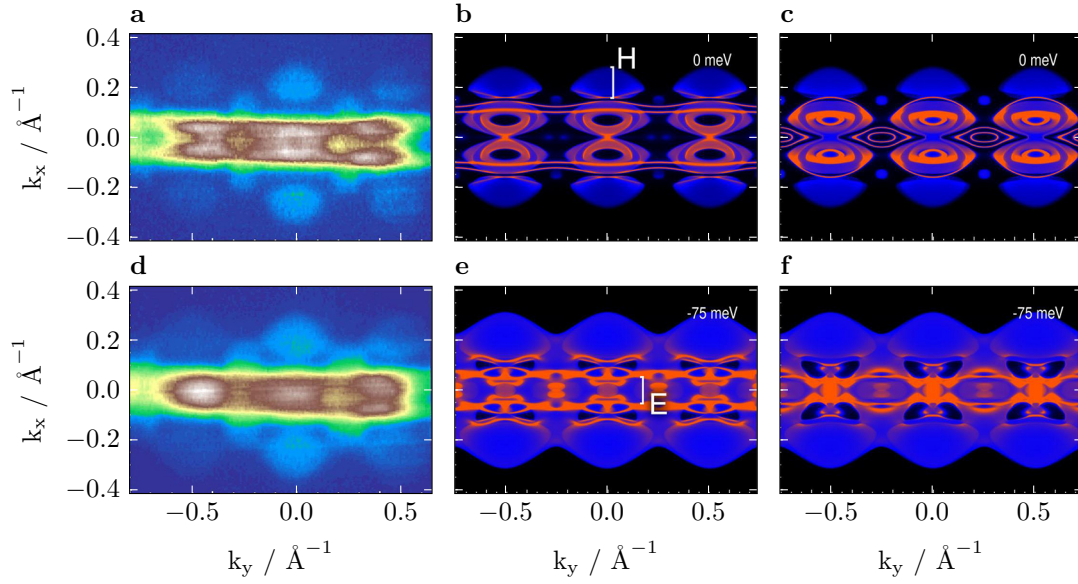


Figure 3.15: Analysis of the different possible cleavage planes. a) 25 eV photon energy Fermi surface map. b) Calculated (001) Fermi surface and c) calculated (00 $\bar{1}$ ) surface. d) Same map as shown in a), but shown for a shifted energy of  $E - E_{\text{Fermi}} = -25$  meV. e) and f) same as b) and c), but with an energy offset of  $-75$  meV. Picture taken from [118].

hole pockets get larger and connect, forming a continuous feature. Smaller spots with no intensity are still visible at the positions of the edges of the large hole pockets. This behaviour is seen for both surface terminations.

Fig. 3.15a and 3.15d show the measured Fermi surface map at the measured Fermi level and 25 meV below the Fermi energy respectively. Comparing these to the calculated maps seen in panels 3.15b, c and 3.15e, f beside them show very good correspondence with the (001) surface shown in panels 3.15b and 3.15e. Panels 3.15c and 3.15f have good correspondence for the hole pockets, but the electron features are quite different: the measured intensity is mostly a continuous linear shape, with areas of lower intensities within the linear shape. This fits well to the calculations for the (001) surface, but there is no correspondence to the (00 $\bar{1}$ ) surface.

In panel 3.15b the width of the hole pocket is marked with “H”. Panel 3.15e marks the width of the electron features with an “E”. Fig. 3.16 shows ARPES energy momentum cuts taken exactly at the marked positions in the  $k_x$ - $k_y$  plane. On top of the spectra, momentum distribution curves taken at the Fermi level are shown. In these curves,



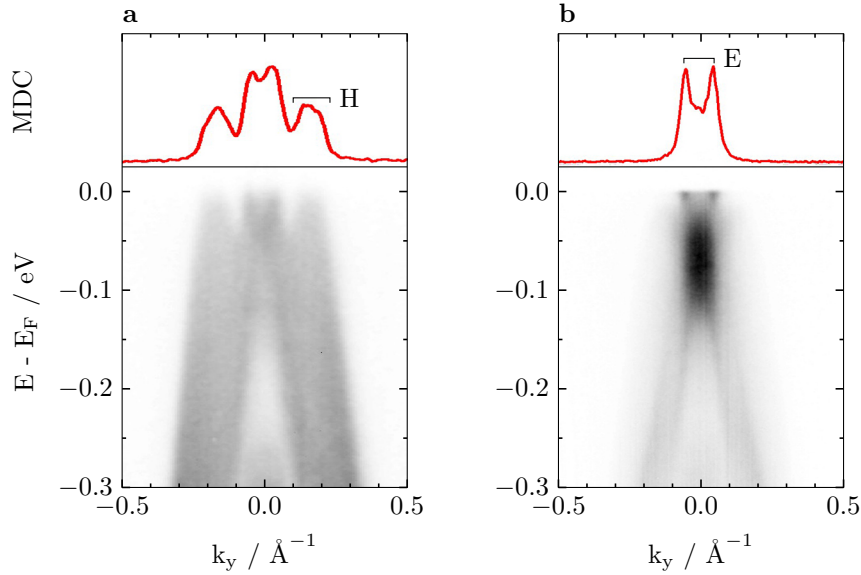


Figure 3.16: Analysis of the different possible cleavage planes. a) Energy momentum cut through the  $\Gamma$  point with the corresponding momentum distribution curve shown above the ARPES data. b) Energy momentum cut taken at a position between the large and the small hole pockets. The marked widths are of the same value as the ones in Fig. 3.15. Picture taken from [118].

again feature sizes are marked with “H” and “E”, corresponding to the features marked in the calculated maps of Fig. 3.15. The momentum scales of the lines are the same for both figures. As it can be seen, the correspondence is quite good, especially with the highlighted (001) surface.

As mentioned in section 3.3.3, one can compare de-Haas-van-Alphen data to ARPES data using the Onsager relation. The values added into this relation as well as the results are shown in Fig. 3.17b. When comparing to the measured de-Haas-van-Alphen frequencies the correspondence is very good.

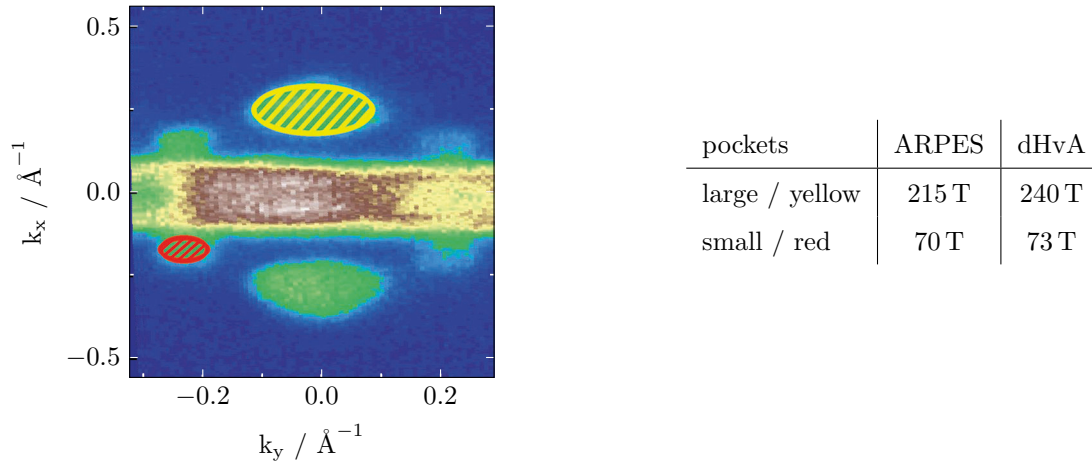


Figure 3.17: Comparison of de-Haas-van-Alphen (dHvA) measurements and ARPES data. Image: 25 eV photon energy Fermi surface map. The feature sizes, used within the Onsager relation are marked with yellow and red ellipses. Table: The calculated values from the Onsager relation and the measured values from dHvA. Panel a taken from [118].

### 3.4.3 Topology in TaIrTe<sub>4</sub>

As the measured surface is now discussed, a detailed analysis of the existence of surface features in TaIrTe<sub>4</sub> can now be conducted. With the crystal surface known, the band structure close to the Fermi energy as well as the Fermi surface can now be compared to the respective calculation for indications of topological states. In general, as the surface states of the (001) surface are expected to be along the hole pockets, it will be difficult to resolve them with ARPES, as the bright bulk states are overlapping with the thin surface states in the Fermi surface map.

For this comparison, the 25 eV Fermi surface map, belonging to the plane in the Brillouin zone at the  $\Gamma$  point, was taken, as it resolves the structure the best. This map is compared to the respective calculations. Two locations were chosen: an energy-momentum cut through the  $\Gamma$  point (Fig. 3.18a-c) as well as a location at the edge of the large hole pocket, being approximately the position of the Weyl point (Fig. 3.18d-f). For each energy-momentum cut a calculated, measured and the second derivative of the data is presented. On top of the ARPES energy-momentum cuts, momentum distribution curves are depicted, showing the intensity curve at the Fermi level.

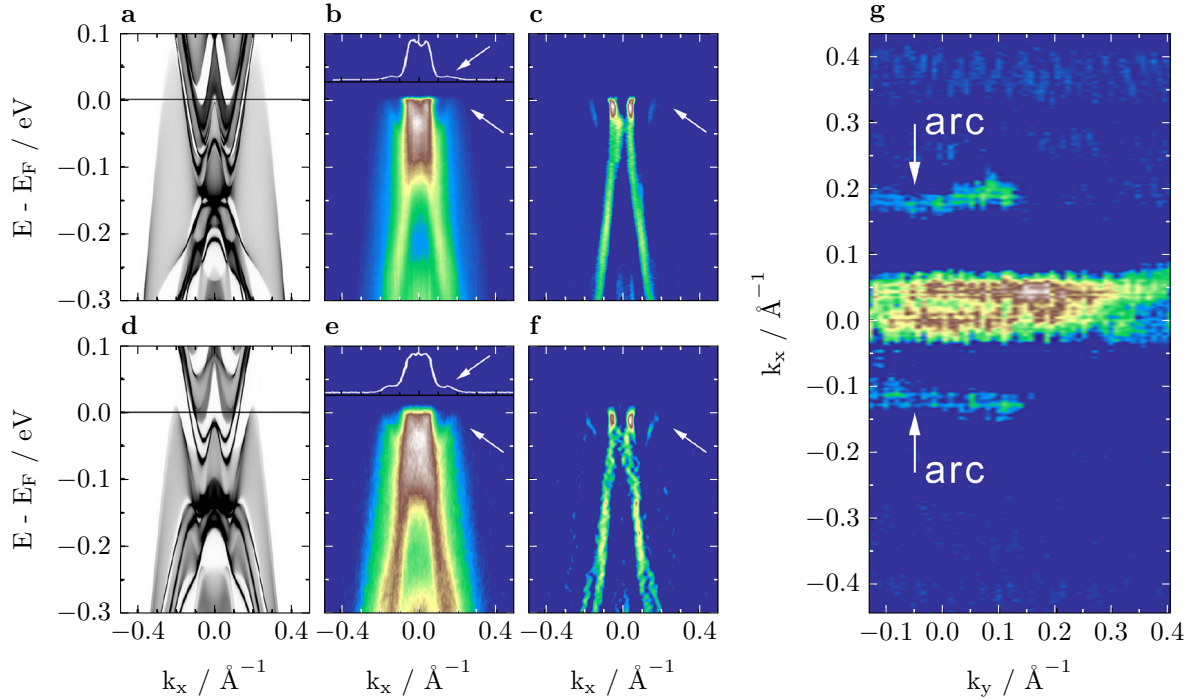


Figure 3.18: Surface states in ARPES maps and cuts. (a-c) Energy-momentum cuts through the  $\Gamma$ -point of the Fermi surface map. a) Calculated cut, b) measured ARPES data with the Fermi level momentum distribution curve shown above the data, c) second derivative of b). The locations of the surface feature are highlighted by arrows. (d-f) same as (a-c), but for a cut through the edges of the large hole pockets. g) Second derivative Fermi surface map, with the Fermi arc locations highlighted. Picture taken from [118].

An intense feature accompanying the bulk valence bands on their inner side is clearly visible in these cuts. The respective calculations also show a comparable feature at the same position. A very sharp and intense feature along the inner side of the outer hole band is going from approximately  $-0.1$  eV to  $0.1$  eV. Panels 3.18c and 3.18f, showing the second derivative of the ARPES data, highlight these bright features again. It is not believed, that this feature is due to the bulk band of the hole pocket, as the hole pockets always show an even distribution of intensity without any sharp edges. Thus, this edge is believed to belong to the surface feature of  $\text{TaIrTe}_4$ . When looking at a Fermi surface map build out of these second derivative energy-momentum cuts, these

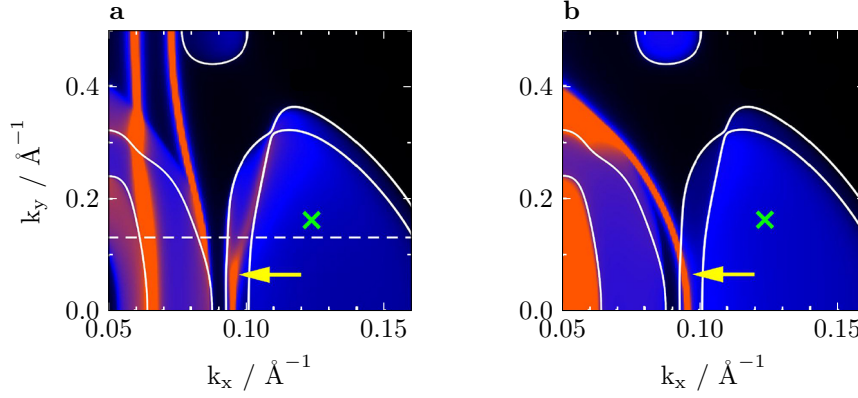


Figure 3.19: Calculated Fermi arc locations for the a)  $(001)$  and b)  $(00\bar{1})$  surface. The yellow arrows point to the calculated surface states. Panels are taken from [116].

intense features form an intense line, resembling a bright inner edge of the hole pocket at the expected arc positions. This map is shown in Fig. 3.18g. Comparing to the feature sizes from Fig. 3.13, the visible sizes in this map fit well within the size of the hole pockets. Out of this clear evidence,  $\text{TaIrTe}_4$  is stated to be a type-2 Weyl semimetal.

### Spin polarization of the topological states

As an additional prove for  $\text{TaIrTe}_4$  to be a Weyl semimetal, the spin polarization of the identified Fermi arcs can be measured. If these are surface features, the spin should be polarized. In addition,  $\text{TaIrTe}_4$  is non-magnetic - there should be no spin polarization visible anywhere else except on the arcs. Thus, a test for the spin polarization along the presented states in Fig. 3.18g can be seen as the ultimate proof of existence. Fig. 3.20 and 3.21 show the results of such 3D spin polarized ARPES experiments.

Spin polarization experiments were performed at the Hiroshima university HSRC synchrotron facility. During the experiments, both surface terminations were analysed at locations within the momentum space, where their topological states have been measured in the case of the  $(001)$  surface or where they are expected to be in the case of the  $(00\bar{1})$  surface. Both surfaces are again shown in Fig. 3.19, with the Fermi arcs highlighted by the yellow arrows and the Weyl points by green crosses.

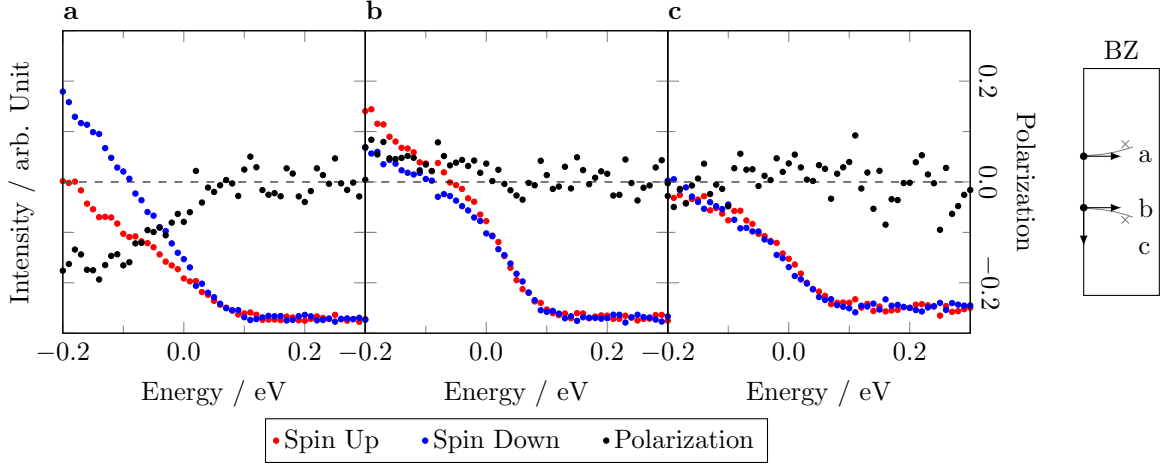


Figure 3.20: Spin polarization data of the Fermi arcs on the (001) surface observed in TaIrTe<sub>4</sub>. The measured positions are indicated on the Brillouin zone scheme on the right, showing half of a Brillouin zone with Fermi arcs and Weyl points indicated together with the measured positions and directions.

Dataset	measured axis	location in the Brillouin zone (*)
Fig. 3.20a	$k_y$	$k_x = -0.10 \text{ \AA}^{-1}, k_y = 0.0 \text{ \AA}^{-1}$
Fig. 3.20b	$k_y$	$k_x = 0.10 \text{ \AA}^{-1}, k_y = 0.0 \text{ \AA}^{-1}$
Fig. 3.20c	$k_x$	$k_x = 0.10 \text{ \AA}^{-1}, k_y = 0.0 \text{ \AA}^{-1}$

Table 3.1: Overview of the spin polarization measurements on the (001) surface. (\*): in relation to Fig. 3.19a.

### The (001) surface

On the (001) surface, two nearly parallel Fermi arcs are present at the centre of the Brillouin zone, stretching approximately to one third of the overall Brillouin zone size. These arcs have been measured with ARPES and are shown in the Fig. 3.18g, highlighted by the white arrows. In Fig. 3.20, the spin polarization of the two arcs of the (001) surface is shown with the configurations as shown in table 3.1. Panel 3.20a shows the result of one Fermi arc measured on the  $k_y$  direction. A strong polarization with a factor of up to  $-20\%$  is observed. Panel 3.20b shows the spin polarization of the other Fermi arc in the (001) Fermi surface. A polarization factor of  $10\%$  has been recorded for the spin polarization of a point on the other Fermi arc. As expected from

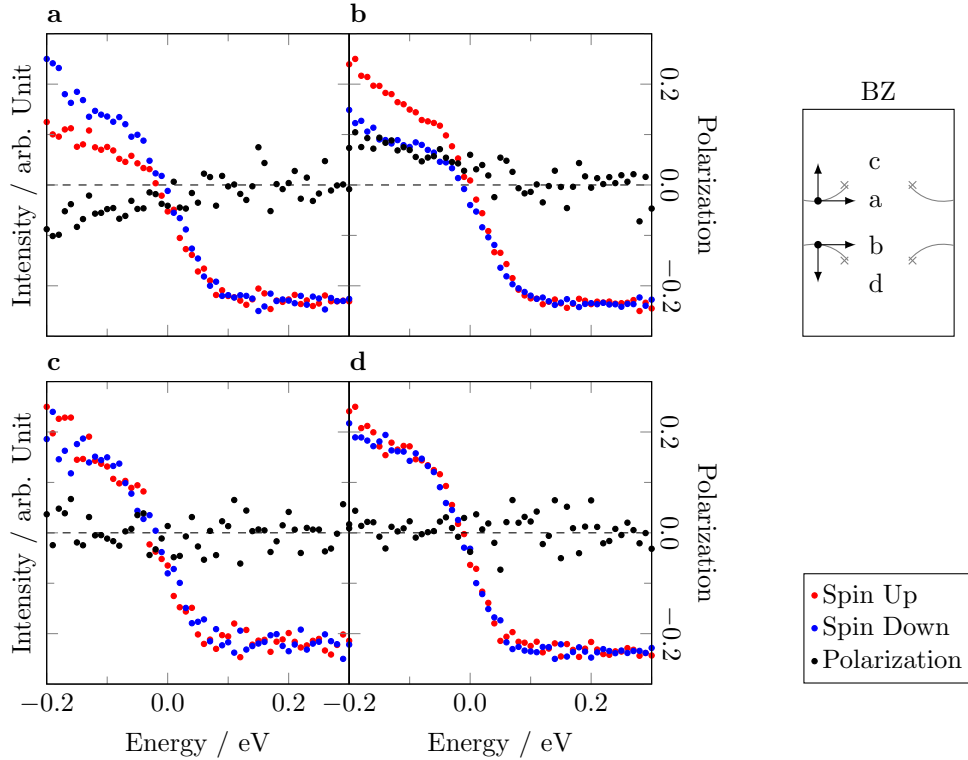


Figure 3.21: Spin polarization data of the Fermi arcs on the  $(00\bar{1})$  surface observed in  $\text{TaIrTe}_4$ . The positions in the Brillouin zone are highlighted in the scheme on the top-right.

Weyl semimetals, the polarization factors are of the opposite sign, highlighting the opposing spin directions as predicted by Fig. 3.5a). The data shown in panel 3.20c is measured on the same position as the one in panel 3.20b, but this time perpendicular to the Fermi arc. No polarization is seen in this case, showing that there is only a strong polarization along the measured Fermi arcs, but no spin polarization otherwise.

### The $(00\bar{1})$ surface

The  $(00\bar{1})$  surface does behave similar to the previously shown  $(001)$  surface - with different locations of the Fermi arcs as shown in Fig. 3.19b. The position of the arcs is again shown by a yellow arrow. In general, in comparison to the  $(001)$  surface, the arcs are now oriented from the Weyl points towards the  $Y$  point of the Brillouin zone. Details about the measurement location are given in table 3.2. Again, the polarization results of this surface show the same picture as the  $(001)$  one: a clear polarization is

Dataset	measured axis	location in the Brillouin zone <sup>(*)</sup>
Fig. 3.21a	$k_y$	$k_x = -0.05 \text{ \AA}^{-1}, k_y = 0.3 \text{ \AA}^{-1}$
Fig. 3.21b	$k_y$	$k_x = 0.05 \text{ \AA}^{-1}, k_y = 0.3 \text{ \AA}^{-1}$
Fig. 3.21c	$k_x$	$k_x = -0.05 \text{ \AA}^{-1}, k_y = 0.3 \text{ \AA}^{-1}$
Fig. 3.21d	$k_x$	$k_x = 0.05 \text{ \AA}^{-1}, k_y = 0.3 \text{ \AA}^{-1}$

Table 3.2: Overview of the spin polarization measurements on the  $(00\bar{1})$  surface. (\*): in relation to Fig. 3.19b.

visible along the Fermi arcs, with one being polarized spin-down (panel 3.21a) while the other side is polarized spin-up (panel 3.21b). The overall polarization factor is approximately 10% along the Fermi arcs. Again, when measuring perpendicular to the arcs, as shown in the results in panels 3.21c,d no polarization is observed.

### 3.4.4 Conclusion

As it has been shown in this chapter, TaIrTe<sub>4</sub> is a very interesting topological material. ARPES was used to analyse its electronic structure, which was then compared to calculations as well as with transport measurements. The overall agreement is remarkable.

We could prove the topological character by resolving the topological states in our Fermi surface maps, as well as confirming their non-trivial nature through spin polarization measurements which clearly stated a strong polarization along the arcs - in an otherwise non-magnetic material.

The now proved overall topological structure of this material again highlights its application potential: no other material with such a unique Weyl node configuration is known yet. The well separated nodes with their very long Fermi arcs are very good candidates for further research, for example on the chiral anomaly. Hopefully boosting possible applications utilizing the principle of switching charges at the Fermi level using magnetic fields.

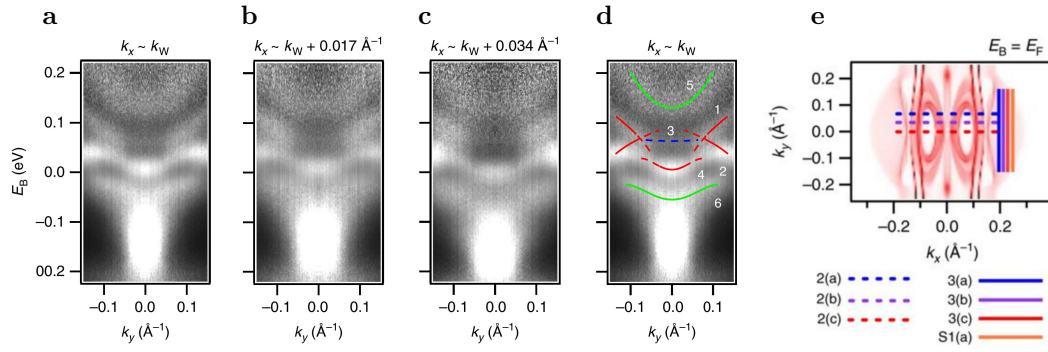


Figure 3.22: Pump probe ARPES energy-momentum cuts, taken from [121]. (a-c) Pump probe ARPES spectra at different fixed  $k_x$  showing dispersions above the Fermi level. d) Same data as in panel a), with possible locations of bands and features highlighted. Bulk bands are green, topological states red, the Fermi arc is dashed blue. e) Fermi surface calculation with solid lines drawn showing the positions of the cuts from panels (a-c).

## 3.5 Outlook

After the initial prediction, the growth and characterization as well as the ARPES proof, TaIrTe<sub>4</sub> kept sparking interest within fundamental research. Initial results of very recent, still ongoing research on TaIrTe<sub>4</sub> will now be highlighted shortly on the following pages.

### 3.5.1 Advanced ARPES measurements

As described in chapter 2.3.3, utilizing pump-probe ARPES allows one to measure above the Fermi level. When no pump-probe setup is available, the same effect can be achieved through doping with elements like potassium. Through this, the Fermi level can be raised to allow the measurement of bands above the Fermi level. While this method works very well with bulk states, it has to be treated with care when trying to measure surface states: due to the atoms on the surface the signal-to-noise ratio quickly decreases, non-reproducible alterations of the surface electronics can lead to unexpected results.

Pump-probe ARPES circumvents these problems and thus allows to directly measure



the Weyl points, which are located slightly above the Fermi level in TaIrTe<sub>4</sub>. Fig. 3.22 shows the results of Belopolski et al [121] stating to resolve the Weyl points and the Fermi arc directly connecting them. Three energy-momentum cuts measured by pump-probe ARPES are shown in panels 3.22a-c. In contrast to all previously discussed energy-momentum cuts, the orientation of these shown here is different, as highlighted in the Fermi surface map in panel 3.22e. The data corresponds to the cuts along the long sides of the large hole pockets at fixed  $k_x$  values. Dispersions can be seen in these panels, despite a lower signal-to-noise ratio. Panel 3.22d shows the same cut as panel 3.22a, but this time they highlighted the band structure with coloured lines: The Weyl cones being the red crossing lines (1) and the Fermi arc the dashed blue line (3).

### 3.5.2 Superconductivity

Recently, STM and transport data showing superconducting behaviour in TaIrTe<sub>4</sub> was shown by Xing et al. [125]. They measured in a temperature range from 0.4 K to 1.5 K. Fig. 3.23 shows the most important parts of their results. A typical STM picture at very low temperatures of 4 K showing quasi-1D superconductivity in panel 3.23a. Panel 3.23b shows a normalised differential conductance  $dI/dV$  measured at 0.4 K. A v-shaped superconducting gap is visible with a width of approximately 1.2 meV. The gap seen is also quite shallow with a depth smaller than 10 %. The authors relate this shallow gap to a topological origin of the superconductivity.

Taking new, yet unpublished, transport measurements from the IFW Dresden into account, it can be said that the resistivity never completely vanishes. At the critical temperature “ $T_C$ ” the resistivity drops by larger amounts nearly immediately, but a certain offset remains. The exact origin has yet to be analysed, but first ideas discussed include, that the bulk electronic structure changes into a superconducting phase, whereas the protected electronic states of the topological phase stay. This seems to contradict the topological superconductivity idea, but highlights the interesting nature of the material.

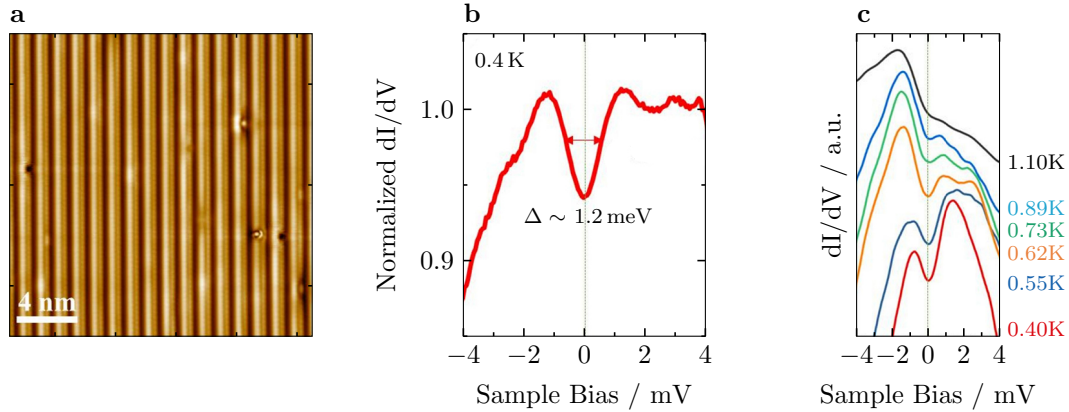


Figure 3.23: STM results measured by Xing et al. a) Typical STM topographic image of the cleaved TaIrTe<sub>4</sub> surface highlighting a quasi 1D structure. b) Normalized differential conductance dI/dV spectrum measured on a terrace of TaIrTe<sub>4</sub>. Visible is a V-shaped superconducting gap of 1.2 meV. The shallow depth of the gap implies the superconductivity to be related to the surface states. c) Temperature dependence of the gap from 0.4 K to 1.1 K. Figure taken from [125].

### 3.5.3 Ta(IrRhRu)Te<sub>4</sub>

Like the substitution of tungsten with molybdenum within the Mo<sub>x</sub>W<sub>1-x</sub>Te<sub>2</sub> system to slightly change and ultimately tune the surface properties of these compounds, these possibilities are also analysed for TaIrTe<sub>4</sub>. Due to the similarities of iridium and rhodium, a substitution of Ir with Rh was focussed, as no dramatic changes in the bulk structure should appear. Due to rhodium having a significant lower strength of spin-orbit coupling, a tuning of the exact Fermi level or the Weyl point position might be possible. Additionally, chemical doping was checked - with ruthenium doping, replacing either iridium or rhodium, showing very interesting results.

A whole series of samples from pure TaIrTe<sub>4</sub> to pure TaRhTe<sub>4</sub>, as well as an assortment of different ruthenium doping levels were grown and analysed with transport measurements. Results from three interesting representing samples are shown in Tab. 3.3. It can be seen, that the carrier mobilities are varying a lot.

Very interesting are the additional findings, that when comparing TaIrTe<sub>4</sub> to TaRhTe<sub>4</sub>, the quadratic behaviour of the magneto-resistance changes for higher fields to a linear

Sample	remarks
TaIrTe <sub>4</sub>	Quadratic magneto-resistance behaviour
TaRhTe <sub>4</sub>	Quadratic magneto-resistance, not depending on magnetic field orientation
TaRh <sub>0.92</sub> Ir <sub>0.08</sub> Te <sub>4</sub>	3 superconducting phases with different T <sub>C</sub> 's each

Table 3.3: Overview of compositions from the Ta(IrRhRu)Te<sub>4</sub> system where initial calculations, transport and ARPES data is available.

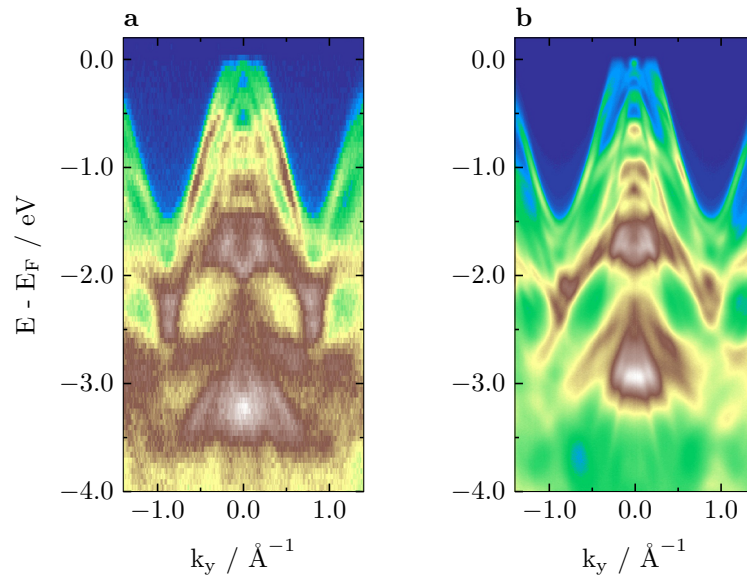


Figure 3.24: ARPES energy-momentum cuts taken at 100 eV photon energy. a) TaIrTe<sub>4</sub>, b) TaRhTe<sub>4</sub>.

one. In regards of the superconductivity, the compound TaRh<sub>0.92</sub>Ir<sub>0.08</sub>Te<sub>4</sub> turned out to be especially interesting, as it shows three overlapping superconducting phases, with the highest critical temperature of approximately 4 K.

Initial ARPES data has been recorded for TaRhTe<sub>4</sub> as well as the compound with the 4 K critical temperature. Figs. 3.24 and 3.25 show these results. While these results are not differing on a larger scale, the discussion in regards of topological states requires a very detailed analysis of high resolution data collected around the Fermi level.

Comparing these results, first of all, the major correspondence between these two compounds is noteworthy. Looking into more detail, differences become visible at the absolute energy scale. The feature between 93.6 eV and 92.8 eV in the TaRhTe<sub>4</sub> plot

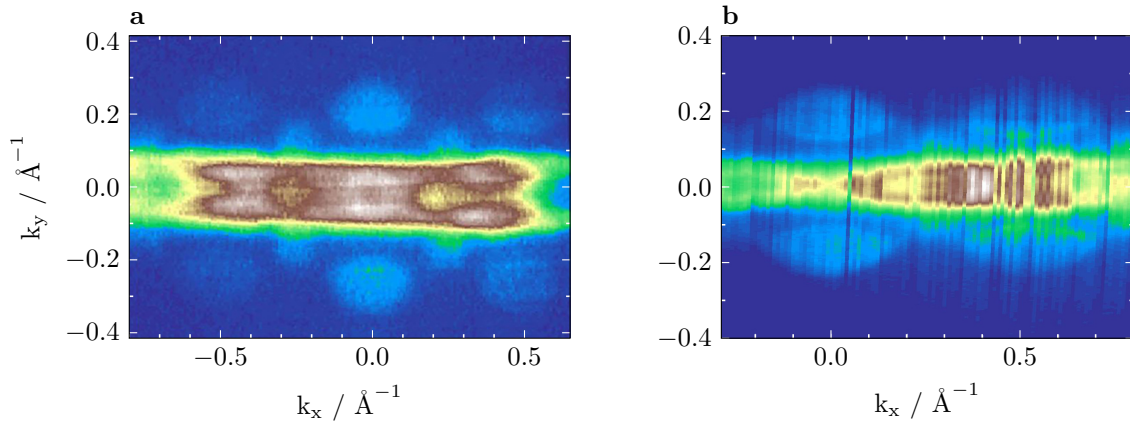


Figure 3.25: ARPES Fermi surface maps taken at 25 eV photon energy. a) TaIrTe<sub>4</sub>, b) TaRhTe<sub>4</sub>.

is on a higher position than in the TaIrTe<sub>4</sub> plot. Also, between 94.8 eV and 95.6 eV, similar features can be found for both materials, but with shifted positions.

Fermi surfaces of both materials are shown in Fig. 3.25. Again, the Fermi surfaces don't differ on a larger scale: a central feature consisting of electron pockets is visible, accompanied by large and small hole pockets.

In contrast to TaIrTe<sub>4</sub>, intense edges on the inner sides of the large hole pockets are visible, even without the need of a second derivative transformation to highlight the edges. It is believed, that these features, as they are in TaIrTe<sub>4</sub>, are the Fermi arcs.

# 4 GaGeTe - a simple topological semimetal

GaGeTe was first mentioned in [126, 127], more than 30 years ago. In these publications the synthesis and crystal structure of GaGeTe is described. Shortly after, its phonon structure [128] was analysed in more depth. Until now, thermoelectric [129] and transport properties [130] were studied.

First theoretical study of the bulk electronic structure appeared very recently [42] and will be discussed in the next chapter. This work sparked lot of interest in the surface electronic structure [131], showing the possibility of a strain induced band gap tuning in these layers, ranging from close to no band gap at all up to approximately 1.1 eV width.

Theoretical [131] and experimental [132] work additionally shows, that thin “mono”-layers of GaGeTe, consisting only of the 6 atom-sheets Te-Ga-Ge-Ge-Ga-Te, and which are connected by Van-der-Waals bonding, which are exfoliated from bulk GaGeTe crystals, are suitable for fabrication of electronic nano-devices including transistors and photodetectors. This highlights the large application potential of GaGeTe and the need to understand the electronic structure in full detail.

## 4.1 Theoretical aspects of the GaGeTe band structure

The crystals of GaGeTe are consisting of six-atom thick layers: a two-atom germanium sheet, arranged in an armchair configuration. This germanium sheet has striking similarities to germanene, a material like graphene, silicene or stannene. This group

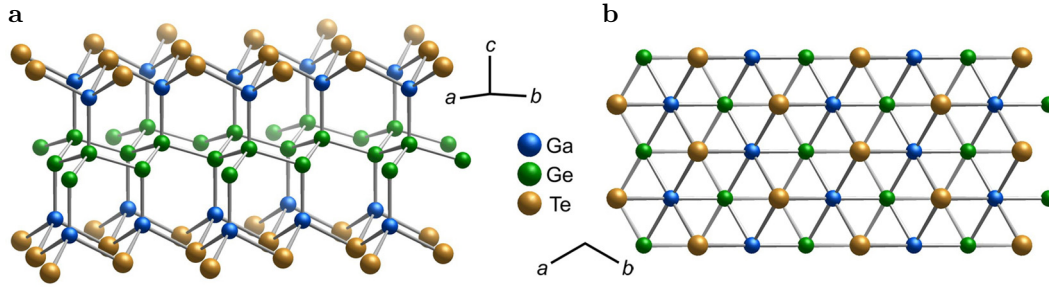


Figure 4.1: Schematic layered structure of GaGeTe. The germanene sheet is enclosed by Ga-Te sheets, organized in the way, that a layer always terminates with Te. a) perspective view, b) top view. Picture taken from [133].

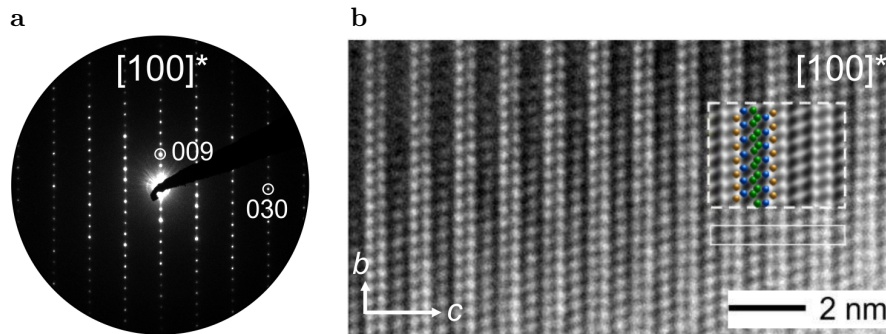


Figure 4.2: HRTEM data of a GaGeTe crystal. a) main  $[100]^*$  zone PED, b) experimental  $[100]^*$  zone HRTEM micrograph with simulation ( $f = -50$  nm,  $t = 4.04$  nm) inset. Picture taken from [133].

of materials is expected to host topological properties, such as the quantum spin Hall effect. The germanene sheet is enclosed by two Ga-Te sheets, being oriented in the way that Te is always pointing away from the germanene sheet. A schematic overview of this structure is shown in Fig. 4.1.

The stacking of the material layers has been confirmed by high-resolution TEM measurements, presented in Fig. 4.2. Panel 4.2a shows the main  $[001]^*$  zone precession electron diffraction pattern. Panel 4.2b shows the corresponding HRTEM micrograph with a simulated image inset in the dashed box. A very good correspondence between the measurement and the expected crystal structure is visible, highlighting the lack of major stacking faults within the crystals.

GaGeTe crystallizes in a trigonal unit cell with space group  $R\bar{3}m$ . The corresponding

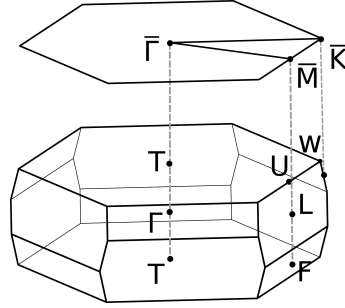


Figure 4.3: Brillouin zone of GaGeTe with the projected surface Brillouin zone sketched above it. Picture taken from [42].

Brillouin zone is highlighted in Fig. 4.3. Notable, especially for ARPES measurements, are the alternating sides of the hexagon. ARPES data is usually measured along a linear cut through that zone, with the exact angle and position depending on the crystal orientation in the beam. Data taken on the line  $L-\Gamma$  expended to a  $L'$  on the other side would be slightly altered and not necessary symmetric.

DFT calculations show, GaGeTe being a narrow band gap topological insulator. But, when changing the exchange correlation functional, a part of the calculations defining the exchange interactions within the electronic system, this picture changes. Utilizing the HSE06 exchange correlation functional, GaGeTe becomes an insulator with a relatively large band gap. A detailed discussion of the different exchange correlation functionals can be found in reference [134]. In general it can be stated, that each functional does have its pros and cons, but differences as large as seen within GaGeTe can be viewed unusual showing possible difficulties of the functionals to correctly calculate the electronic structure on such a small range as present in GaGeTe. Thus, a detailed analysis of different calculation methods is needed as well as an experimental confirmation through ARPES is regarded mandatory.

The material has a gapless band structure in the scalar-relativistic case, shown in Fig. 4.4. The top of the valence band is the Te-5p<sub>z</sub> state and the minimum of the conduction band is the Ge-4s state. Also clearly seen is, that the material does have a very large band gap in all other positions. When switching on spin-orbit coupling, the gap opens up. Details about specific bands and their respective locations can be found in [42]. This behaviour can be seen in Fig. 4.5.

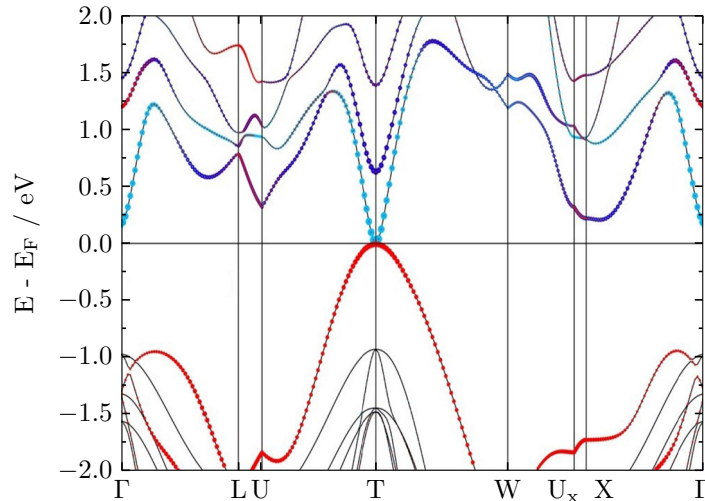


Figure 4.4: Band structure of GaGeTe, computed in a scalar-relativistic way but without SOC. The PBE functional was used. Picture taken from [42].

It turned out, that calculations using HSE hybrid functional shows a band gap larger than the other functionals. These results are also shown in Fig. 4.5, clearly showing a gap of ten times the size. Due to this major difference, more functionals and different software tool sets were tested. These tool sets were: FPLO [120], ELK software package [135] and VASP [136–138]. The results of the band gap for the different functionals and software combinations are shown in Tab. 4.1. The result of the GW-approximation is shown in Fig. 4.6. The results of GW are also indicating a trivial material, with a band gap smaller than the one calculated with the HSE functional, but still five times larger compared to using the PBE functional.

Overall it can be seen, that the choice of the functional or usage of the GW approximation strongly influences the electronic structure, especially close to the Fermi level. Out of theory, it can not be said, which of these functionals computes a result, actually representing the real sample. Therefore detailed experimental data is needed to narrow down the choice of functionals.

Additionally it can be seen in the inset in Fig. 4.5, that PBE including spin-orbit coupling induces a band inversion at the T-point. This feature is similar in shape and position in the overall band structure to  $\text{Bi}_2\text{Se}_3$ , despite being approximately ten times smaller. The predicted surface state in GaGeTe when using the PBE functional is shown in Fig. 4.7. Calculating the four topological  $\mathbb{Z}_2$  invariants  $\nu_0; (\nu_1\nu_2\nu_3)$  for



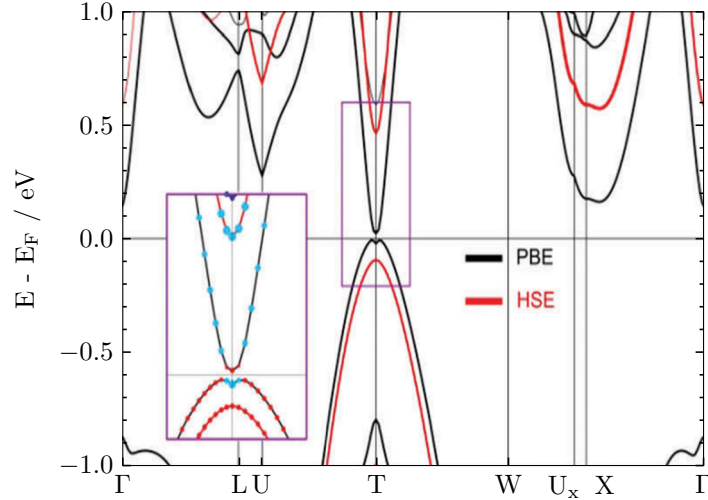


Figure 4.5: Comparison of the band structure of GaGeTe with SOC taken into account for the functionals PBE (black) and HSE (red). Picture taken from [42].

method-functional	band gap [meV]
using experimental GaGeTe geometry	
FPLO-LDA	57
FPLO-PBE	29
ELK-FPLAPW-LDA	70
VASP-PAW-PBE	33
using optimised geometry of GaGeTe	
FPLO-LDA	21
VASP-PAW-PBE+D3	55
VASP-HSE	550
GW	298

Table 4.1: Overview of the used software-method-functional combinations and their respective results for the band gap.

the time reversal invariant momenta would classify GaGeTe as a strong topological insulator with  $\mathbb{Z}_2 = 1;(111)$  for the primitive cell, which would transform to  $\mathbb{Z}_2 = 1;(001)$  in the conventional cell. For these calculations VASP and FPLO return the same result. The  $\mathbb{Z}_2$  values for HSE have been calculated as well, but these results are just showing a trivial material in case of the HSE functional.

In case, that HSE turns out to be the correct functional, GaGeTe would not be a topological insulator, but a trivial material. In this case, as suggested by [42], Ga and Ge could be replaced by isovalent elements with higher atomic numbers, such as In or Sn. These elements would introduce a stronger spin-orbit coupling and thus enforcing the band inversion on a much larger scale, while being comparable to GaGeTe in all other parts of the band structure. For these materials, the difference with the gap, when calculating using PBE or HSE, stays the same, but both show a non-trivial state. This shows, that the small effect of the weak spin-orbit coupling in GaGeTe leads to noteworthy inaccuracies with many computational techniques. Because of this, a careful breakdown of this data together with experimental results is needed to get a clear picture of GaGeTe.

Here, a comprehensive ARPES analysis of the electronic structure of GaGeTe is presented. ARPES on GaGeTe turned out to be more complex than initially thought. The layered structure usually helps the measurement a lot, due to the “predefined” cleavage planes as well as the already denoted Tellurium-only terminations. It turned out, that cleaving GaGeTe will not result in relatively large, plane surfaces. Most cleaves, especially on larger crystals turned out to have a fractured surface. The use of very small crystals increased the chance of planar surfaces, but still the overall success was low.

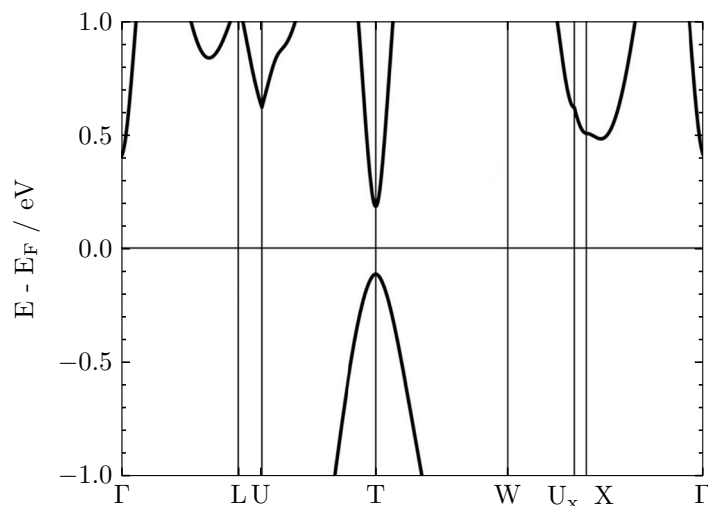


Figure 4.6: Band structure of GaGeTe calculated with SOC taken into account utilizing the GW approximation. Picture taken from [42].

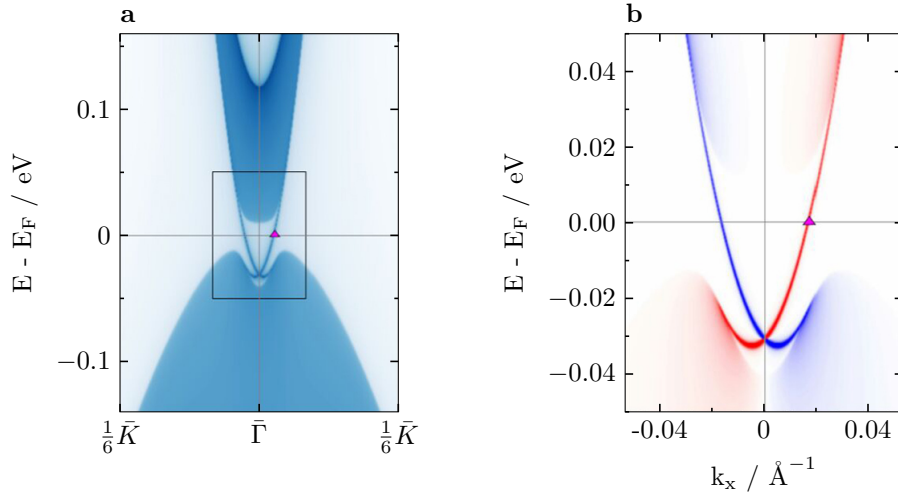


Figure 4.7: Topological surface states of GaGeTe, as expected by [42] through initial calculations using PBE. a) Density of states, b) spin polarization of the topological states. Picture taken from [42].

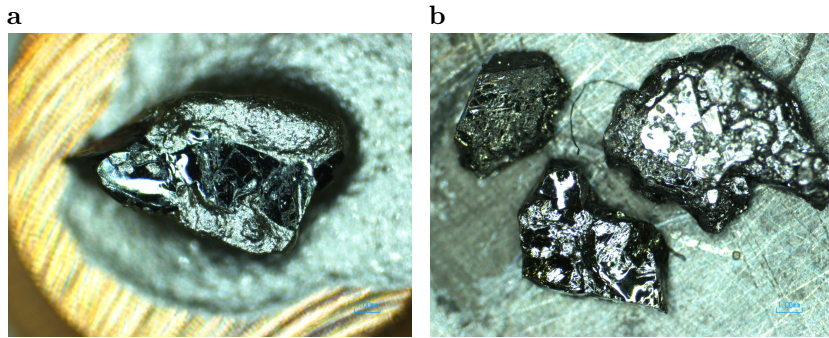


Figure 4.8: Pictures of glued GaGeTe crystals. These pictures were taken after the experiment to analyse signal quality in regards to the sample surface. The surfaces are very fractured and no larger mirror like regions are visible.

In the lab, cleaving with sticky tape was tested and worked out well. While the surface of the crystals are substantially better, this method does have other difficulties: the photon energy in our lab is not variable as well and not focussed light in comparison to a synchrotron. Additionally, sticky tape does not work for cleaving on most manipulators and does not work for cleaving at very low temperatures. The thus required transfers and movements in the chamber are a cause for less ideal vacuum. During the cooling process, additional dirt can settle on the sample surface. These effects are possibilities where the surface can get dirty again before the actual measurement.

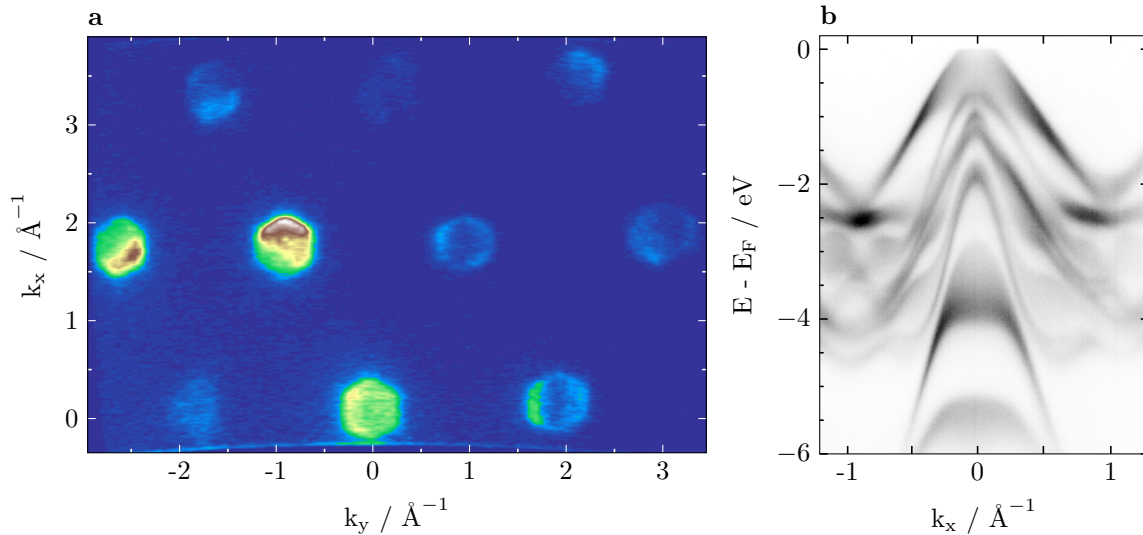


Figure 4.9: a) Fermi surface map of GaGeTe taken at 180 eV photon energy. The trigonal symmetries of the system as well as the metal like Fermi surface behaviour. b) An energy-momentum cut taken at 100 eV. Picture taken from [133].

## 4.2 ARPES on GaGeTe

ARPES spectra have been recorded and are shown in Fig. 4.9. An energy-momentum cut taken at 100 eV and a Fermi surface map taken at 180 eV are seen. The energy-momentum cut shows the bands approximately along the L- $\Gamma$ -T direction of the Brillouin zone. It ranges from the Fermi level to  $E_{\text{Fermi}} - 6$  eV in energy direction and shows the high symmetry points in momentum space at  $-0.8 \text{ \AA}^{-1}$ ,  $0.0 \text{ \AA}^{-1}$  and  $1.0 \text{ \AA}^{-1}$ . Alongside a visible clear Fermi edge, indicating that bands cross the Fermi level. A more detailed discussion of the bands will be done later with the support of theory.

The Fermi surface map of Fig. 4.9 shows the symmetry within the Brillouin zone very well. The features themselves show a trigonal symmetry with their hexagonal shape. These hexagonal shapes are also visible when looking at the orientation of these points. The changes in intensity of the different Brillouin zones can be attributed to the matrix element of the material. Because of this, the  $\Gamma$ -point at  $(0, 0) \text{ \AA}^{-1}$  is more intense than the T-point at  $(0, 3.5) \text{ \AA}^{-1}$ . The map also highlights, that there are states crossing the Fermi level for certain high symmetry positions. This would contradict the idea of a large band gap and GaGeTe being a semiconductor.

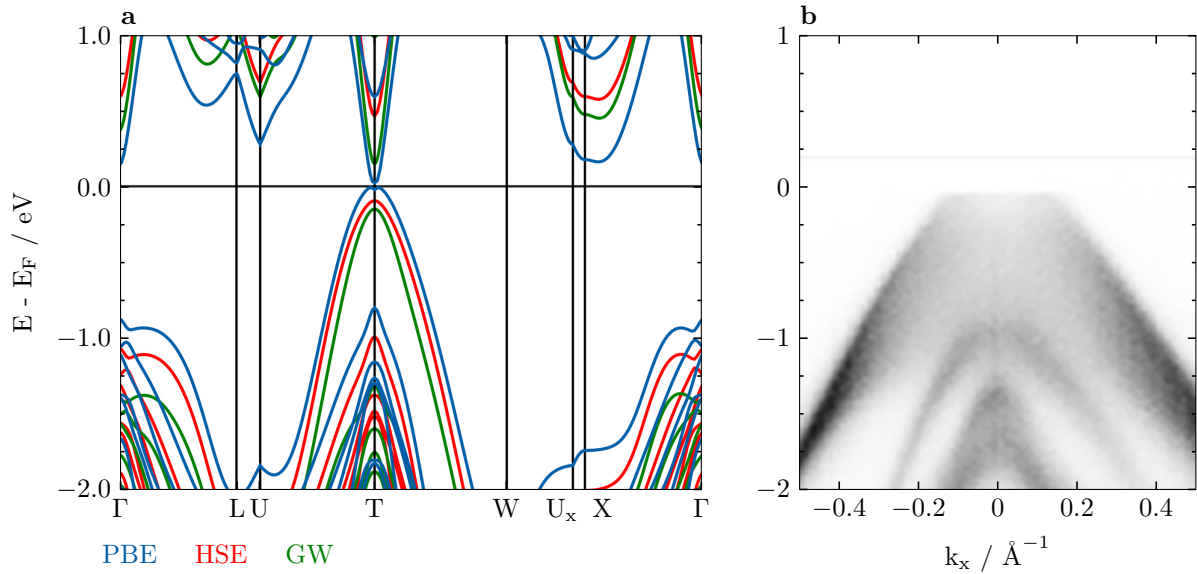


Figure 4.10: a) Calculated band structure using PBE (blue), HSE (red) and GW (green) in the range from 1 eV to  $-2$  eV. b) Measured energy-momentum cut taken at 100 eV at an corresponding energy scale.

Fig. 4.10 depicts a comparison of the band structure calculated using the PBE, HSE and GW functionals in panel 4.10a together with the corresponding region in the energy-momentum cut in panel 4.10b. Comparing these three different functionals to the ARPES data, some things become noteworthy: the ARPES data shows a clear Fermi edge. If GW or HSE would be a correct type of calculation, a large band gap would be directly within a very small energy range above the Fermi level, as otherwise the difference between calculation and bulk bands would not fit anymore for the measured bands at  $\sim -1$  eV. The PBE functional with its very small gap is fitting this better. Looking into the PBE calculation, the topmost band moves between the Fermi level and  $-1$  eV, with a second band residing right at  $-1$  eV with no large changes along the  $k_z$  axis. A similar behaviour can be observed in the ARPES data, with the topmost band being blurred over approximately 1 eV on the energy scale. Due to this, the focus is oriented at the PBE based calculations - yet the other results can not be excluded yet. To clarify this, an analysis of the possible band gap has to be done.

As ARPES is limited by the Fermi level and special experimental setups, which would allow to measure above the Fermi level, were unavailable at the time of experiment,

approximately half a monolayer of potassium was evaporated on the sample to achieve a similar effect. Dosing with an electron donor raises the chemical potential in the material, thus looking like a shifted down spectra compared to undosed ARPES measurements. The results of the evaporation are shown in Fig. 4.11. Depicted are energy-momentum cuts before and after the evaporation process. The measured range was the same both times, being 6.3 eV. As the sample needed to be moved out of the measuring position for evaporation, the momentum axis are not exactly the same. Still, both times the sample has been adjusted to comparable positions. For a guide to the eye, white lines have been drawn on distinct band structure features to allow a better comparison of their absolute energy value. Clearly visible is the shift of the bands down to lower energies, with an approximate shift of 330 meV.

More details close to the Fermi level are shown in Fig. 4.11c, d. Their position in regards to panels 4.10a and 4.10b is shown by the dashed boxes within them. Looking into the data, a shift is also visible here. For example, the feature at (0, -0.65) seen in panel 4.10c moves down and thus is not visible in panel 4.10d anymore. At the Fermi level, the intensity does not vanish. Although the absolute intensity is only a fraction of the undosed intensity, a clear step is still visible. Above the energy-momentum cuts, momentum distribution curves taken directly at the Fermi level are shown. Again, there is a clear intensity seen compared to the background noise for the dosed sample, but the overall signal-to-noise ratio decreased a lot. This is a common unfortunate problem of dosing samples by depositing a certain amount of material as a surface layer on the crystal. This layer causes the signal to get worse - the more atoms the worse the signal, due to strongly increased scattering of the electrons when crossing through this layer.

In addition to the already discussed features, no charging was observed during these measurements. Charging can be considered as a clear indication, that the measured material is a semiconductor with its gap being at the Fermi level. Thus, no charging can be considered as no band gap being at the Fermi level. The conclusion is, that there is no large band gap in GaGeTe. With a shift of 0.33 eV a potential large gap should be clearly seen. A gap above the reached shift of 0.33 eV can be ruled out by the band structure calculations, as major other features would then required to be shifted

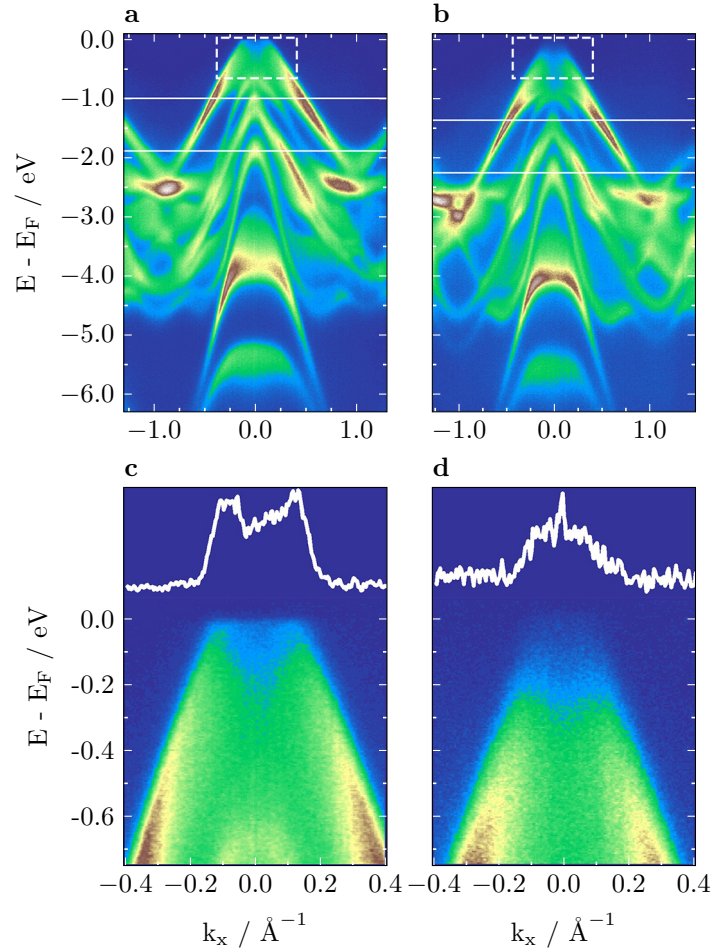


Figure 4.11: In-situ surface doping experiment of GaGeTe. a) Undoped and b) doped energy-momentum cut taken at 100 eV. Two distinct features in the band structure are highlighted with white lines for better comparison of their respective energy positions. c), d) Zoomed-in versions corresponding to the dashed boxes in panels a) and b). Added above the cuts is the respective momentum distribution curve for  $E_{\text{Fermi}}$ . Picture taken from [133].

and thus not fitting to any calculation anymore.

Now, that the proposed gap of the calculations has been discussed in regards to experimental data, a closer look into the band structure is taken. For this, the band structure is compared to calculations using the PBE functional, as GW and HSE already do have substantial differences in terms of the band gap.

Band structure and calculations using PBE are shown in Fig. 4.12 for a very large range of energies down to  $-6 \text{ eV}$ . Presented calculations are done for many different

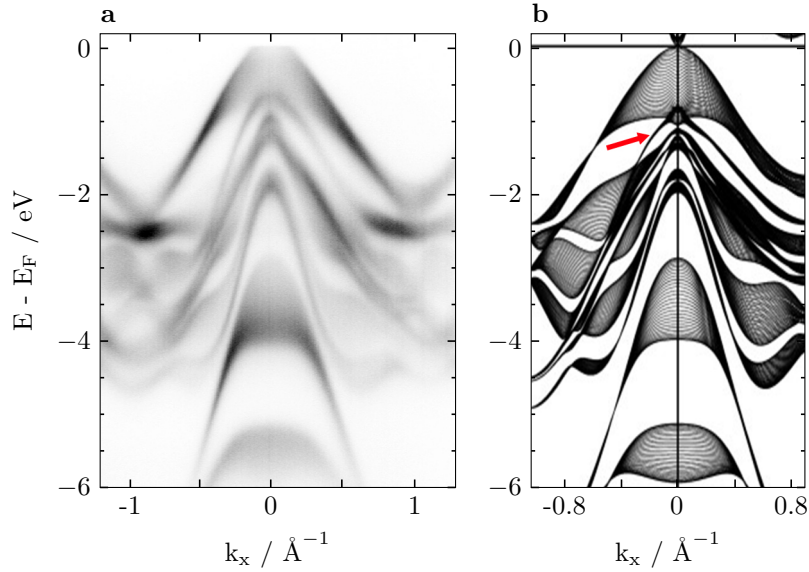


Figure 4.12: Detailed comparison of a) the calculated band structure using PBE and b) the measured ARPES energy-momentum cut. Picture taken from [133].

$k_z$  positions from  $\Gamma$  to T-point and then overlapped into one picture. This allows for a basic comparison with energy-momentum cuts having a certain  $k_z$  integration. Starting with the bands with a high  $k_z$  dispersion, their correspondence in regards of the position on the energy scale is fitting very well. Guides to the eye have been drawn into the panels to highlight this. Additionally, the calculated  $k_z$  dependency of the band fits the measured one remarkably well. The case is similar for the less  $k_z$ -dependent bands. Most of these are corresponding very well except of one band, approximately  $-1$  eV away from the Fermi level, also highlighted with a red arrow. Comparing this band to the measured spectrum, the calculation shows the band approximately 200 meV lower. Still the overall agreement between the calculated band structure using PBE functional and the measured spectra is remarkably good. Only one band close to the Fermi level, does not fit. Despite being just one band, this discrepancy might get important when looking more closely at the bands around the Fermi level, as done later in section 4.2.1. Fig. 4.13 shows a more detailed comparison in regards of the  $k_z$ -behaviour. Band structure calculations, depicted in panels 4.13a-d, show bands for  $k_z$  values of  $0 \text{ \AA}^{-1}$ ,  $0.05 \text{ \AA}^{-1}$ ,  $0.16 \text{ \AA}^{-1}$  and  $0.27 \text{ \AA}^{-1}$  corresponding to the range from  $\Gamma$  to T point with intermediate steps. The energy ranges from 1 eV to  $-5$  eV. As already discussed in Fig. 4.12, a certain set of bands have a high  $k_z$  dependency. The exact behaviour of



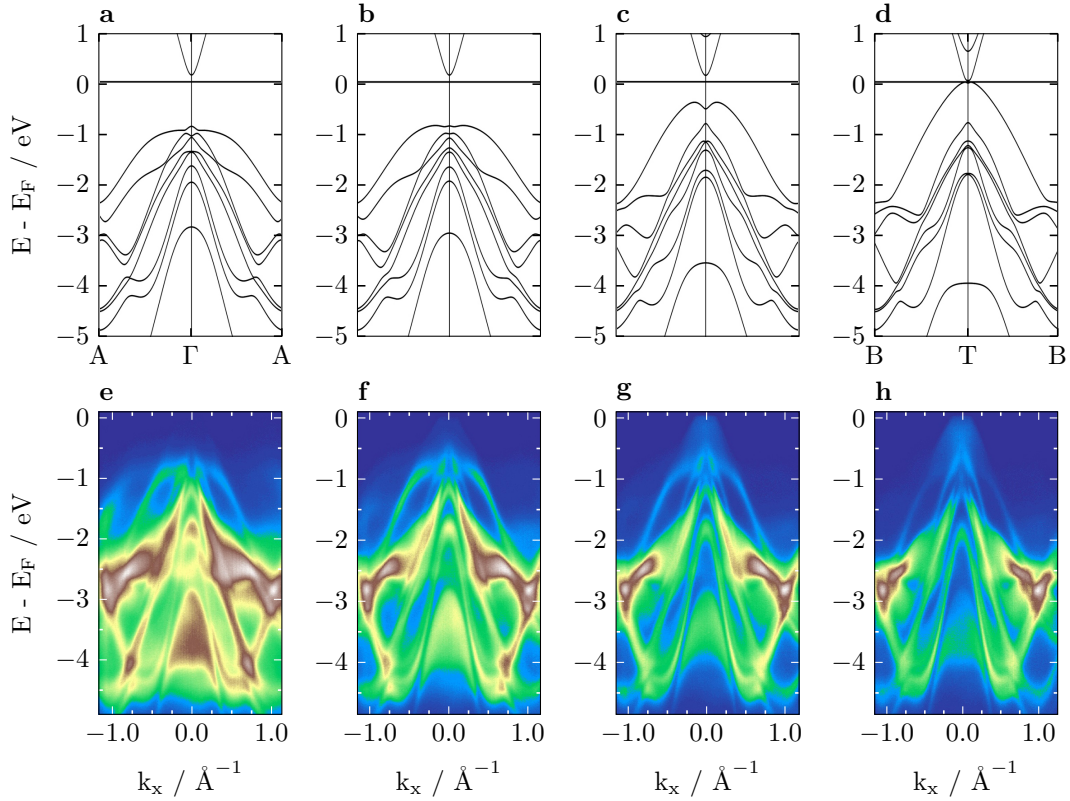


Figure 4.13:  $k_z$  dependency of the band structure: (a-d) calculated band structures for the single  $k_z$  values of  $0 \text{ \AA}^{-1}$ ,  $0.05 \text{ \AA}^{-1}$ ,  $0.16 \text{ \AA}^{-1}$  and  $0.27 \text{ \AA}^{-1}$  ranging from the  $\Gamma$  to the T point. (g-j) measured energy-momentum cuts at energies ranging from of 91 eV to 100 eV in equidistant photon energy steps. Picture taken from [133].

these bands can now be seen in more detail: the topmost valence band moves from a maximum at approximately  $-1 \text{ eV}$  up to the Fermi level. Similar movement shows the lowest band in the figure, moving from  $-3 \text{ eV}$  to  $-4 \text{ eV}$ . These movements can be traced very good with ARPES, as shown in the bottom row of this figure. In the case of the topmost band, the intensity is at approximately  $-1 \text{ eV}$  in the left panel, but moves up until a clear Fermi edge is seen in the right panel - just like theory predicted. A similar, but less clear shift is seen for the lower band. Due to the finite  $k_z$ -integration of ARPES, no sharp bands can be resolved. Still, the main intensity shifts in the same way as the calculation suggests. This again highlights how well PBE fits to the measured structure.

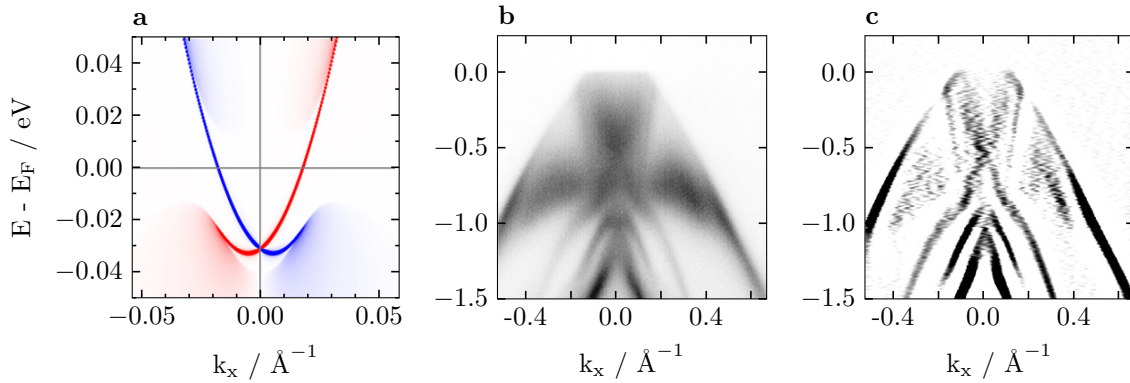


Figure 4.14: Comparison of calculations of the topological states with ARPES data. a) Calculated surface states on top of the band at the T-point. Red and blue highlight the different spin polarization. b) Energy-momentum cut taken at 19 eV photon energy to better resolve the bands close to the Fermi level. c) Same as b), but with edges highlighted using a second derivative. Picture taken from [133].

### 4.2.1 Topology in GaGeTe

So far, it was proven that PBE based calculations can reproduce the measurement the best. As mentioned in the discussion of the calculations, PBE also shows a band inversion at the T-point. This will now be analysed in more detail. Fig. 4.14 shows the states based on the calculations. On the top band a small dip is expected which contains the surface state connecting to the conduction band which is above the Fermi level.

Panel 4.14b shows an energy-momentum cut taken at 19 eV photon energy. Panel 4.14c is a second derivative of the measured data, essentially highlighting edges in the picture. Comparing the measured and calculated data for this small region close to the Fermi level, larger differences are visible than before. Clearly seen in the middle is a parabola-like structure coming into the picture from the top. Therefore we state, that this feature is a part of a conduction band. Comparing to the calculation, this is not reproduced by theory. Experiment shows no direct band gap at all, compared to the small direct band gap from theory. Still, one could alter the calculated structure in a way highlighted in Fig. 4.15. This would mean, that the topmost valence band, having its “M”-shape would rise up higher, whilst the lowest conduction band, with

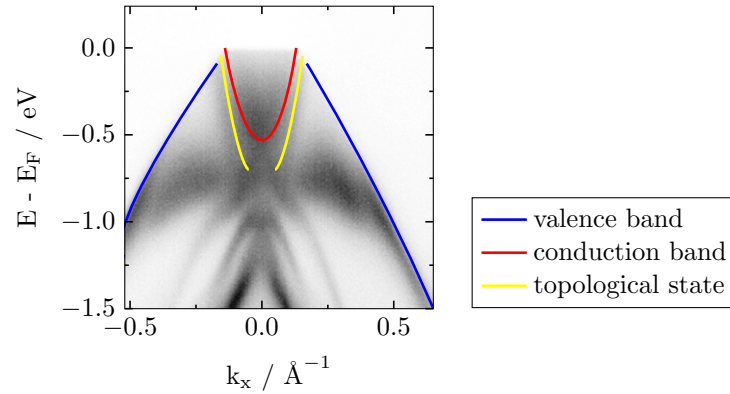


Figure 4.15: Suggested nature of the measured bands of GaGeTe. The red parabola highlights the contour of a conduction band coming from the top, the blue lines the contour of the topmost valence band going up very close to the Fermi level. Shown in yellow are possible traces of the surface states, accompanying the conduction band parabola.

it's “V”-shape, would dip into this “M” - while maintaining an indirect band gap. This would also explain, why there is no gap visible in the Fermi surface.

The signature of the topological state is unfortunately not as sharp as it is expected from surface states. This is found to be because of the rough surface of the cleaved crystals. Several crystals have been cleaved and only the data from the best cleaving results are shown in this chapter. Still, those surfaces are not completely mirror like, often showing either steps on the surface or holes ripped into the surface through several layers. A similar behaviour can be seen in  $\text{Bi}_2\text{Se}_3$ . While showing very large topological Dirac cones which are usually easy to detect, a bad crystal surface can hinder the detection of these. Fig. 4.16 shows example images for GaGeTe in panel a and the noted bad surface of a  $\text{Bi}_2\text{Se}_3$  crystal. It can be seen in the image of the cleaved GaGeTe crystal, that there are clean and shiny parts, but these are quite small and at different angles, making it difficult to measure sharp surface states.

It was then analysed, whether theory could alter the calculations in a way where the changes can be plausibly explained as well as it fits to the proposed structure from ARPES data. This resulted in Fig. 4.17. To achieve this, one axis of the GaGeTe was strained by 1%. As indicated in the introduction to GaGeTe, this system is very sensitive to small changes.

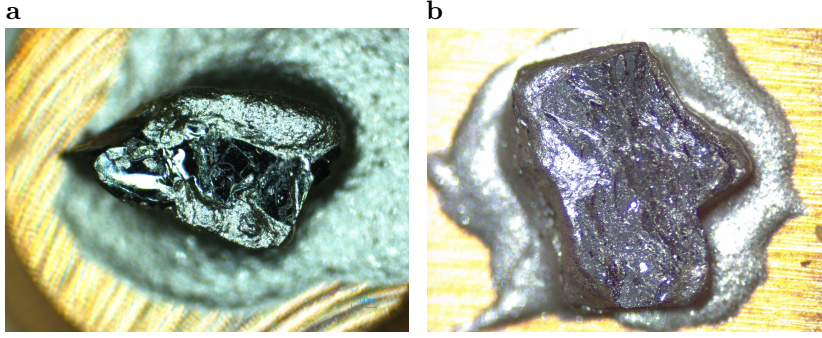


Figure 4.16: a) Surface of a cleaved GaGeTe crystal. b) Bad surface of a cleaved  $\text{Bi}_2\text{Se}_3$  crystal. This  $\text{Bi}_2\text{Se}_3$  crystal did not show any surface states with ARPES.

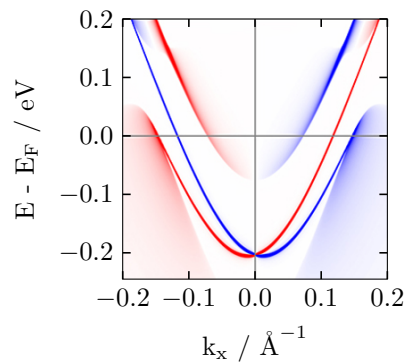


Figure 4.17: Surface feature calculation of GaGeTe using PBE functional and a 1% distortion along one axis of the unit cell. Picture taken from [133].

An important question is now: is such a strain a feasible change, as the crystal parameters were checked after growing. Analysing all the steps of the measurement process identified many situations, where the material could be put under strain, both mechanically and also by reorganization. Major candidates for mechanical strain are curing of the glue under high temperatures together with the thermal expansion of the glue itself after it cured. Second, the sample is cooled down from room temperature to very low temperatures around 5 K and third the situation of cleaving might itself introduce strain. Apart from this, it is also possible to have surface recombination on the cleaved surface, which itself might also have an influence. It has not been analysed yet, how and if each of these mentioned possible sources of strain actually has an influence. But an experiment on a sample holder which can induce a reproducible fixed amount of strain has been proposed to check, whether the gap can be opened with this.

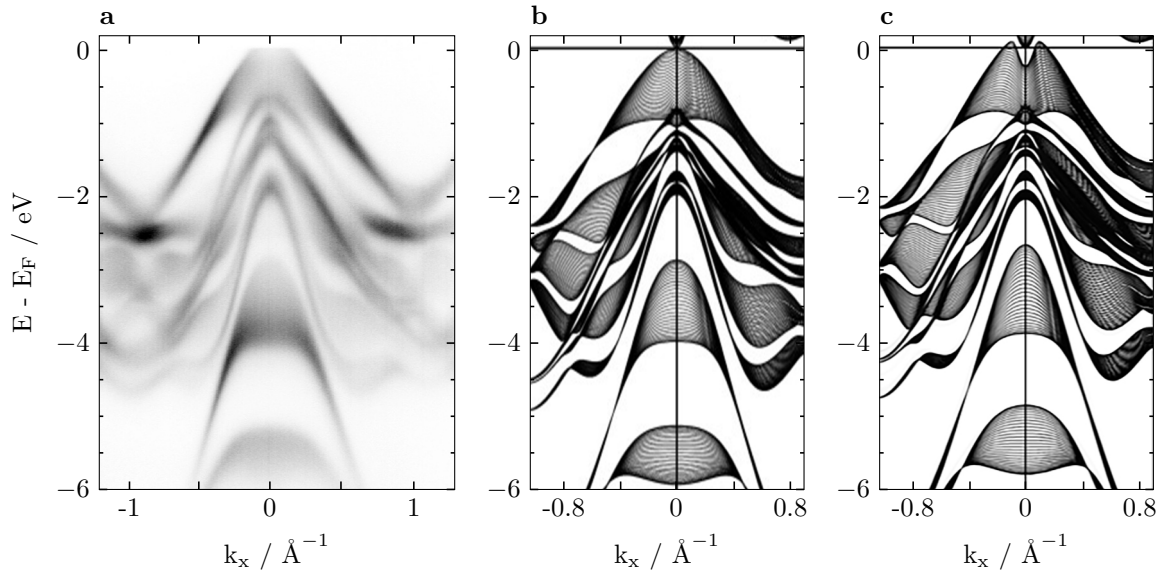


Figure 4.18: Energy-momentum cut and band structure calculations of Fig. 4.12 together with c) band structure calculation as in b), but with a 1% strain on one crystal axis. Noteworthy are the changes close to the Fermi level in those calculations while maintaining parity the same features in the remaining band structure.

Fig. 4.18 shows the calculated band structure already discussed in Fig. 4.12 together with new bulk calculations on a strained crystal lattice. What is immediately visible, is that major parts of the band structure further away from the Fermi level do not show major changes in shape, although some bands change slightly in position. For example, the bands at  $-2$  eV and above are separated farther than without strain. Also, the band  $-1.5$  eV is further down than in the unstrained case. The most important changes are directly at the Fermi level: the dip in the valence band is substantially larger - now reaching down to approximately  $-0.3$  eV while it was barely visible before on this scale. Also, the valence band now clearly crosses the Fermi level as well as overlaps with the conduction band in the energy region, resulting in no direct band gap. When comparing these changes to the measured data, the changes at  $-1.5$  eV can not be resolved in the necessary detail to give a clear answer, but it certainly does not contradict each other. Regarding the change at  $-2$  eV, the expected splitting should be resolvable, but it is seen not as large as calculated. Overall, the band structure is still fitting very well.

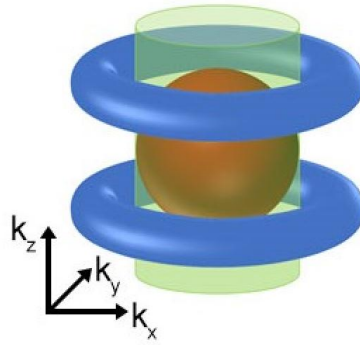


Figure 4.19: Proposed Fermi surface based on the suggested location and behaviour of the band structure and surface features. The conduction forms a ball shape in the middle (red), the valence bands will show up as tori (blue) on the top and the bottom of the Brillouin zone, whereas the 2D surface state will connect both in a cylindrical shape (green). Picture taken from [133].

With the situation observed by ARPES remodelled with calculations, it is also seen that the surface states are still visible in these calculations. Looking into the ARPES panels of Fig. 4.14 and 4.15, another feature is accompanying the conduction band. This band, as not explained by any bulk band calculations, is believed to be a signal from the actual surface state.

Out of this data, a Fermi surface was constructed and shown in Fig. 4.19. The electron pocket is shown in red in the middle, accompanied by two hole pockets as tori. Both 3D features are connected by a cylindrical 2D feature between them.

Overall, this structure has not yet been realized anywhere: A metal like Fermi surface material with no direct band gap hosting 2D Dirac surface features. Because of this, this kind of material was called “simplest  $\mathbb{Z}_2$  topological semimetal”.

## 4.3 Conclusion

In this chapter, GaGeTe was presented. Theoretical predictions showed difficulties to correctly calculate the proper electronic structure as major deviations between different possible methods were observed. Among all calculations, the ones using the PBE

exchange correlation functional showed topological non-trivial states in the style of a 2D Dirac crossing like in  $\text{Bi}_2\text{Se}_3$ .

ARPES measurements showed, that calculations using the PBE functional are giving the same band structure as well as the same  $k_z$  behaviour as the experimentally observed band structure of GaGeTe. This has been shown in multiple figures as well as a comprehensive discussion of different momenta on the  $k_z$  axis. An in-situ dosing experiment has been showing no band gap above the measured Fermi level, essentially ruling out all other results from the other functionals.

The topological analysis revealed, that GaGeTe has indeed no direct, but an indirect band gap, which can be recreated by calculations when straining the crystal lattice. The same calculations show, that the topological states are still present and still in the same shape. Their presence has not been confirmed in full due to very bad surfaces on GaGeTe crystals, but indications of these states have been recorded, making GaGeTe the first material having both, trivial surface states as well as 2D topological states. We thus call this material a simplest  $\mathcal{Z}_2$  topological semimetal.





## 5 Summary

In this thesis, two highly interesting topological materials were presented: TaIrTe<sub>4</sub> and GaGeTe. Both of them, while being very different, are very good candidates for new technologies as well as further research.

TaIrTe<sub>4</sub> is a ternary type-2 Weyl semimetal. It is a non-centrosymmetric material with a crystal structure similar to WTe<sub>2</sub>. It was predicted to host four Weyl points - the minimum number for non-centrosymmetric materials - located very well separated in the Brillouin zone. Calculations also predict, that the Fermi arcs, are connecting the Weyl points while being nearly straight and parallel, making this material a very good candidate for exploring possible application potential of these states. The extensive transport analysis of S. Khim has shown, that typical transport properties are behaving as they are expected to do for Weyl semimetals, like the non-saturating magnetoresistance.

A comprehensive ARPES analysis of the bulk and topological band structure of TaIrTe<sub>4</sub> has been presented, including Fermi surface maps at different photon energies,  $k_z$  maps. The different surface terminations of this material have been discussed thoroughly, but unfortunately during most experiments no cleave of the  $(00\bar{1})$  termination could be achieved. The quantum oscillation measurements have been compared to ARPES Fermi surface feature sizes and a very good correspondence has been shown.

The topological states of TaIrTe<sub>4</sub> have been resolved and shown at the expected positions. As their intensities in the ARPES Fermi surface maps was not very high, their topological character was proven with spin polarization - showing a strong polarization along the arcs, but not perpendicular to them, in an otherwise non-magnetic material. Finally, recent findings, including a superconducting phase at very low temperatures have been briefly discussed.

GaGeTe was predicted by theory as a topological insulator hosting topological states similar to the well known  $\text{Bi}_2\text{Se}_3$ . It is designed around a double-layered germanene block, a germanium based graphene equivalent. During the band structure calculations, the band structure turned out to be difficult to handle for the exchange functionals used. While they are not expected to show the same values, their differences were within a factor of ten between the smallest and the largest band gap calculated. Thus, an ARPES analysis resolving the band structure and band gap is necessary to clarify these difficulties.

Initial ARPES measurements included large momentum-range Fermi surface maps and energy-momentum cuts. Comparing these cuts to all different calculations showed, that the Fermi levels are approximately the same when aligning the calculated and measured bulk features. Dosing the sample surface with potassium lead to an overall shift of the band structure by approximately 330 meV, while not revealing a band gap within that region - a larger scale band gap is therefore ruled out to exist in that material due to the very good correspondence of the bulk data and calculation further away from the Fermi level.

A thorough analysis of the PBE functional calculation - showing the smallest band gap - and ARPES data in dependency of the  $k_z$  value was performed, showing very good correspondence. But when looking at the band structure very close to the Fermi surface, it became obvious, that the ARPES data is differing from all calculations. ARPES data indicates no direct band gap at all but an indirect gap while showing indications of a possible topological state. It was achieved to recreate this state in calculations by straining the unit cell of GaGeTe. These new calculations also showed that the topology is still present in this case.

This leads to the conclusion, that GaGeTe is indeed a topological material with  $\text{Bi}_2\text{Se}_3$  style 2D topological states - but at the same time it is a material without a direct band gap, thus having trivial and topological states at the Fermi level. Such a material was predicted before, but never realized until now. Due to the combination of its properties, the material is called a  $\mathbb{Z}_2$  topological semimetal.

# Bibliography

- [1] G. E. Moore. “Cramming more components onto integrated circuits, Reprinted from Electronics, volume 38, number 8, April 19, 1965, pp.114 ff.” In: *IEEE Solid-State Circuits Society Newsletter* 11.3 (Sept. 2006), pp. 33–35. ISSN: 1098-4232.
- [2] G. E. Moore. “Progress in digital integrated electronics [Technical literature, Copyright 1975 IEEE. Reprinted, with permission. Technical Digest. International Electron Devices Meeting, IEEE, 1975, pp. 11-13.]” In: *IEEE Solid-State Circuits Society Newsletter* 11.3 (Sept. 2006), pp. 36–37. ISSN: 1098-4232.
- [3] J. M. Shalf and R. Leland. “Computing beyond Moore’s Law”. In: *Computer* 48.12 (Dec. 2015).
- [4] T. N. Theis and H.-S. P. Wong. “The End of Moore’s Law: A New Beginning for Information Technology”. In: *Computing in Science & Engineering* 19.2 (2017), pp. 41–50.
- [5] M. M. Waldrop. “The chips are down for Moore’s law”. In: *Nature News* 530.7589 (2016), p. 144.
- [6] J. M. Kosterlitz and D. J. Thouless. “Long range order and metastability in two dimensional solids and superfluids. (Application of dislocation theory)”. In: *Journal of Physics C: Solid State Physics* 5.11 (June 1972), pp. L124–L126.
- [7] J. M. Kosterlitz and D. J. Thouless. “Ordering, metastability and phase transitions in two-dimensional systems”. In: *Journal of Physics C: Solid State Physics* 6.7 (Apr. 1973), pp. 1181–1203.

- 
- [8] D. J. Thouless, M. Kohmoto, M. P. Nightingale, and M. den Nijs. “Quantized Hall Conductance in a Two-Dimensional Periodic Potential”. In: *Phys. Rev. Lett.* 49 (6 Aug. 1982), pp. 405–408.
- [9] F. Haldane. “Continuum dynamics of the 1-D Heisenberg antiferromagnet: Identification with the  $O(3)$  nonlinear sigma model”. In: *Physics Letters A* 93.9 (1983), pp. 464–468. ISSN: 0375-9601.
- [10] F. D. M. Haldane. “Nonlinear Field Theory of Large-Spin Heisenberg Antiferromagnets: Semiclassically Quantized Solitons of the One-Dimensional Easy-Axis Néel State”. In: *Phys. Rev. Lett.* 50 (15 Apr. 1983), pp. 1153–1156.
- [11] G. Rudolf and M. Achim. *Festkörperphysik*. 3rd ed. De Gruyter, 2018. ISBN: 978-3-11-055822-7.
- [12] M. V. Berry. “Quantal phase factors accompanying adiabatic changes”. In: *Proceedings of the Royal Society of London. A. Mathematical and Physical Sciences* 392.1802 (1984), pp. 45–57.
- [13] M. Z. Hasan and C. L. Kane. “Colloquium: Topological insulators”. In: *Rev. Mod. Phys.* 82 (4 Nov. 2010), pp. 3045–3067.
- [14] C. Kane. “Chapter 1 - Topological Band Theory and the 2 Invariant”. In: *Topological Insulators*. Ed. by M. Franz and L. Molenkamp. Vol. 6. Contemporary Concepts of Condensed Matter Science. Elsevier, 2013, pp. 3–34.
- [15] E. H. Ph.D. “XVIII. On the “Rotational Coefficient” in nickel and cobalt”. In: *The London, Edinburgh, and Dublin Philosophical Magazine and Journal of Science* 12.74 (1881), pp. 157–172.
- [16] K. v. Klitzing, G. Dorda, and M. Pepper. “New Method for High-Accuracy Determination of the Fine-Structure Constant Based on Quantized Hall Resistance”. In: *Phys. Rev. Lett.* 45 (6 Aug. 1980), pp. 494–497.
- [17] Nobel Media AB. *Electrons in New Guises*. 1998. URL: <https://www.nobelprize.org/prizes/physics/1998/press-release/> (visited on 05/06/2019).

- [18] R. Kubo. “Statistical-Mechanical Theory of Irreversible Processes. I. General Theory and Simple Applications to Magnetic and Conduction Problems”. In: *Journal of the Physical Society of Japan* 12.6 (1957), pp. 570–586.
- [19] S. Oh. “The Complete Quantum Hall Trio”. In: *Science* 340.6129 (2013), pp. 153–154. ISSN: 0036-8075.
- [20] F. D. M. Haldane. “Model for a Quantum Hall Effect without Landau Levels: Condensed-Matter Realization of the ”Parity Anomaly””. In: *Phys. Rev. Lett.* 61 (18 Oct. 1988), pp. 2015–2018.
- [21] M. König, S. Wiedmann, C. Brüne, A. Roth, H. Buhmann, L. W. Molenkamp, X.-L. Qi, and S.-C. Zhang. “Quantum Spin Hall Insulator State in HgTe Quantum Wells”. In: *Science* 318.5851 (2007), pp. 766–770. ISSN: 0036-8075.
- [22] C.-Z. Chang, J. Zhang, X. Feng, J. Shen, Z. Zhang, M. Guo, K. Li, Y. Ou, P. Wei, L.-L. Wang, Z.-Q. Ji, Y. Feng, S. Ji, X. Chen, J. Jia, X. Dai, Z. Fang, S.-C. Zhang, K. He, Y. Wang, L. Lu, X.-C. Ma, and Q.-K. Xue. “Experimental Observation of the Quantum Anomalous Hall Effect in a Magnetic Topological Insulator”. In: *Science* 340.6129 (2013), pp. 167–170. ISSN: 0036-8075.
- [23] H. Kramers. “HA Kramers, Proc. Acad. Sci. Amsterdam 33, 959 (1930).” In: *Proc. Acad. Sci. Amsterdam*. Vol. 33. 1930, p. 959.
- [24] N. P. Armitage, E. J. Mele, and A. Vishwanath. “Weyl and Dirac semimetals in three-dimensional solids”. In: *Rev. Mod. Phys.* 90 (1 Jan. 2018), p. 015001.
- [25] L. Fu and C. L. Kane. “Topological Insulators with Inversion Symmetry”. In: *Phys. Rev. B* 76 (July 2007), p. 045302.
- [26] H. Nielsen and M. Ninomiya. “The Adler-Bell-Jackiw anomaly and Weyl fermions in a crystal”. In: *Physics Letters B* 130.6 (1983), pp. 389–396. ISSN: 0370-2693.
- [27] L. Fu, C. L. Kane, and E. J. Mele. “Topological Insulators in Three Dimensions”. In: *Phys. Rev. Lett.* 98 (10 Mar. 2007), p. 106803.
- [28] P. A. M. Dirac and R. H. Fowler. “The quantum theory of the electron”. In: *Proceedings of the Royal Society of London. Series A, Containing Papers of a Mathematical and Physical Character* (Feb. 1928).

- [29] Z.-G. Chen, R. Y. Chen, R. D. Zhong, J. Schneeloch, C. Zhang, Y. Huang, F. Qu, R. Yu, Q. Li, G. D. Gu, and N. L. Wang. “Spectroscopic evidence for bulk-band inversion and three-dimensional massive Dirac fermions in ZrTe<sub>5</sub>”. In: *Proceedings of the National Academy of Sciences* 114.5 (2017), pp. 816–821. ISSN: 0027-8424.
- [30] B. Q. Lv, S. Muff, T. Qian, Z. D. Song, S. M. Nie, N. Xu, P. Richard, C. E. Matt, N. C. Plumb, L. X. Zhao, G. F. Chen, Z. Fang, X. Dai, J. H. Dil, J. Mesot, M. Shi, H. M. Weng, and H. Ding. “Observation of Fermi-Arc Spin Texture in TaAs”. In: *Phys. Rev. Lett.* 115 (21 Nov. 2015), p. 217601.
- [31] E. Majorana. “Teoria simmetrica dell’elettrone e del positrone”. In: *Il Nuovo Cimento (1924-1942)* 14.4 (Apr. 1937), p. 171. ISSN: 1827-6121.
- [32] E. Marsch. “A Real Version of the Dirac Equation and Its Coupling to the Electromagnetic Field”. In: *Journal of Modern Physics* 6.01 (2015), p. 1.
- [33] Y. Oreg, G. Refael, and F. von Oppen. “Helical Liquids and Majorana Bound States in Quantum Wires”. In: *Phys. Rev. Lett.* 105 (17 Oct. 2010), p. 177002.
- [34] R. M. Lutchyn, J. D. Sau, and S. Das Sarma. “Majorana Fermions and a Topological Phase Transition in Semiconductor-Superconductor Heterostructures”. In: *Phys. Rev. Lett.* 105 (7 Aug. 2010), p. 077001.
- [35] H. Weyl. “GRAVITATION AND THE ELECTRON”. In: *Proceedings of the National Academy of Sciences* 15.4 (1929), pp. 323–334. ISSN: 0027-8424.
- [36] A. A. Soluyanov, D. Gresch, Z. Wang, Q. Wu, M. Troyer, X. Dai, and B. A. Bernevig. “Type-ii weyl semimetals”. In: *Nature* 527.7579 (2015), p. 495.
- [37] B. Bradlyn, J. Cano, Z. Wang, M. G. Vergniory, C. Felser, R. J. Cava, and B. A. Bernevig. “Beyond Dirac and Weyl fermions: Unconventional quasiparticles in conventional crystals”. In: *Science* 353.6299 (2016). ISSN: 0036-8075.
- [38] W. Witczak-Krempa, G. Chen, Y. B. Kim, and L. Balents. “Correlated Quantum Phenomena in the Strong Spin-Orbit Regime”. In: *Annual Review of Condensed Matter Physics* 5.1 (2014), pp. 57–82.

- [39] M. M. Vazifeh and M. Franz. “Electromagnetic Response of Weyl Semimetals”. In: *Phys. Rev. Lett.* 111 (2 July 2013), p. 027201.
- [40] J. Behrends, A. G. Grushin, T. Ojanen, and J. H. Bardarson. “Visualizing the chiral anomaly in Dirac and Weyl semimetals with photoemission spectroscopy”. In: *Phys. Rev. B* 93 (June 2016), p. 075114.
- [41] A. Molle, J. Goldberger, M. Houssa, Y. Xu, S.-C. Zhang, and D. Akinwande. “Buckled two-dimensional Xene sheets”. In: *Nature Materials* 16 (Jan. 2017), p. 163.
- [42] F. Pielnhofer, T. V. Menshchikova, I. P. Rusinov, A. Zeugner, I. Y. Sklyadneva, R. Heid, K.-P. Bohnen, P. Golub, A. I. Baranov, E. V. Chulkov, et al. “Designing 3D topological insulators by 2D-Xene (X= Ge, Sn) sheet functionalization in GaGeTe-type structures”. In: *Journal of Materials Chemistry C* 5.19 (2017), pp. 4752–4762.
- [43] Hsieh D., Qian D., Wray L., Xia Y., Hor Y. S., Cava R. J., and Hasan M. Z. “A topological Dirac insulator in a quantum spin Hall phase”. In: *Nature* 452 (Apr. 2008), p. 970.
- [44] J. C. Y. Teo, L. Fu, and C. L. Kane. “Surface states and topological invariants in three-dimensional topological insulators: Application to  $\text{Bi}_{1-x}\text{Sb}_x$ ”. In: *Phys. Rev. B* 78 (4 July 2008), p. 045426.
- [45] D. Hsieh, Y. Xia, D. Qian, L. Wray, J. H. Dil, F. Meier, J. Osterwalder, L. Patthey, A. V. Fedorov, H. Lin, A. Bansil, D. Grauer, Y. S. Hor, R. J. Cava, and M. Z. Hasan. “Time-reversal-protected single-Dirac-cone topological-insulator states in  $\text{Bi}_2\text{Te}_3$  and  $\text{Sb}_2\text{Te}_3$ : Topologically Spin-polarized Dirac fermions with  $\pi$  Berry’s Phase”. In: *Phys. Rev. Lett.* 103 (Sept. 2009), p. 146401.
- [46] T. Zhang, P. Cheng, X. Chen, J.-F. Jia, X. Ma, K. He, L. Wang, H. Zhang, X. Dai, Z. Fang, X. Xie, and Q.-K. Xue. *Experimental demonstration of the topological surface states protected by the time-reversal symmetry*. Oct. 2009.

- [47] Xia Y., Qian D., Hsieh D., Wray L., Pal A., Lin H., Bansil A., Grauer D., Hor Y. S., Cava R. J., and Hasan M. Z. “Observation of a large-gap topological-insulator class with a single Dirac cone on the surface”. In: *Nature Physics* 5 (May 2009), p. 398.
- [48] Y. S. Hor, A. Richardella, P. Roushan, Y. Xia, J. G. Checkelsky, A. Yazdani, M. Z. Hasan, N. P. Ong, and R. J. Cava. “p-type Bi<sub>2</sub>Se<sub>3</sub> for topological insulator and low temperature thermoelectric applications”. In: *Physical Review B* 79 (Apr. 2009), p. 195208.
- [49] Hsieh D., Xia Y., Qian D., Wray L., Dil J. H., Meier F., Osterwalder J., Patthey L., Checkelsky J. G., Ong N. P., Fedorov A. V., Lin H., Bansil A., Grauer D., Hor Y. S., Cava R. J., and Hasan M. Z. “A tunable topological insulator in the spin helical Dirac transport regime”. In: *Nature* 460 (July 2009), p. 1101.
- [50] S. R. Park, W. S. Jung, C. Kim, D. J. Song, C. Kim, S. Kimura, K. D. Lee, and N. Hur. “Quasi-particle scattering and protected nature of topological states in a parent topological insulator Bi<sub>2</sub>Se<sub>3</sub>”. In: *Phys. Rev. B* 81 (Dec. 2010), p. 041405.
- [51] Y. L. Chen, J. G. Analytis, J.-H. Chu, Z. K. Liu, S.-K. Mo, X. L. Qi, H. J. Zhang, D. H. Lu, X. Dai, Z. Fang, S. C. Zhang, I. R. Fisher, Z. Hussain, and Z.-X. Shen. “Experimental Realization of a Three-Dimensional Topological Insulator, Bi<sub>2</sub>Te<sub>3</sub>”. In: *Science* 325.5937 (2009), pp. 178–181. ISSN: 0036-8075.
- [52] Z. Wang, H. Weng, Q. Wu, X. Dai, and Z. Fang. “Three-dimensional Dirac semimetal and quantum transport in Cd<sub>3</sub>As<sub>2</sub>”. In: *Physical Review B* 88.12 (2013), p. 125427.
- [53] S. Borisenko, Q. Gibson, D. Evtushinsky, V. Zabolotnyy, B. Büchner, and R. J. Cava. “Experimental realization of a three-dimensional Dirac semimetal”. In: *Physical review letters* 113.2 (2014), p. 027603.
- [54] Z. Liu, J. Jiang, B. Zhou, Z. Wang, Y. Zhang, H. Weng, D. Prabhakaran, S. K. Mo, H. Peng, P. Dudin, et al. “A stable three-dimensional topological Dirac semimetal Cd<sub>3</sub>As<sub>2</sub>”. In: *Nature materials* 13.7 (2014), p. 677.



- [55] Z. Liu, B. Zhou, Y. Zhang, Z. Wang, H. Weng, D. Prabhakaran, S.-K. Mo, Z. Shen, Z. Fang, X. Dai, et al. “Discovery of a three-dimensional topological Dirac semimetal,  $\text{Na}_3\text{Bi}$ ”. In: *Science* 343.6173 (2014), pp. 864–867.
- [56] S.-Y. Xu, C. Liu, S. K. Kushwaha, R. Sankar, J. W. Krizan, I. Belopolski, M. Neupane, G. Bian, N. Alidoust, T.-R. Chang, et al. “Observation of Fermi arc surface states in a topological metal”. In: *Science* 347.6219 (2015), pp. 294–298.
- [57] S. M. Young, S. Zaheer, J. C. Teo, C. L. Kane, E. J. Mele, and A. M. Rappe. “Dirac semimetal in three dimensions”. In: *Physical review letters* 108.14 (2012), p. 140405.
- [58] S. Thirupathaiah, D. Efremov, Y. Kushnirenko, E. Haubold, T. K. Kim, B. R. Pienning, I. Morozov, S. Aswartham, B. Büchner, and S. V. Borisenko. “Absence of Dirac fermions in layered  $\text{BaZnBi}_2$ ”. In: *Phys. Rev. Materials* 3 (2 Feb. 2019), p. 024202.
- [59] Q. Gibson, L. Schoop, L. Muechler, L. Xie, M. Hirschberger, N. Ong, R. Car, and R. Cava. “Three-dimensional Dirac semimetals: Design principles and predictions of new materials”. In: *Physical Review B* 91.20 (2015), p. 205128.
- [60] Q. Li, D. E. Kharzeev, C. Zhang, Y. Huang, I. Pletikosić, A. Fedorov, R. Zhong, J. Schneeloch, G. Gu, and T. Valla. “Chiral magnetic effect in  $\text{ZrTe}_5$ ”. In: *Nature Physics* 12.6 (2016), p. 550.
- [61] X. Yuan, C. Zhang, Y. Liu, A. Narayan, C. Song, S. Shen, X. Sui, J. Xu, H. Yu, Z. An, et al. “Observation of quasi-two-dimensional Dirac fermions in  $\text{ZrTe}_5$ ”. In: *NPG Asia Materials* 8.11 (2016), e325.
- [62] W. Gao, N. Hao, F.-W. Zheng, W. Ning, M. Wu, X. Zhu, G. Zheng, J. Zhang, J. Lu, H. Zhang, C. Xi, J. Yang, H. Du, P. Zhang, Y. Zhang, and M. Tian. “Extremely Large Magnetoresistance in a Topological Semimetal Candidate Pyrite  $\text{PtBi}_2$ ”. In: *Phys. Rev. Lett.* 118 (25 June 2017), p. 256601.
- [63] S. Thirupathaiah, Y. Kushnirenko, E. Haubold, A. Fedorov, E. Rienks, T. Kim, A. Yaresko, C. Blum, S. Aswartham, B. Büchner, S. V. Borisenko, et al. “Pos-

- sible origin of linear magnetoresistance: Observation of Dirac surface states in layered PtBi 2". In: *Physical Review B* 97.3 (2018), p. 035133.
- [64] Gao Wenshuai, Zhu Xiangde, Zheng Fawei, Wu Min, Zhang Jinglei, Xi Chuanying, Zhang Ping, Zhang Yuheng, Hao Ning, Ning Wei, and Tian Mingliang. "A possible candidate for triply degenerate point fermions in trigonal layered PtBi<sub>2</sub>". In: *Nature Communications* 9.1 (2018), p. 3249. ISSN: 2041-1723.
- [65] S.-Y. Xu, I. Belopolski, N. Alidoust, M. Neupane, G. Bian, C. Zhang, R. Sankar, G. Chang, Z. Yuan, C.-C. Lee, et al. "Discovery of a Weyl fermion semimetal and topological Fermi arcs". In: *Science* 349.6248 (Aug. 2015), pp. 613–617.
- [66] B. Lv, N. Xu, H. Weng, J. Ma, P. Richard, X. Huang, L. Zhao, G. Chen, C. Matt, F. Bisti, et al. "Observation of Weyl nodes in TaAs". In: *Nature Physics* 11.9 (2015), p. 724.
- [67] L. Yang, Z. Liu, Y. Sun, H. Peng, H. Yang, T. Zhang, B. Zhou, Y. Zhang, Y. Guo, M. Rahn, et al. "Weyl semimetal phase in the non-centrosymmetric compound TaAs". In: *Nature physics* 11.9 (2015), p. 728.
- [68] Y. Sun, S.-C. Wu, and B. Yan. "Topological surface states and Fermi arcs of the noncentrosymmetric Weyl semimetals TaAs, TaP, NbAs, and NbP". In: *Phys. Rev. B* 92 (Sept. 2015), p. 115428.
- [69] S.-Y. Xu, I. Belopolski, D. S. Sanchez, C. Zhang, G. Chang, C. Guo, G. Bian, Z. Yuan, H. Lu, T.-R. Chang, et al. "Experimental discovery of a topological Weyl semimetal state in TaP". In: *Science advances* 1.10 (2015), e1501092.
- [70] S.-Y. Xu, N. Alidoust, I. Belopolski, Z. Yuan, G. Bian, T.-R. Chang, H. Zheng, V. N. Strocov, D. S. Sanchez, G. Chang, et al. "Discovery of a Weyl fermion state with Fermi arcs in niobium arsenide". In: *Nature Physics* 11.9 (2015), p. 748.
- [71] X. Di-Fei, D. Yong-Ping, W. Zhen, L. Yu-Peng, N. Xiao-Hai, Y. Qi, D. Pavel, X. Zhu-An, W. Xian-Gang, and F. Dong-Lai. "Observation of Fermi arcs in non-centrosymmetric Weyl semi-metal candidate NbP". In: *Chinese Physics Letters* 32.10 (2015), p. 107101.

- [72] C. Wang, Y. Zhang, J. Huang, S. Nie, G. Liu, A. Liang, Y. Zhang, B. Shen, J. Liu, C. Hu, et al. “Observation of Fermi arc and its connection with bulk states in the candidate type-II Weyl semimetal WTe<sub>2</sub>”. In: *Physical Review B* 94.24 (2016), p. 241119.
- [73] F. Y. Bruno, A. Tamai, Q. Wu, I. Cucchi, C. Barreateau, A. De La Torre, S. M. Walker, S. Riccò, Z. Wang, T. Kim, et al. “Observation of large topologically trivial Fermi arcs in the candidate type-II Weyl semimetal WTe<sub>2</sub>”. In: *Physical Review B* 94.12 (2016), p. 121112.
- [74] K. Deng, G. Wan, P. Deng, K. Zhang, S. Ding, E. Wang, M. Yan, H. Huang, H. Zhang, Z. Xu, et al. “Experimental observation of topological Fermi arcs in type-II Weyl semimetal MoTe<sub>2</sub>”. In: *Nature Physics* 12.12 (2016), p. 1105.
- [75] L. Huang, T. M. McCormick, M. Ochi, Z. Zhao, M.-T. Suzuki, R. Arita, Y. Wu, D. Mou, H. Cao, J. Yan, et al. “Spectroscopic evidence for a type II Weyl semimetallic state in MoTe<sub>2</sub>”. In: *Nature materials* 15.11 (2016), p. 1155.
- [76] A. Liang, J. Huang, S. Nie, Y. Ding, Q. Gao, C. Hu, S. He, Y. Zhang, C. Wang, B. Shen, J. Liu, P. Ai, L. Yu, X. Sun, W. Zhao, S. Lv, D. Liu, C. Li, Y. Zhang, Y. Hu, Y. Xu, L. Zhao, G. Liu, Z. Mao, X. Jia, F. Zhang, S. Zhang, F. Yang, Z. Wang, Q. Peng, H. Weng, X. Dai, Z. Fang, Z. Xu, C. Chen, and X. J. Zhou. *Electronic Evidence for Type II Weyl Semimetal State in MoTe<sub>2</sub>*. Apr. 2016.
- [77] A. Tamai, Q. Wu, I. Cucchi, F. Y. Bruno, S. Ricco, T. Kim, M. Hoesch, C. Barreateau, E. Giannini, C. Besnard, et al. “Fermi arcs and their topological character in the candidate type-II Weyl semimetal MoTe<sub>2</sub>”. In: *Physical Review X* 6.3 (2016), p. 031021.
- [78] J. Jiang, Z. Liu, Y. Sun, H. Yang, C. Rajamathi, Y. Qi, L. Yang, C. Chen, H. Peng, C. Hwang, et al. “Signature of type-II Weyl semimetal phase in MoTe<sub>2</sub>”. In: *Nature communications* 8 (2017), p. 13973.
- [79] I. Belopolski, D. S. Sanchez, Y. Ishida, X. Pan, P. Yu, S.-Y. Xu, G. Chang, T.-R. Chang, H. Zheng, N. Alidoust, et al. “Discovery of a new type of topological Weyl fermion semimetal state in Mo<sub>1-x</sub>W<sub>x</sub>Te<sub>2</sub>”. In: *Nature communications* 7 (2016), p. 13643.

- [80] I. Belopolski, S.-Y. Xu, Y. Ishida, X. Pan, P. Yu, D. S. Sanchez, H. Zheng, M. Neupane, N. Alidoust, G. Chang, et al. “Fermi arc electronic structure and Chern numbers in the type-II Weyl semimetal candidate  $\text{Mo}_x\text{W}_{1-x}\text{Te}_2$ ”. In: *Physical Review B* 94.8 (2016), p. 085127.
- [81] S. Borisenko, D. Evtushinsky, Q. Gibson, A. Yaresko, T. Kim, M. Ali, B. Buechner, M. Hoesch, and R. J. Cava. “Time-reversal symmetry breaking type-II Weyl state in  $\text{YbMnBi}_2$ ”. In: *arXiv preprint arXiv:1507.04847* (2015).
- [82] C. Shekhar, N. Kumar, V. Grinenko, S. Singh, R. Sarkar, H. Luetkens, S.-C. Wu, Y. Zhang, A. C. Komarek, E. Kampert, et al. “Anomalous Hall effect in Weyl semimetal half-Heusler compounds  $\text{RPtBi}$  ( $\text{R} = \text{Gd}$  and  $\text{Nd}$ )”. In: *Proceedings of the National Academy of Sciences* 115.37 (2018), pp. 9140–9144.
- [83] G. Chang, S.-Y. Xu, H. Zheng, B. Singh, C.-H. Hsu, G. Bian, N. Alidoust, I. Belopolski, D. S. Sanchez, S. Zhang, et al. “Room-temperature magnetic topological Weyl fermion and nodal line semimetal states in half-metallic Heusler  $\text{Co}_2\text{TiX}$  ( $\text{X} = \text{Si}, \text{Ge}, \text{or Sn}$ )”. In: *Scientific reports* 6 (2016), p. 38839.
- [84] S. Chadov, S.-C. Wu, C. Felser, and I. Galanakis. “Stability of Weyl points in magnetic half-metallic Heusler compounds”. In: *Physical Review B* 96.2 (2017), p. 024435.
- [85] G. Wang and J. Wei. “Topological phase transition in half-Heusler compounds  $\text{HfIrX}$  ( $\text{X} = \text{As}, \text{Sb}, \text{Bi}$ )”. In: *Computational Materials Science* 124 (2016), pp. 311–315.
- [86] Z. Wang, M. Vergniory, S. Kushwaha, M. Hirschberger, E. Chulkov, A. Ernst, N. Ong, R. J. Cava, and B. A. Bernevig. “Time-reversal-breaking Weyl fermions in magnetic Heusler alloys”. In: *Physical review letters* 117.23 (2016), p. 236401.
- [87] S. A. Wolf, D. D. Awschalom, R. A. Buhrman, J. M. Daughton, S. von Molnár, M. L. Roukes, A. Y. Chtchelkanova, and D. M. Treger. “Spintronics: A Spin-Based Electronics Vision for the Future”. In: *Science* 294.5546 (2001), pp. 1488–1495. ISSN: 0036-8075.

- [88] “Devices with a spin”. In: *Nature Electronics* 1.11 (2018), pp. 571–571. ISSN: 2520-1131.
- [89] D. E. Kharzeev and H.-U. Yee. “Anomaly induced chiral magnetic current in a Weyl semimetal: Chiral electronics”. In: *Phys. Rev. B* 88 (11 Sept. 2013), p. 115119.
- [90] S. Bhatti, R. Sbiaa, A. Hirohata, H. Ohno, S. Fukami, and S. Piramanayagam. “Spintronics based random access memory: a review”. In: *Materials Today* 20.9 (2017), pp. 530–548. ISSN: 1369-7021.
- [91] Wang Yi, Zhu Dapeng, Wu Yang, Yang Yumeng, Yu Jiawei, Ramaswamy Rajagopalan, Mishra Rahul, Shi Shuyuan, Elyasi Mehrdad, Teo Kie-Leong, Wu Yihong, and Yang Hyunsoo. “Room temperature magnetization switching in topological insulator-ferromagnet heterostructures by spin-orbit torques”. In: *Nature Communications* 8.1 (2017), p. 1364. ISSN: 2041-1723.
- [92] J. Gooth, G. Schierning, C. Felser, and K. Nielsch. “Quantum materials for thermoelectricity”. In: *MRS Bulletin* 43.3 (2018), pp. 187–192.
- [93] C. Fu, S. N. Guin, S. J. Watzman, G. Li, E. Liu, N. Kumar, V. Sü, W. Schnelle, G. Auffermann, C. Shekhar, Y. Sun, J. Gooth, and C. Felser. “Large Nernst power factor over a broad temperature range in polycrystalline Weyl semimetal NbP”. In: *Energy Environ. Sci.* 11 (10 2018), pp. 2813–2820.
- [94] Oersted. “Notiz von neuen electrisch - magnetischen Versuchen des Herrn Seebeck in Berlin”. In: *Annalen der Physik* 73.4 (1823), pp. 430–432.
- [95] R. He, G. Schierning, and K. Nielsch. “Thermoelectric Devices: A Review of Devices, Architectures, and Contact Optimization”. In: *Advanced Materials Technologies* 3.4 (2018), p. 1700256.
- [96] G. Schierning. “Bring on the heat”. In: *Nature Energy* 3.2 (2018), pp. 92–93. ISSN: 2058-7546.
- [97] G. Li, J. Garcia Fernandez, D. A. Lara Ramos, V. Barati, N. Pérez, I. Soldatov, H. Reith, G. Schierning, and K. Nielsch. “Integrated microthermoelectric coolers

- with rapid response time and high device reliability”. In: *Nature Electronics* 1.10 (2018), pp. 555–561. ISSN: 2520-1131.
- [98] J. Schaumann, M. Loor, D. Ünal, A. Mudring, S. Heimann, U. Hagemann, S. Schulz, F. Maculewicz, and G. Schierning. “Improving the  $zT$  value of thermoelectrics by nanostructuring: tuning the nanoparticle morphology of  $Sb_2Te_3$  by using ionic liquids”. In: *Dalton Trans.* 46 (3 2017), pp. 656–668.
- [99] A. Stern and N. H. Lindner. “Topological Quantum Computation—From Basic Concepts to First Experiments”. In: *Science* 339.6124 (2013), pp. 1179–1184. ISSN: 0036-8075.
- [100] G. P. Collins. “Computing with quantum knots.” In: *Scientific American* (Apr. 2006), pp. 56–63.
- [101] S. Das Sarma, M. Freedman, and C. Nayak. “Topologically Protected Qubits from a Possible Non-Abelian Fractional Quantum Hall State”. In: *Phys. Rev. Lett.* 94 (16 Apr. 2005), p. 166802.
- [102] C. Nayak, S. H. Simon, A. Stern, M. Freedman, and S. Das Sarma. “Non-Abelian anyons and topological quantum computation”. In: *Rev. Mod. Phys.* 80 (3 Sept. 2008), pp. 1083–1159.
- [103] S. D. Sarma, M. Freedman, and C. Nayak. “Majorana zero modes and topological quantum computation”. In: *Npj Quantum Information* 1 (Oct. 2015), p. 15001.
- [104] A. Damascelli. “Probing the electronic structure of complex systems by ARPES”. In: *Physica Scripta* 2004.T109 (2004), p. 61.
- [105] H. Hertz. “Ueber einen Einfluss des ultravioletten Lichtes auf die elektrische Entladung”. In: *Annalen der Physik* 267.8 (1887), pp. 983–1000.
- [106] A. Einstein. “Über einen die Erzeugung und Verwandlung des Lichtes betreffenden heuristischen Gesichtspunkt”. In: *Annalen der Physik* 322.6 (1905), pp. 132–148.

- [107] M. Seah and W. Dench. “Quantitative electron spectroscopy of surfaces. A standard data base for electron inelastic mean free paths in solids.[Review 10 to 10,000 eV above Fermi level]”. In: (1979).
- [108] N. Doiron-Leyraud, C. Proust, D. LeBoeuf, J. Levallois, J.-B. Bonnemaïson, R. Liang, D. A. Bonn, W. N. Hardy, and L. Taillefer. “Quantum oscillations and the Fermi surface in an underdoped high-Tc superconductor”. In: *Nature* 447 (May 2007), p. 565.
- [109] S. V. Borisenko. ““One-cubed” ARPES User Facility at BESSY II”. In: *Synchrotron Radiation News* 25.5 (2012), pp. 6–11.
- [110] A. Varykhalov. “1<sup>2</sup>-ARPES: The ultra high resolution photoemission station at the U112-PGM-2a-1<sup>2</sup> beamline at BESSY II”. In: *Journal of large-scale research facilities* 4 (2018), A128.
- [111] M. Hoesch, T. K. Kim, P. Dudin, and F. Baumberger. “State of the art in high resolution synchrotron radiation Angle-Resolved Photoemission Spectroscopy”. In: *Hoshako* 29.5 (2016), pp. 253–262.
- [112] T. Okuda, K. Miyamaoto, H. Miyahara, K. Kuroda, A. Kimura, H. Namatame, and M. Taniguchi. “Efficient spin resolved spectroscopy observation machine at Hiroshima Synchrotron Radiation Center”. In: *Review of Scientific Instruments* 82.10 (2011), p. 103302.
- [113] T. Okuda, K. Miyamoto, A. Kimura, H. Namatame, and M. Taniguchi. “A double VLEED spin detector for high-resolution three dimensional spin vectorial analysis of anisotropic Rashba spin splitting”. In: *Journal of Electron Spectroscopy and Related Phenomena* 201 (2015). Special issue on electron spectroscopy for Rashba spin-orbit interaction, pp. 23–29. ISSN: 0368-2048.
- [114] G. Nicolay, F. Reinert, F. Forster, D. Ehm, S. Schmidt, B. Eltner, and S. Hüfner. “About the stability of noble-metal surfaces during VUV-photoemission experiments”. In: *Surface science* 543.1-3 (2003), pp. 47–56.

- [115] S. Eich, A. Stange, A. Carr, J. Urbancic, T. Popmintchev, M. Wiesenmayer, K. Jansen, A. Ruffing, S. Jakobs, T. Rohwer, S. Hellmann, C. Chen, P. Matyba, L. Kipp, K. Rosnagel, M. Bauer, M. Murnane, H. Kapteyn, S. Mathias, and M. Aeschlimann. “Time- and angle-resolved photoemission spectroscopy with optimized high-harmonic pulses using frequency-doubled Ti:Sapphire lasers”. In: *Journal of Electron Spectroscopy and Related Phenomena* 195 (2014), pp. 231–236. ISSN: 0368-2048.
- [116] K. Koepnik, D. Kasinathan, D. V. Efremov, S. Khim, S. Borisenko, B. Büchner, and J. van den Brink. “TaIrTe<sub>4</sub> a ternary Type-II Weyl semi-metal”. In: *Phys. Rev. B Rap. Comm.* 93 (May 2016), p. 201101.
- [117] S. Khim, K. Koepnik, D. V. Efremov, J. Klotz, T. Förster, J. Wosnitza, M. I. Sturza, S. Wurmehl, C. Hess, J. van den Brink, and B. Büchner. “Magnetotransport and de Haas-van Alphen measurements in the type-II Weyl semimetal TaIrTe<sub>4</sub>”. In: *Phys. Rev. B* 94 (May 2016), p. 165145.
- [118] E. Haubold, K. Koepnik, D. Efremov, S. Khim, A. Fedorov, Y. Kushnirenko, J. van den Brink, S. Wurmehl, B. Büchner, T. K. Kim, M. Hoesch, K. Sumida, K. Taguchi, T. Yoshikawa, A. Kimura, T. Okuda, and S. V. Borisenko. “Experimental realization of type-II Weyl state in non-centrosymmetric TaIrTe<sub>4</sub>”. In: *Phys. Rev. B* 95 (Sept. 2017), p. 241108.
- [119] J. P. Perdew and Y. Wang. “Accurate and simple analytic representation of the electron-gas correlation energy”. In: *Physical Review B* 45.23 (1992), p. 13244.
- [120] K. Koepnik and H. Eschrig. “Full-potential nonorthogonal local-orbital minimum-basis band-structure scheme”. In: *Physical Review B* 59.3 (1999), p. 1743.
- [121] I. Belopolski, P. Yu, D. S. Sanchez, Y. Ishida, T.-R. Chang, S. S. Zhang, S.-Y. Xu, H. Zheng, G. Chang, G. Bian, et al. “Signatures of a time-reversal symmetric Weyl semimetal with only four Weyl points”. In: *Nature communications* 8.1 (2017), p. 942.
- [122] “SAINT”. In: *SAINT* <https://xray.utmb.edu/saint.html> (1998).



- [123] G. M. Sheldrick. “Crystal structure refinement with SHELXL”. In: *Acta Crystallographica Section C: Structural Chemistry* 71.1 (2015), pp. 3–8.
- [124] V. Petricek, M. Dusek, and L. Palatinus. “Crystallographic computing system JANA2006: general features”. In: *Zeitschrift für Kristallographie-Crystalline Materials* 229.5 (2014), pp. 345–352.
- [125] Y. Xing, Z. Shao, J. Ge, J. Wang, Z. Zhu, J. Liu, Y. Wang, Z. Zhao, J. Yan, D. Mandrus, B. Yan, X.-J. Liu, M. Pan, and J. Wang. *Surface Superconductivity in the type II Weyl Semimetal TaIrTe<sub>4</sub>*. Sept. 2018.
- [126] G. Kra, R. Eholie, and J. Flahant. “” In: *Comptes Rendus des Seances de l’Academie des Sciences, Serie C: Science Chimiques* 284 (1977), pp. 889–892.
- [127] D. Fenske and H. G. V. Schnering. “GaGeTe, eine neue Defekt-Tetraederstruktur”. In: *Angewandte Chemie* 95.5 (1983), pp. 420–421.
- [128] E. Lopez-Cruz, M. Cardona, and E. Martinez. “Raman spectrum and lattice dynamics of GaGeTe”. In: *Physical Review B* 29.10 (1984), p. 5774.
- [129] C. Drasar, V. Kucek, L. Benes, P. Lostak, and M. Vlcek. “Thermoelectric properties and nonstoichiometry of GaGeTe”. In: *Journal of Solid State Chemistry* 193 (2012), pp. 42–46.
- [130] V. Kucek, C. Drasar, J. Navratil, L. Benes, and P. Lostak. “Optical and transport properties of GaGeTe single crystals”. In: *Journal of Crystal Growth* 380 (2013), pp. 72–77.
- [131] J. Zhang, S.-s. Li, W.-x. Ji, C.-w. Zhang, P. Li, S.-f. Zhang, P.-j. Wang, and S.-s. Yan. “Two-dimensional GaGeTe film: a promising graphene-like material with tunable band structure and high carrier mobility”. In: *Journal of Materials Chemistry C* 5.34 (2017), pp. 8847–8853.
- [132] W. Wang, L. Li, Z. Zhang, J. Yang, D. Tang, and T. Zhai. “Ultrathin GaGeTe p-type transistors”. In: *Applied Physics Letters* 111.20 (2017), p. 203504.

- 
- [133] E. Haubold, A. Fedorov, I. P. Rusinov, T. V. Menshchikova, V. Duppel, D. Friedrich, F. Pielhofer, R. Wehrich, A. Pfitzner, A. Zeugner, A. Isaeva, S. Thirupathaiyah, Y. Kushnirenko, E. Rienks, T. Kim, E. V. Chulkov, B. Büchner, and S. V. Borisenko. *Possible Experimental Realization of a Basic Z<sub>2</sub> Topological Semimetal*. Dec. 2018.
- [134] G. Kresse. “Beyond standard DFT”. In: *EPJ Web of Conferences*. Vol. 14. EDP Sciences. 2011, p. 01004.
- [135] K. Dewhurst, S. Sharma, L. Nordstrom, F. Cricchio, F. Bultmark, H. Gross, C. Ambrosch-Draxl, C. Persson, C. Brouder, R. Armiento, et al. “The elk FP-LAPW code”. In: *ELK*, <http://elk.sourceforge.net> (2016).
- [136] G. Kresse and J. Furthmüller. “Efficient iterative schemes for ab initio total-energy calculations using a plane-wave basis set”. In: *Physical review B* 54.16 (1996), p. 11169.
- [137] G. Kresse and D. Joubert. “From ultrasoft pseudopotentials to the projector augmented-wave method”. In: *Physical Review B* 59.3 (1999), p. 1758.
- [138] J. Hafner. “Ab-initio simulations of materials using VASP: Density-functional theory and beyond”. In: *Journal of computational chemistry* 29.13 (2008), pp. 2044–2078.

# List of Publications

- E. Haubold, A. Fedorov, I. P. Rusinov, T. V. Menshchikova, V. Duppel, D. Friedrich, F. Pielhofer, R. Wehrich, A. Pfitzner, A. Zeugner, A. Isaeva, S. Thirupathaiah, Y. Kushnirenko, E. Rienks, T. Kim, E. V. Chulkov, B. Büchner, S. V. Borisenko. *Possible Experimental Realization of a Basic Z2 Topological Semimetal*. Dec. 2018
- E. Haubold, K. Koepnik, D. Efremov, S. Khim, A. Fedorov, Y. Kushnirenko, J. van den Brink, S. Wurmehl, B. Büchner, T. K. Kim, M. Hoesch, K. Sumida, K. Taguchi, T. Yoshikawa, A. Kimura, T. Okuda, S. V. Borisenko. “Experimental realization of type-II Weyl state in non-centrosymmetric TaIrTe<sub>4</sub>”. In: *Phys. Rev. B* 95 (Sept. 2017), p. 241108
- S. Thirupathaiah, D. Efremov, Y. Kushnirenko, E. Haubold, T. K. Kim, B. R. Piennig, I. Morozov, S. Aswartham, B. Büchner, S. V. Borisenko. “Absence of Dirac fermions in layered BaZnBi<sub>2</sub>”. In: *Phys. Rev. Materials* 3 (2 Feb. 2019), p. 024202
- A. Fedorov, A. Yaresko, E. Haubold, Y. Kushnirenko, T. Kim, B. Buechner, S. Aswartham, S. Wurmehl, S. Borisenko. *Energy scale of nematic ordering in the parent iron-based superconductor: BaFe<sub>2</sub>As<sub>2</sub>*. Nov. 2018
- S. Thirupathaiah, I. Morozov, Y. Kushnirenko, A. V. Fedorov, E. Haubold, T. K. Kim, G. Shipunov, A. Maksutova, O. Kataeva, S. Aswartham, B. Büchner, S. V. Borisenko. “Spectroscopic evidence of topological phase transition in the three-dimensional Dirac semimetal Cd<sub>3</sub>(As<sub>1-x</sub>P<sub>x</sub>)<sub>2</sub>”. In: *Phys. Rev. B* 98 (8 Aug. 2018), p. 085145

- Y. S. Kushnirenko, A. V. Fedorov, E. Haubold, S. Thirupathaiiah, T. Wolf, S. Aswartham, I. Morozov, T. K. Kim, B. Büchner, S. V. Borisenko. “Three-dimensional superconducting gap in FeSe from angle-resolved photoemission spectroscopy”. In: *Phys. Rev. B* 97 (18 May 2018), p. 180501
- S. Thirupathaiiah, Y. Kushnirenko, E. Haubold, A. Fedorov, E. Rienks, T. Kim, A. Yaresko, C. Blum, S. Aswartham, B. Büchner, S. V. Borisenko. “Possible origin of linear magnetoresistance: Observation of Dirac surface states in layered PtBi<sub>2</sub>”. In: *Physical Review B* 97.3 (2018), p. 035133
- Y. S. Kushnirenko, A. A. Kordyuk, A. V. Fedorov, E. Haubold, T. Wolf, B. Büchner, S. V. Borisenko. “Anomalous temperature evolution of the electronic structure of FeSe”. In: *Phys. Rev. B* 96 (10 Sept. 2017), p. 100504
- A. Fedorov, A. Yaresko, T. K. Kim, Y. Kushnirenko, E. Haubold, T. Wolf, M. Hoesch, A. Grüneis, B. Büchner, S. V. Borisenko. “Effect of nematic ordering on electronic structure of FeSe”. In: *Scientific Reports* 6 (Nov. 2016), p. 36834
- E. Haubold, P. Schöppe, S. Eckner, S. Lehmann, I. Colantoni, F. d’Acapito, F. di Benedetto, S. Schorr, C. S. Schnohr. “Short-range versus long-range structure in Cu(In,Ga)Se<sub>2</sub>, Cu(In,Ga)<sub>3</sub>Se<sub>5</sub>, and Cu(In,Ga)<sub>5</sub>Se<sub>8</sub>”. In: *Journal of Alloys and Compounds* 774 (2019), pp. 803–812. ISSN: 0925-8388
- V. Eckert, E. Haubold, S. Oswald, S. Michel, C. Bellmann, P. Potapov, D. Wolf, S. Hampel, B. Büchner, M. Mertig. “Investigation of the surface properties of different highly aligned N-MWCNT carpets”. In: *Carbon* 141 (2019), pp. 99–106
- S. Eckner, K. Ritter, P. Schöppe, E. Haubold, E. Eckner, J. Rensberg, R. Röder, M. C. Ridgway, C. S. Schnohr. “Bond-strength inversion in (In,Ga)As semiconductor alloys”. In: *Phys. Rev. B* 97 (19 May 2018), p. 195202
- C. S. Schnohr, S. Eckner, P. Schöppe, E. Haubold, d’Acapito, D. Greiner, C. A. Kaufmann. “Reversible correlation between subnanoscale structure and Cu content in co-evaporated Cu(In,Ga)Se<sub>2</sub> thin films”. In: *Acta Materialia* 153 (2018), pp. 8–14. ISSN: 1359-6454

# Acknowledgements

This work would have not been possible without the contributions and support of many people, whom I want to thank now.

First, I'd like to thank the IFW Dresden and Prof. Dr. Bernd Büchner for giving me the opportunity to work in this scientific environment. I'd also like to thank Prof. Dr. Oliver Rader for writing a referee report for my thesis and Dr. Sergey Borisenko for his supervision during the last 3.5 years and all the interesting discussions we had. Additionally I'd like to acknowledge Dr. Sergey Borisenko and the DFG for the project "Dirac and Weyl semimetals" under grant number BO 1912/7-1.

Special thanks is due to all my ARPES co-workers and group members, namely Dr. Alexander Fedorov, Dr. Setti Thirupathaiah, Yevhen Kushnirenko and Volodymyr Bezghuba. I learned a lot from all our beamtimes and lab sessions. I'd like to thank Dr. Roland Hübel, Marco Naumann and Stephan Leger for their technical assistance as well as Dr. Emile Rienks and Dr. Timur Kim for all their scientific and technical support during the numerous beamtimes.

I'd like to thank Kerstin Höllerer and Katja Schmiedel for their administrative support in many situations, especially for their asisstances connected to all the travels I was allowed to do.

For their work as co-authors with my papers, I want to thank Dr. Klaus Koepernik and Dr. Dmitri Efremov for their theoretical work and assistance on  $\text{TaIrTe}_4$  and Dr. Seunghyun Khim for the growing of the samples as well as providing the transport measurements. I also want to thank Dr. Saicharan Aswartham and Boy Roman Piening for their continued work on  $\text{TaRhTe}_4$  and it's derivates among many different samples they provided. For their work on  $\text{GaGeTe}$  I'd like to thank Dr. Anna Isaeva and Dr. Florian Pielnhofer for all the fruitfull discussions and Dr. Tatiana Menshchikova and

Dr. Igor Rusinov for their theoretical calculations on this very complex material.

Although my presence in my office was quite rare, I want to thank Sebastian Selter and Julian Zeisner as well as all the other colleagues there to always welcome me and having an open ear for tricky sample data discussions and Dr. Uwe Gräfe, Dr. Frederick Klein and Dr. Yannick Utz among others for welcoming me to this office 3.5 years ago. For their work on organizing social events and keeping all the PhD students connected I want to thank Margaritha Iakovleva, Richard Hentrich, Matthias Gillig and Christoph Wuttke and all the other members of the IFF PhD councils, helping hands during all these events and so on which I did not mention before.

Finally, I want to thank my parents, family and friends for all their support, distraction and interest in my work and Victoria Eckert for stopping me, when I start to write silly things.

# Erklärung

Hiermit versichere ich, dass ich die vorliegende Arbeit ohne unzulässige Hilfe Dritter und ohne Benutzung anderer als der angegebenen Hilfsmittel angefertigt habe; die aus fremden Quellen direkt oder indirekt übernommenen Gedanken sind als solche kenntlich gemacht. Die Arbeit wurde bisher weder im Inland noch im Ausland in gleicher oder ähnlicher Form einer anderen Prüfungsbehörde vorgelegt.

Die vorliegende Arbeit wurde am Institut für Festkörperforschung (IFF) des Leibniz-Institutes für Festkörper- und Werkstoffforschung Dresden e.V. (IFW Dresden) unter wissenschaftlicher Betreuung von Herrn Prof. Dr. Bernd Büchner angefertigt. Es haben keine früheren Promotionsverfahren stattgefunden.

Ich erkenne hiermit die Promotionsordnung der Fakultät Mathematik und Naturwissenschaften der Technischen Universität Dresden vom 23.2.2011 an.

---

Erik Haubold

Dresden, Mai 2019